

Higgs Production with a Central Jet Veto at NNLL+NNLO

Carola F. Berger,^a Claudio Marcatonini,^a Iain W. Stewart,^{a,b} Frank J. Tackmann,^a and Wouter J. Waalewijn^{a,c}

^a*Center for Theoretical Physics, Massachusetts Institute of Technology, Cambridge, MA 02139, U.S.A.*

^b*Center for the Fundamental Laws of Nature, Harvard University, Cambridge, MA 02138, U.S.A.*

^c*Department of Physics, University of California at San Diego, La Jolla, CA 92093, U.S.A.*

E-mail: cfberger@mit.edu, cmarcant@mit.edu, iains@mit.edu, frank@mit.edu,
wouterw@physics.ucsd.edu

ABSTRACT: A major ingredient in Higgs searches at the Tevatron and LHC is the elimination of backgrounds with jets. In current $H \rightarrow WW \rightarrow \ell\nu\ell\nu$ searches, jet algorithms are used to veto central jets to obtain a 0-jet sample, which is then analyzed to discover the Higgs signal. Imposing this tight jet veto induces large double logarithms which significantly modify the Higgs production cross section. These jet-veto logarithms are presently only accounted for at fixed order or with the leading-logarithmic summation from parton-shower Monte Carlos. Here we consider Higgs production with an inclusive event-shape variable for the jet veto, namely beam thrust \mathcal{T}_{cm} , which has a close correspondence with a traditional p_T jet veto. \mathcal{T}_{cm} allows us to systematically sum the large jet-veto logarithms to higher orders and to provide better estimates for theoretical uncertainties. We present results for the 0-jet Higgs production cross section from gluon fusion at next-to-next-to-leading-logarithmic order (NNLL), fully incorporating fixed-order results at next-to-next-to-leading order (NNLO). At this order the scale uncertainty is 15 – 20%, depending on the cut, implying that a larger scale uncertainty should be used in current Tevatron bounds on the Higgs.

KEYWORDS: Higgs Physics, Hadronic Colliders, Jets

Contents

1	Introduction	2
2	Components of the Calculation	9
2.1	Hard Virtual Corrections	11
2.2	Gluon Beam Function	13
2.3	Soft Function	17
2.4	Nonsingular Contributions	18
2.5	Cross Section at NNLL+NNLO	23
2.6	Choice of Running Scales	24
2.7	PDFs and π^2 Summation	26
2.8	Nonperturbative Corrections	27
3	Numerical Results	28
3.1	Convergence of Resummed Predictions	29
3.2	Comparison of Resummed and Fixed-Order Predictions	31
3.3	Discussion of K -Factors	35
4	Conclusions	36
A	NLO Calculation of the Gluon Beam Function	39
A.1	Definition and General Results	39
A.2	The Gluon PDF at One Loop	42
A.3	The Gluon Beam Function at One Loop	43
A.4	Integrals, Discontinuities, and Plus Distributions	48
B	Perturbative Results	49
B.1	Hard Function	49
B.2	Beam Function	51
B.3	Renormalization Group Evolution	53
B.4	Singular Fixed-Order NLO and NNLO Coefficients	55

1 Introduction

The discovery of the Higgs boson is a major goal of the Large Hadron Collider (LHC) and current analyses at the Tevatron. The decay $H \rightarrow WW^*$ is the dominant channel for Higgs masses $m_H \gtrsim 130$ GeV. Hence, the $H \rightarrow W^+W^- \rightarrow \ell^+\nu\ell^-\bar{\nu}$ channel has strong discovery potential and plays a very important role for early searches that are statistically limited. It is the dominant channel in the current Tevatron exclusion limit [1]. The presence of the final-state neutrinos does not allow the reconstruction of the Higgs invariant mass, and hence sideband methods cannot be used for this channel to determine the backgrounds directly from data. At the LHC and Tevatron, $t\bar{t} \rightarrow W^+W^-b\bar{b}$ events constitute a large background, dominating the signal by a factor of 10 to 40 depending on the Higgs mass and center-of-mass energy. Requiring a minimum missing energy is not effective against this background since it also contains two neutrinos. To eliminate the huge background from top-quark decays one imposes a stringent jet veto to define a 0-jet sample for the search, where one only allows soft jets with $p_T^{\text{jet}} \leq p_T^{\text{cut}}$. The latest ATLAS study [2] vetoes any jets with transverse momentum $p_T^{\text{jet}} \geq 20$ GeV and pseudorapidity $|\eta^{\text{jet}}| \leq 4.8$, which reduces the $t\bar{t}$ background to a negligible level. The latest CMS study [3] rejects all events that have jets with $p_T^{\text{jet}} \gtrsim 25$ GeV and $|\eta^{\text{jet}}| \leq 2.5$, which reduces this background by a factor of ~ 40 . After the jet veto, the main irreducible background stems from the direct production channel $pp \rightarrow W^+W^-$, which at this point still dominates the signal by a factor of about 4 : 1. The final discrimination against this and other backgrounds is achieved by exploiting several kinematic variables [4].

The Tevatron Higgs searches analyze their data using a jet algorithm and Monte Carlo to implement a jet veto and divide the data into 0-jet, 1-jet, and ≥ 2 -jet samples for all jets with $p_T^{\text{jet}} \geq 15$ GeV and $|\eta^{\text{jet}}| \leq 2.4 - 2.5$ [1, 5, 6]. For $m_H \gtrsim 130$ GeV the sensitivity is completely dominated by the 0-jet and 1-jet samples in $H \rightarrow WW$. At lower Higgs masses, the WH , ZH , and vector-boson-fusion production channels with higher jet multiplicities are included to increase sensitivity. With the latest update from ICHEP 2010 [7], the Tevatron excludes a range of Higgs masses $m_H = 158 - 175$ GeV at 95% confidence level. For these exclusion limits it is important to have a good theoretical understanding of the jet production cross sections and a reliable estimate of theory uncertainties separately for each jet bin, as emphasized in ref. [8]. The theory uncertainties in the Higgs production cross section were investigated recently in refs. [9–11]. For their 0-jet bin, the Tevatron analyses use an uncertainty of 7%, which is taken from the fixed next-to-next-to-leading order (NNLO) analysis of the 0-jet bin in ref. [8]. With our resummed next-to-next-to-leading logarithmic order (NNLL) plus NNLO calculation of a 0-jet cross section we will see that the perturbative uncertainties are actually larger, $\simeq 20\%$, due to the presence of large logarithms that are not accounted for in the fixed-order analysis.

Theoretically, the inclusive Higgs production cross section has been studied extensively in the literature and is known to NNLO [12–19] and including NLO electroweak corrections [20–22] (for reviews and additional references see e.g. refs. [23, 24]). However, Higgs production in a 0-jet sample differs substantially from inclusive Higgs production. In particular, the jet

veto induces large double logarithms $\alpha_s^n \ln^m(p_T^{\text{cut}}/m_H)$ with $m \leq 2n$ that are not present in the inclusive cross section, and also induces a sizable dependence on the choice of jet algorithm used to define the veto (see e.g. ref. [25]). Theoretical studies of the jet veto are available in fixed-order calculations at NNLO [26–28], and include additional kinematic selection cuts [8, 25, 29, 30] (see also ref. [31]).

Currently, the only method available to experiments to incorporate the effect of the jet veto and the accompanying large logarithms beyond fixed order is to use parton-shower Monte Carlos, such as MC@NLO [32, 33], POWHEG [34, 35], PYTHIA [36, 37], and HERWIG [38, 39]. This allows one to take into account the dependence of the 0-jet sample on the choice of jet algorithm, but for the large logarithms it limits the accuracy to the leading-logarithmic summation provided by the parton shower. The comparison [8, 25, 28] of the results at fixed NLO with those from MC@NLO, HERWIG, and PYTHIA (the latter two reweighted to the total NLO cross section), shows differences of 20 – 30%, cf. tables 4 and 1 of refs. [8, 25] respectively. This shows the importance of resumming the phase-space logarithms caused by the jet veto. Furthermore, the HERWIG and PYTHIA parton-level results obtained in ref. [8] differ by about 15%, which is an indication that subleading phase-space logarithms are relevant.

Theoretically, one can also study the Higgs production as a function of the Higgs transverse momentum, p_T^H , both in fixed-order perturbation theory for large p_T^H [40–43] and with a resummation of logarithms of p_T^H at small p_T^H [44–51]. A further method is the so-called joint factorization [48, 52], which allows one to simultaneously resum logarithms at threshold and small p_T^H by introducing p_T -dependent PDFs. For $H \rightarrow W^+W^- \rightarrow \ell^+\nu\ell^-\bar{\nu}$ the missing neutrino momenta make a direct measurement of small p_T^H impossible. Instead the NNLL resummed p_T^H spectrum [53] is used to reweight the PYTHIA Higgs spectrum in the Tevatron search, which is important for estimating the efficiency of selection cuts. The study of p_T -resummation is also motivated by the fact that the jet veto automatically forces p_T^H to be small, see e.g. refs. [8, 25, 54]. However, the logarithms at small p_T^H summed at NNLL differ from those induced by the jet veto. Thus studies of the small- p_T^H spectrum can only provide a qualitative template for the effect of the jet veto.¹

In this paper we explore a jet veto in $pp \rightarrow HX$ at the LHC and $p\bar{p} \rightarrow HX$ at the Tevatron using an inclusive kinematic variable called beam thrust [56]. Beam thrust does not require a jet algorithm and is well-suited for carrying out higher-order logarithmic resummation. It allows us to directly predict a 0-jet Higgs production cross section using factorization techniques without relying on parton showers or hadronization models from Monte Carlo. We will present results for both the differential beam-thrust spectrum as well as the integrated $pp \rightarrow H + 0j$ cross section with a cut on beam thrust working at NNLL and including the NNLO corrections.² With the large logarithms under control, we are also able to perform a

¹On the other hand, the hadronic E_T spectrum could be considered for a central jet veto, and the resummation at small E_T was carried out in ref. [55] at NLL order.

²Our NNLL resummation is in the jet-veto variable, and is not the same as NNLL threshold resummations for the total cross section [57–62].

realistic assessment of the perturbative theory uncertainties. Since a factorization theorem exists for the beam thrust spectrum we are also able to rigorously account for the leading effect of nonperturbative hadronization corrections. A final advantage of beam thrust is that the cross section for the dominant irreducible background, $pp \rightarrow WW + 0j$, can be computed with precisely the same jet veto and similar precision, which we leave to future work.

While $H \rightarrow WW$ provides the most obvious motivation for studying the effect of jet vetoes, one can also consider the case of $H \rightarrow \gamma\gamma$. Here, the Higgs signal appears as a small bump in the $\gamma\gamma$ invariant mass spectrum on top of a smooth but overwhelming QCD background. The signal and background are separated from each other by a combined fit to both. The main reducible backgrounds are $pp \rightarrow jj$ and $pp \rightarrow j\gamma$, while the irreducible background comes from QCD diphoton production, $pp \rightarrow \gamma\gamma$. Experimentally, it is still advantageous to separate the data into 0-jet, 1-jet, and ≥ 2 -jet samples because in each sample the background has a different shape, which helps to gain sensitivity in the fit. However, this separation introduces the same theoretical issues as for the jet veto in $H \rightarrow WW$. Beam thrust provides a continuous measure of the 0-jettiness of an event. Hence, instead of using separate jet samples it may be useful to perform a combined fit to the beam thrust and $\gamma\gamma$ invariant mass spectra. The theoretical formulas presented here can be used to study $H \rightarrow \gamma\gamma$, and we briefly comment on this, however we choose to focus on $H \rightarrow WW$.

In $H \rightarrow WW$, where missing energy plays an important role, the appropriate version of beam thrust is defined in the hadronic center-of-mass frame [56, 63] by

$$\tau = \frac{\mathcal{T}_{\text{cm}}}{m_H}, \quad \mathcal{T}_{\text{cm}} = \sum_k |\vec{p}_{kT}| e^{-|\eta_k|} = \sum_k (E_k - |p_k^z|). \quad (1.1)$$

The central jet veto using beam thrust is implemented by requiring $\mathcal{T}_{\text{cm}} \ll m_H$, or equivalently $\tau \ll 1$. Since the mass of the Higgs, m_H , is unknown, for our analysis the dimension-one variable \mathcal{T}_{cm} is more convenient than the dimensionless τ . The sum over k in eq. (1.1) runs over all particles in the final state, excluding the signal leptons from the W decays. Here \vec{p}_{kT} and η_k are the measured transverse momentum and rapidity of particle k with respect to the beam axis (taken to be the z axis).³ For simplicity we assume all particles to be massless.

To see that a cut on $\mathcal{T}_{\text{cm}} \ll m_H$ vetoes central jets, first note that the absolute value in eq. (1.1) divides all particles k into two hemispheres $\eta_k, p_k^z > 0$ and $\eta_k, p_k^z < 0$. We can now distinguish between energetic particles with $E_k \sim m_H$ and soft particles with $E_k \ll m_H$. The latter only give small contributions to \mathcal{T}_{cm} . Energetic particles moving in the forward direction have $E_k - |p_k^z| \ll m_H$, so they also contribute only small amounts. In particular, unmeasured particles beyond the rapidity reach of the detector are exponentially suppressed, $|\vec{p}_{kT}| e^{-|\eta_k|} \approx 2E_k e^{-2|\eta_k|}$, and give negligible contributions. On the other hand, energetic particles in the central region have $E_k - |p_k^z| \sim E_k \sim m_H$ and give a large contribution.

³Just as for jet algorithms, experimentally the sum will be over pseudo-particles constructed from calorimeter clusters and possibly supplemented by tracking information. Using information from the tracking systems is important to reduce the impact of pile-up as it allows to distinguish particles originating from the primary hard interaction from those due to secondary minimum-bias interactions.

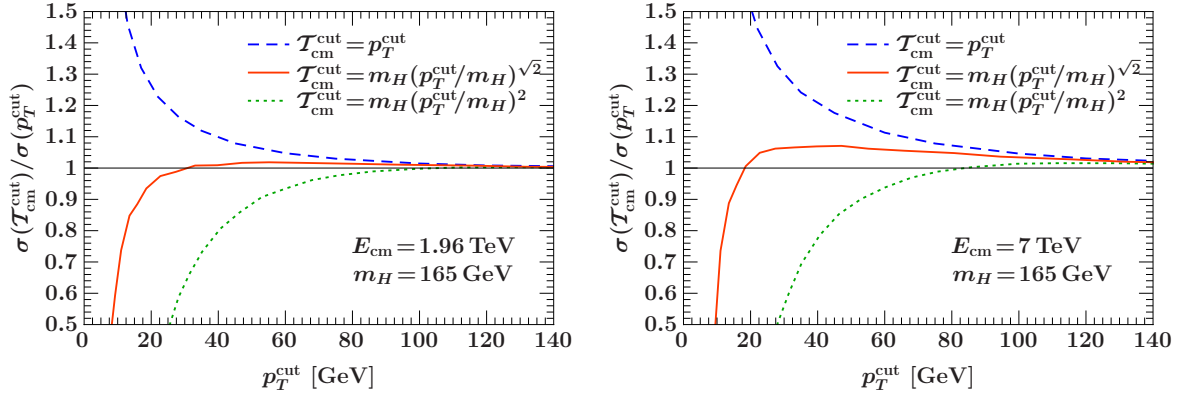


Figure 1. Comparison of different relations between p_T^{cut} and $\mathcal{T}_{\text{cm}}^{\text{cut}}$ for the NNLO cross section, where the left panel is for the Tevatron and the right panel is for the LHC. The relation $\mathcal{T}_{\text{cm}}^{\text{cut}} \simeq m_H(p_T^{\text{cut}}/m_H)^{\sqrt{2}}$ yields the same leading large logarithm at $\mathcal{O}(\alpha_s)$ and also the best overall agreement at NNLO. Here we used MSTW2008 NNLO PDFs [64] and evaluate the cross section at $\mu = m_H$.

Therefore, a cut $\mathcal{T}_{\text{cm}} \leq \mathcal{T}_{\text{cm}}^{\text{cut}} \ll m_H$ provides an inclusive veto on central energetic jets without requiring a jet algorithm.

An important question is how the 0-jet cross section $\sigma(\mathcal{T}_{\text{cm}}^{\text{cut}})$ with the jet-veto cut $\mathcal{T}_{\text{cm}} \leq \mathcal{T}_{\text{cm}}^{\text{cut}}$ compares to the more standard $\sigma(p_T^{\text{cut}})$ with a traditional jet-veto cut on the maximum p_T of the jets, $p_T^{\text{jet}} \leq p_T^{\text{cut}}$. To relate the uncertainties due to the large logarithms in these two cross sections, we can compare their leading double-logarithmic terms at $\mathcal{O}(\alpha_s)$ using our computation and the one in ref. [26]:

$$\sigma(\mathcal{T}_{\text{cm}}^{\text{cut}}) \propto \left(1 - \frac{\alpha_s C_A}{\pi} \ln^2 \frac{\mathcal{T}_{\text{cm}}^{\text{cut}}}{m_H} + \dots\right), \quad \sigma(p_T^{\text{cut}}) \propto \left(1 - \frac{2\alpha_s C_A}{\pi} \ln^2 \frac{p_T^{\text{cut}}}{m_H} + \dots\right). \quad (1.2)$$

To obtain agreement for the leading-logarithmic terms in eq. (1.2) the correct correspondence between the two variables is

$$\mathcal{T}_{\text{cm}}^{\text{cut}} \simeq m_H \left(\frac{p_T^{\text{cut}}}{m_H}\right)^{\sqrt{2}}. \quad (1.3)$$

We can check the accuracy of this relation for the two jet vetoes at NNLO numerically using the FEHiP program [27, 43]. This fixed-order comparison contains not only leading logarithms, but also subleading logarithms and non-logarithmic terms. The ratio of the NNLO cross sections using different trial relations for the correspondence between $\mathcal{T}_{\text{cm}}^{\text{cut}}$ and p_T^{cut} are shown in figure 1. With the relation in eq. (1.3) the NNLO cross sections differ by $\leq 2\%$ at the Tevatron, and $\leq 7\%$ at the LHC, throughout the range of interesting cuts. If we multiply the prefactor in eq. (1.3) by a factor of 1/2 or 2 then the agreement is substantially worse, close to that of the dotted and dashed curves in figure 1. This confirms that eq. (1.3) provides a realistic estimate for the correspondence. However, it does not directly test the correspondence for the cross sections with resummation at NLL order or beyond.

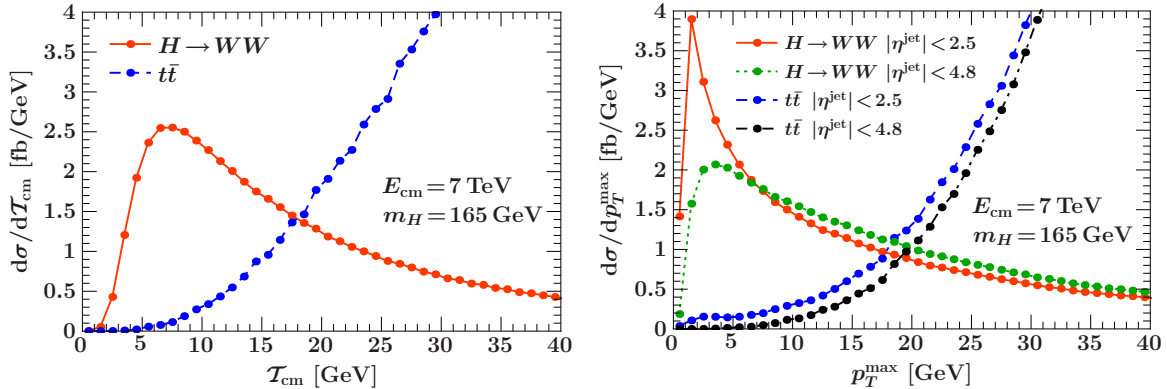


Figure 2. Comparison of the Higgs signal and $t\bar{t}$ background using PYTHIA. The differential spectrum in \mathcal{T}_{cm} is shown on the left, and in p_T^{max} , the p_T of the hardest jet, on the right. For the jet algorithm we use the anti- k_t algorithm with $R = 0.4$, only considering jets with $|\eta^{\text{jet}}| < 2.5$ or $|\eta^{\text{jet}}| < 4.8$.

To illustrate the relative size of the $H \rightarrow WW$ signal compared to the $t\bar{t} \rightarrow WWb\bar{b}$ background as a function of either \mathcal{T}_{cm} or the p_T of the hardest jet, p_T^{max} , we use PYTHIA 8 [37] to simulate $gg \rightarrow H \rightarrow WW$ for $m_H = 165$ GeV and $t\bar{t} \rightarrow WWb\bar{b}$ events. In both cases we turn off multiple interactions in PYTHIA, since the corresponding uncertainty is hard to estimate without dedicated LHC tunes. Following the selection cuts from ATLAS in ref. [2] we force one W to decay into an electron and one into a muon. We then require both leptons to have $p_T > 15$ GeV and $|\eta| < 2.5$. For the dilepton invariant mass we require $12 \text{ GeV} < m_{\ell\ell} < 300 \text{ GeV}$, and for the missing transverse momentum, $p_T^{\text{miss}} > 30 \text{ GeV}$. We have not attempted to implement any lepton isolation criteria since they should have a similar effect on the Higgs signal and $t\bar{t}$ background. For the p_T jet veto we define jets using the anti- k_t algorithm [65] with $R = 0.4$ implemented in the FASTJET package [66]. The results for the differential cross section in \mathcal{T}_{cm} and p_T^{max} after the above cuts are shown in figure 2, where the normalization corresponds to the total cross sections $\sigma_{gg \rightarrow H} = 8 \text{ pb}$ and $\sigma_{t\bar{t}} = 163 \text{ pb}$ (see e.g. ref. [67]). Note that the above selection cuts have no effect on the shape of the Higgs signal and a small 5 – 20% effect on the shape of the $t\bar{t}$ background. In this simulation a signal to background ratio of one is achieved with cuts $\mathcal{T}_{\text{cm}} < 31 \text{ GeV}$, $p_T^{\text{max}} < 32 \text{ GeV}$ for $|\eta| < 2.5$, and $p_T^{\text{max}} < 33 \text{ GeV}$ for $|\eta| < 4.8$. It will be very interesting to see the performance of \mathcal{T}_{cm} in a full experimental analysis including a b -jet veto from b -tagging which will further improve the suppression of $t \rightarrow Wb$ decays with only small effects on the Higgs signal.

We have also tested the correspondence between the \mathcal{T}_{cm} and p_T^{cut} variables using partonic PYTHIA 8 Higgs samples for the LHC at 7 TeV. The cut $p_T < p_T^{\text{cut}}$ is applied for $R = 0.4$ anti- k_T jets with rapidities $|\eta| < \eta^{\text{cut}}$. For $\eta^{\text{cut}} = 4.8$ the variable correspondence is roughly midway between $\mathcal{T}_{\text{cm}} = p_T^{\text{cut}}$ and the relation in eq. (1.3), whereas for $\eta^{\text{cut}} = 2.5$ the correspondence is closer to $\mathcal{T}_{\text{cm}} = p_T^{\text{cut}}$. For the Tevatron the correspondence is also closer to $\mathcal{T}_{\text{cm}} = p_T^{\text{cut}}$ with less dependence on η^{cut} . To estimate the impact of our results on the uncertainties for the p_T^{cut} jet veto we will consider the range between eq. (1.3) and $\mathcal{T}_{\text{cm}} = p_T^{\text{cut}}$.

Further discussion on how to apply our results to the experimental analyses using reweighted Monte Carlo samples is left to section 4.

Including the resummation of large logarithms for $\mathcal{T}_{\text{cm}} \ll m_H$, the production cross section from gluon fusion, $gg \rightarrow H$, is given by the factorization theorem [56]

$$\begin{aligned} \frac{d\sigma}{d\mathcal{T}_{\text{cm}}} &= \sigma_0 H_{gg}(m_t, m_H^2, \mu) \int dY \int dt_a dt_b B_g(t_a, x_a, \mu) B_g(t_b, x_b, \mu) \\ &\times S_B^{gg} \left(\mathcal{T}_{\text{cm}} - \frac{e^{-Y}t_a + e^Y t_b}{m_H}, \mu \right) + \frac{d\sigma^{\text{ns}}}{d\mathcal{T}_{\text{cm}}}, \end{aligned} \quad (1.4)$$

where

$$x_a = \frac{m_H}{E_{\text{cm}}} e^Y, \quad x_b = \frac{m_H}{E_{\text{cm}}} e^{-Y}, \quad \sigma_0 = \frac{\sqrt{2}G_F m_H^2}{576\pi E_{\text{cm}}^2}, \quad (1.5)$$

E_{cm} is the total center-of-mass energy, and Y is the rapidity of the Higgs.⁴ The limits on the Y integration are $\ln(m_H/E_{\text{cm}}) \leq Y \leq -\ln(m_H/E_{\text{cm}})$.

In this paper we focus our attention on the Higgs production cross section. The leptonic decay of the Higgs does not alter the factorization structure for the summation of large logarithms in the first term in eq. (1.4), where it can be included straightforwardly as was done in ref. [56] for the simpler case of $pp \rightarrow Z/\gamma \rightarrow \ell^+ \ell^-$. Its effect on the second term can be more involved. Including the Higgs decay is of course important in practical applications, which use additional leptonic variables to discriminate against the $pp \rightarrow WW$ background. A further investigation of these effects using factorization is left for future work.

By using a cut on $\mathcal{T}_{\text{cm}} \leq \mathcal{T}_{\text{cm}}^{\text{cut}}$ to implement the jet veto, the resulting large double logarithms in the 0-jet cross section have the form $\alpha_s^n \ln^m(\mathcal{T}_{\text{cm}}^{\text{cut}}/m_H)$ with $m \leq 2n$. Measuring \mathcal{T}_{cm} introduces two new energy scales into the problem. In addition to the hard-interaction scale $\mu_H \simeq m_H$, one is now sensitive to an intermediate beam scale $\mu_B^2 \simeq \mathcal{T}_{\text{cm}} m_H$ and a soft scale $\mu_S \simeq \mathcal{T}_{\text{cm}}$. In the first term in eq. (1.4), the physics at each of these scales is factorized into separate hard, beam, and soft functions, H_{gg} , B_g , S_B^{gg} , which are briefly discussed below. The veto induced logarithms are systematically summed using this factorized result for the singular terms in the cross section. These functions and the nonsingular cross section components, $d\sigma^{\text{ns}}/d\mathcal{T}_{\text{cm}}$, are discussed in detail in section 2. The full expression in eq. (1.4) applies for any value of \mathcal{T}_{cm} , and reduces to the fixed-order result when $\mathcal{T}_{\text{cm}} \simeq m_H$.

When $\mathcal{T}_{\text{cm}} \ll m_H$ the absence of additional hard jets in the final state implies that the dominant corrections appearing at μ_H are hard virtual corrections, which are described by the hard function, $H_{gg}(m_t, m_H^2, \mu_H)$. It contains the virtual top-quark loop that generates the effective ggH vertex plus the effects of any additionally exchanged hard virtual gluons.

⁴For $H \rightarrow \gamma\gamma$ the Higgs rapidity Y is measurable. With no additional jets in the event it provides the boost of the partonic hard collision relative to the hadronic center-of-mass frame. In this case one can account for this boost in the definition of beam thrust, $\mathcal{T}_B = \sum_k |\vec{p}_{kT}| e^{-|\eta_k - Y|}$, which effectively defines beam thrust in the partonic center-of-mass frame. Just as for \mathcal{T}_{cm} , a jet veto is obtained by imposing $\mathcal{T}_B \ll m_H$. The factorization theorem for the gluon-fusion production cross section for $\mathcal{T}_B \ll m_H$ is the same as in eq. (1.4) but with Y set to zero inside S_B^{gg} [56]. The difference between $d\sigma/\mathcal{T}_{\text{cm}}$ and $d\sigma/d\mathcal{T}_B$ first appears at NLO and NNLL and is numerically small, at the 4% level.

The jet veto explicitly restricts the energetic initial-state radiation (ISR) emitted by the incoming gluon to be collinear to the proton direction. As a result, the energetic ISR cannot be described by the evolution of the standard parton distribution functions (PDFs), which would treat it fully inclusively. In this situation, as discussed in detail in refs. [56, 68], the initial state containing the colliding gluon is described by a gluon beam function, $B_g(t, x, \mu_B)$, which depends on the momentum fraction x and spacelike virtuality $-t < 0$ of the gluon annihilated in the hard interaction. The beam function can be computed as [68, 69]

$$B_g(t, x, \mu_B) = \sum_{j=\{g, q, \bar{q}\}} \int_x^1 \frac{d\xi}{\xi} \mathcal{I}_{gj}\left(t, \frac{x}{\xi}, \mu_B\right) f_j(\xi, \mu_B). \quad (1.6)$$

Here, $f_j(\xi, \mu_B)$ is the standard PDF describing the probability to find a parton j with light-cone momentum fraction ξ in the proton, which is probed at the beam scale μ_B . The virtual and real collinear ISR emitted by the parton j builds up an incoming jet and is described by the perturbative coefficients $\mathcal{I}_{gj}(t, x/\xi, \mu_B)$. At tree level, a gluon from the proton directly enters the hard interaction without emitting any radiation, so $B_g(t, x, \mu_B) = \delta(t) f_g(x, \mu_B)$. Beyond tree level, real emissions decrease the parton's momentum fraction to $x \leq \xi$ and push it off shell with $-t < 0$. \mathcal{T}_{cm} for small values is given by

$$\mathcal{T}_{\text{cm}} = \frac{e^{-Y} t_a}{m_H} + \frac{e^Y t_b}{m_H} + \mathcal{T}_{\text{cm}}^{\text{soft}} + \mathcal{O}(\mathcal{T}_{\text{cm}}^2), \quad (1.7)$$

where the t_a - and t_b -dependent terms are the total contributions from forward and backward collinear ISR. Here $\mathcal{T}_{\text{cm}}^{\text{soft}}$ is the total contribution from soft radiation and is determined by the beam-thrust soft function $S_B^{gg}(\mathcal{T}_{\text{cm}}^{\text{soft}}, \mu_S)$. Neither $\mathcal{T}_{\text{cm}}^{\text{soft}}$ nor $t_{a,b}$ are physical observables that can be measured separately. Hence, in eq. (1.4) we integrate over t_a and t_b subject to the constraint in eq. (1.7), where the integration limits are determined by $t_{a,b} \geq 0$ and $\mathcal{T}_{\text{cm}}^{\text{soft}} \geq 0$.

In section 2 we describe all the ingredients required for our calculation of the 0-jet Higgs production cross section from gluon fusion at NNLL+NNLO. The hard, beam, and soft functions are discussed in sections 2.1, 2.2, and 2.3, respectively. In sections 2.4 and 2.5 we describe how we add the nonsingular NNLO corrections, which are terms not contained in the NNLL result. The treatment of running renormalization scales is described in section 2.6, the impact of π^2 summation and PDF choices in section 2.7, and the size of hadronization corrections in section 2.8. Details of the calculations are relegated to appendices. (In appendix A we calculate the one-loop matching of the gluon beam function onto gluon and quark PDFs, and verify at one loop that the IR divergences of the gluon beam function match those of the gluon PDF. In appendix B we present analytic fixed-order results for the hard and beam functions with terms up to NNLO, as well as results for the singular NLO and NNLO beam thrust cross section.) In section 3 we present our results for the Higgs production cross section as a function of beam thrust up to NNLL+NNLO order. In section 3.1 we study the convergence of our resummed predictions. In section 3.2 we compare our resummed to the fixed-order predictions, and our main results for the theoretical scale uncertainties are presented in figs. 15 and 16. The origin of the large K -factors for Higgs production is discussed in section 3.3.

Section 4 contains our conclusions and outlook, including comments on the implications of our results for the current Tevatron Higgs limits. Readers not interested in technical details should focus their reading on the introduction to section 2 (skipping its subsections), and then read sections 3 and 4.

2 Components of the Calculation

The differential cross section for \mathcal{T}_{cm} in eq. (1.4) can be separated into a singular and nonsingular piece

$$\frac{d\sigma}{d\mathcal{T}_{\text{cm}}} = \left(\frac{d\sigma^{\text{s}}}{d\mathcal{T}_{\text{cm}}} + \frac{d\sigma^{\text{ns}}}{d\mathcal{T}_{\text{cm}}} \right) \left[1 + \mathcal{O}\left(\frac{\Lambda_{\text{QCD}}}{m_H}\right) \right]. \quad (2.1)$$

Including the renormalization group running of the hard, beam, and soft functions, we have

$$\begin{aligned} \frac{d\sigma^{\text{s}}}{d\mathcal{T}_{\text{cm}}} &= \sigma_0 H_{gg}(m_t, m_H^2, \mu_H) U_H(m_H^2, \mu_H, \mu) \int dY \int dt_a dt_b \\ &\times \int dt'_a B_g(t_a - t'_a, x_a, \mu_B) U_B^g(t'_a, \mu_B, \mu) \int dt'_b B_g(t_b - t'_b, x_b, \mu_B) U_B^g(t'_b, \mu_B, \mu) \\ &\times \int dk S_B^{gg}\left(\mathcal{T}_{\text{cm}} - \frac{e^{-Y}t_a + e^Y t_b}{m_H} - k, \mu_S\right) U_S(k, \mu_S, \mu). \end{aligned} \quad (2.2)$$

Equation (2.2) is valid to all orders in perturbation theory and is derived in ref. [56] using the formalism of soft-collinear effective theory (SCET) [70–74]. In addition we will consider the cumulant,

$$\sigma(\mathcal{T}_{\text{cm}}^{\text{cut}}) = \int_0^{\mathcal{T}_{\text{cm}}^{\text{cut}}} d\mathcal{T}_{\text{cm}} \frac{d\sigma}{d\mathcal{T}_{\text{cm}}}, \quad (2.3)$$

which gives the cross section with the jet-veto cut $\mathcal{T}_{\text{cm}} < \mathcal{T}_{\text{cm}}^{\text{cut}}$. For $\sigma(\mathcal{T}_{\text{cm}}^{\text{cut}})$ the relevant scales are $\mu_H \simeq m_H$, $\mu_B^2 \simeq \mathcal{T}_{\text{cm}}^{\text{cut}} m_H$, and $\mu_S \simeq \mathcal{T}_{\text{cm}}^{\text{cut}}$.

Letting $v - i0$ be the Fourier conjugate variable to $\tau = \mathcal{T}_{\text{cm}}/m_H$, the Fourier-transformed singular cross section exponentiates and has the form

$$\ln \frac{d\sigma^{\text{s}}}{dv} \sim \ln v (\alpha_s \ln v)^k + (\alpha_s \ln v)^k + \alpha_s (\alpha_s \ln v)^k + \dots, \quad (2.4)$$

where $k \geq 1$. The three sets of terms represent the LL, NLL, and NNLL corrections, respectively. As usual for problems involving Sudakov double logarithms, the summation happens in the exponent of the cross section, which sums a much larger set of terms compared to counting the leading logarithms in the cross section. To sum the terms in eq. (2.4) to all orders in α_s , the hard function, H_{gg} , beam functions, B_g , and soft function, S_B^{gg} , in eq. (2.2) are each evaluated at their natural scales, $\mu_H \simeq m_H$, $\mu_B \simeq \sqrt{\mathcal{T}_{\text{cm}} m_H}$, $\mu_S \simeq \mathcal{T}_{\text{cm}}$, and are then evolved to the common scale μ by their respective renormalization group evolution factors U_H , U_B^g , and U_S to sum the series of large logarithms. In table 1 we show various orders in resummed perturbation theory and the corresponding accuracy needed for the matching

	matching (singular)	nonsingular	γ_x	Γ_{cusp}	β	PDF
LO	LO	LO	-	-	1-loop	LO
NLO	NLO	NLO	-	-	2-loop	NLO
NNLO	NNLO	NNLO	-	-	3-loop	NNLO
LL	LO	-	-	1-loop	1-loop	LO
NLL	LO	-	1-loop	2-loop	2-loop	LO
NNLL	NLO	-	2-loop	3-loop	3-loop	NLO
NLL'+NLO	NLO	NLO	1-loop	2-loop	2-loop	NLO
NNLL+NNLO	(N)NLO	NNLO	2-loop	3-loop	3-loop	NNLO
NNLL'+NNLO	NNLO	NNLO	2-loop	3-loop	3-loop	NNLO
N ³ LL+NNLO	NNLO	NNLO	3-loop	4-loop	4-loop	NNLO

Table 1. The order counting we use in fixed-order and resummed perturbation theory. The last two rows are beyond the level of our calculations here, but are discussed in the text.

(i.e. the fixed-order results for the hard, beam, and soft functions) and anomalous dimensions (γ_x , Γ_{cusp}) that enter the singular corrections. To NNLL order we require the NLO fixed-order corrections for H_{gg} , B_g , and S_B^{gg} , as well as the two-loop non-cusp and three-loop cusp anomalous dimensions in the evolution factors, and the three-loop running of α_s .

The nonsingular contributions, $d\sigma^{\text{ns}}/d\mathcal{T}_{\text{cm}}$ in eq. (2.1), are $\mathcal{O}(\mathcal{T}_{\text{cm}}/m_H)$ suppressed relative to the resummed contribution, $d\sigma^s/d\mathcal{T}_{\text{cm}}$. They become important at large \mathcal{T}_{cm} and are required to ensure that the resummed results also reproduce the fixed-order cross section at a given order.

For the various combinations in table 1 we show the order at which nonsingular corrections are included, which for consistency agrees with the order for the singular matching corrections. For example, to include the fixed NLO corrections in the NLL result requires including both the singular and nonsingular NLO terms, which we denote as NLL'+NLO. Similarly at one higher order we would obtain NNLL'+NNLO. The prime in both cases refers to the fact that the matching corrections in the resummed result are included at one higher order than what would be necessary for the resummation only. The complete NNLO matching corrections for the beam and soft functions, which we would need at NNLL' and N³LL, are not available at present. Instead, for our final result, which we denote as NNLL+NNLO, we only include the μ -dependent NNLO terms in H_{gg} , B_g , and S_B^{gg} , which we compute using the two-loop RGEs. The remaining μ -independent NNLO terms are added in addition to the nonsingular NNLO terms, as discussed in section 2.5, such that the fixed-order expansion of our final result always reproduces the complete NNLO expression.

In the following sections 2.1 to 2.3, the hard, beam, and soft function are discussed in turn, including expressions for their fixed-order corrections as well as their NNLL evolution. The one-loop results for the hard and soft function are easily obtained from known results. The one-loop calculation for the gluon beam function is performed in appendix A.3. The

anomalous dimensions are all known and given in appendix B.3. The basic SCET ingredients relevant to our context are reviewed in refs. [56, 68]. To obtain numerical results for the cross section, we use the identities from App. B of ref. [75] to evaluate the required convolutions of the various plus distributions in the fixed-order results and evolution kernels. In section 2.4 we discuss how to extract the nonsingular contributions at NLO and NNLO, and in section 2.5 how these are combined with the resummed singular result to give our final result valid to NNLL+NNLO.

The scale μ in eq. (2.2) is an arbitrary auxiliary scale and the cross section is manifestly independent of it at each order in resummed perturbation theory. This fact can be used to eliminate one of the evolution factors by setting μ equal to one of μ_H , μ_B , or μ_S . The relevant factorization scales in the resummed result at which a fixed-order perturbative series is evaluated are the three scales μ_H , μ_B , and μ_S . Hence, their dependence only cancels out up to the order one is working, and the residual dependence on these scales can be used to provide an improved estimate of theoretical uncertainties from higher orders in perturbation theory. The choice of scales used for our central value and to estimate the perturbative uncertainties is discussed in section 2.6. Finally, in section 2.7 we briefly discuss the effect that the π^2 summation and the order of the used PDFs have on our results.

2.1 Hard Virtual Corrections

The hard function contains hard virtual corrections at the scale of order m_H , including the virtual top-quark loop that generates the effective ggH vertex. It is obtained by matching the full theory onto the effective Hamiltonian in SCET

$$\mathcal{H}_{\text{eff}} = \frac{H}{12\pi v} \sum_{n_1, n_2} \int d\omega_1 d\omega_2 C_{ggH}(m_t, 2\tilde{b}_1 \cdot \tilde{b}_2) (2\tilde{b}_1 \cdot \tilde{b}_2) g_{\mu\nu} \mathcal{B}_{n_1, -\omega_1 \perp}^{\mu c} \mathcal{B}_{n_2, -\omega_2 \perp}^{\nu c}. \quad (2.5)$$

Here, H denotes the physical Higgs field and $v = (\sqrt{2}G_F)^{-1/2} = 246$ GeV the Higgs vacuum expectation value. The $\mathcal{B}_{n, \omega}^\mu$ fields are gauge invariant fields in SCET that describe energetic gluons with large momentum $\tilde{b}_i = \omega_i n_i / 2$, where n_i are unit light-cone vectors, $n_i^2 = 0$. The matching coefficient C_{ggH} depends on the top-quark mass and the invariant mass $2\tilde{b}_1 \cdot \tilde{b}_2$ of the two gluons. For the case we are interested in we have $2\tilde{b}_1 \cdot \tilde{b}_2 = q^2$, where q is the total momentum of the Higgs, i.e. of the WW or $\gamma\gamma$ pair. In addition to the operator shown in eq. (2.5), there are also operators where the Higgs couples to two collinear quark fields. The tree-level matching onto these operators is proportional to the light quark mass, m_q , and are numerically very small. There are potentially larger matching contributions from QCD loops where the Higgs couples to a top quark, but these are also m_q/m_H suppressed due to helicity conservation. Hence, we neglect these collinear quark operators in our analysis.

The hard function is defined as

$$H_{gg}(m_t, q^2, \mu) = |C_{ggH}(m_t, q^2, \mu)|^2. \quad (2.6)$$

It is evaluated at $q^2 = m_H^2$ in eq. (2.2) because we consider the production of an on-shell Higgs. (Including the decay of the Higgs, the cross section differential in q^2 is proportional

to $\sigma_0 LH_{gg}(m_t, q^2, \mu)$, where L contains the squared Higgs propagator and decay matrix element. In the narrow width approximation L reduces to $L = \delta(q^2 - m_H^2)\text{Br}$, where Br is the appropriate Higgs branching ratio, e.g. $\text{Br}(H \rightarrow WW)$ or $\text{Br}(H \rightarrow \gamma\gamma)$.

By matching onto eq. (2.5) we integrate out all degrees of freedom above the scale μ_H , which are the heavy top quark as well as gluons and light quarks with offshellness above μ_H . This can be done in either one or two steps. In the one-step matching used here we integrate out both the top quark and hard off-shell modes at the same time. This allows us to keep the full dependence on m_H^2/m_t^2 . In pure dimensional regularization with $\overline{\text{MS}}$ the matching coefficient $C_{ggH}(m_t, q^2, \mu_H)$ is given by the infrared-finite part of the full m_t -dependent ggH form factor, which is known analytically at NLO (corresponding to two loops) [76, 77] and in an expansion in q^2/m_t^2 at NNLO (three loops) [78, 79].

We write the Wilson coefficient as

$$C_{ggH}(m_t, q^2, \mu_H) = \alpha_s(\mu_H) F^{(0)}\left(\frac{q^2}{4m_t^2}\right) \left\{ 1 + \frac{\alpha_s(\mu_H)}{4\pi} \left[C^{(1)}\left(\frac{-q^2 - i0}{\mu_H^2}\right) + F^{(1)}\left(\frac{q^2}{4m_t^2}\right) \right] \right. \\ \left. + \frac{\alpha_s^2(\mu_H)}{(4\pi)^2} \left[C^{(2)}\left(\frac{-q^2 - i0}{\mu_H^2}, \frac{q^2}{4m_t^2}\right) + F^{(2)}\left(\frac{q^2}{4m_t^2}\right) \right] \right\}, \quad (2.7)$$

where $F^{(0)}(0) = 1$. At NNLL we need the NLO coefficients

$$C^{(1)}(x_H) = C_A \left(-\ln^2 x_H + \frac{\pi^2}{6} \right), \quad F^{(1)}(0) = 5C_A - 3C_F. \quad (2.8)$$

The dependence of $F^{(0)}(z)$ and $F^{(1)}(z)$ on $z = q^2/(4m_t^2)$, which encodes the m_t dependence, is given in eq. (B.1). At NNLL+NNLO we also need to include the NNLO terms that depend logarithmically on the hard scale μ_H , which follow from the two-loop RGE of the Wilson coefficient (see eq. (B.12)), and are given by

$$C^{(2)}(x_H, z) = \frac{1}{2} C_A^2 \ln^4 x_H + \frac{1}{3} C_A \beta_0 \ln^3 x_H + C_A \left[\left(-\frac{4}{3} + \frac{\pi^2}{6} \right) C_A - \frac{5}{3} \beta_0 - F^{(1)}(z) \right] \ln^2 x_H \\ + \left[\left(\frac{59}{9} - 2\zeta_3 \right) C_A^2 + \left(\frac{19}{9} - \frac{\pi^2}{3} \right) C_A \beta_0 - F^{(1)}(z) \beta_0 \right] \ln x_H. \quad (2.9)$$

The remaining μ_H -independent NNLO terms are contained in $F^{(2)}(z)$. Although these are known in an expansion in z , we do not include them, since the corresponding μ -independent NNLO terms are not known for the beam and soft functions.

To minimize the large logarithms in C_{ggH} we should evaluate eq. (2.7) at the hard scale μ_H with $|\mu_H^2| \sim q^2 \sim m_t^2$. For the simplest choice $\mu_H^2 = q^2$ the double logarithms of $-q^2/\mu_H^2$ are not minimized since they give rise to additional π^2 terms from the analytic continuation of the form factor from spacelike to timelike argument, $\ln^2(-1 - i0) = -\pi^2$, which causes rather large perturbative corrections. These π^2 terms can be summed along with the double logarithms by taking $\mu_H = -i\sqrt{q^2}$ or in our case $\mu_H = -im_H$ [80–83]. For Higgs production this method was applied in refs. [84, 85], where it was shown to improve the perturbative convergence of the hard matching coefficient. Starting at NNLO, the expansion of C_{ggH}

contains single logarithms $\ln(m_t^2/\mu_H^2)$, which in eq. (2.7) are contained as $\ln x_H$ in $C^{(2)}$ with a compensating $-\ln(-4z-i0)$ in $F^{(2)}(z)$, which are not large since $m_H/m_t \simeq 1$. In eq. (2.7), $\alpha_s(\mu_H)$ is defined for $n_f = 5$ flavors. When written in terms of $\alpha_s(\mu_H)$ with $n_f = 6$ flavors similar $\ln(m_t^2/m_H^2)$ terms would already appear at NLO. The additional terms that are induced by using an imaginary scale in these logarithms are small, because the imaginary part of $\alpha_s(-im_H)$ is much smaller than its real part.

The alternative two-step matching is briefly discussed in appendix B.1, where we compare results with the literature. In this case, one first integrates out the top quark at the scale m_t and then matches QCD onto SCET at the slightly lower scale $\mu_H \simeq m_H$. This allows one to sum the logarithms of m_H/m_t at the expense of neglecting m_H^2/m_t^2 corrections. Since parametrically $m_H/m_t \simeq 1$, we use the one-step matching above. Note that we do not include electroweak corrections whose predominant effect (of order 5%) is on the normalization of the cross section through the hard function [20–22, 62, 86, 87].

Given the hard matching coefficient at the scale μ_H we use its renormalization group evolution to obtain it at any other scale μ ,

$$H_{gg}(m_t, q^2, \mu) = H_{gg}(m_t, q^2, \mu_H) U_H(q^2, \mu_H, \mu), \quad (2.10)$$

where the evolution factor is given by

$$U_H(q^2, \mu_H, \mu) = \left| e^{K_H(\mu_H, \mu) \left(\frac{-q^2 - i0}{\mu_H^2} \right)^{\eta_H(\mu_H, \mu)}} \right|^2, \\ K_H(\mu_H, \mu) = -2K_\Gamma^g(\mu_H, \mu) + K_{\gamma_H^g}(\mu_H, \mu), \quad \eta_H(\mu_H, \mu) = \eta_\Gamma^g(\mu_H, \mu), \quad (2.11)$$

and the functions $K_\Gamma^g(\mu_H, \mu)$, $\eta_\Gamma^g(\mu_H, \mu)$, and $K_{\gamma_H^g}(\mu_H, \mu)$ are given in appendix B.3. They vanish for $\mu = \mu_H$ and therefore $U_H(q^2, \mu_H, \mu_H) = 1$, consistent with eq. (2.10).

2.2 Gluon Beam Function

The gluon beam function can be computed in an operator product expansion (OPE) in terms of standard gluon and quark PDFs (see appendix A.1 for more details),

$$B_g(t, x, \mu_B) = \sum_{j=\{g, q, \bar{q}\}} \int_x^1 \frac{d\xi}{\xi} \mathcal{I}_{gj} \left(t, \frac{x}{\xi}, \mu_B \right) f_j(\xi, \mu_B) \left[1 + \mathcal{O} \left(\frac{\Lambda_{\text{QCD}}^2}{t} \right) \right]. \quad (2.12)$$

In ref. [69] the \mathcal{I}_{gg} matching coefficient was computed at one loop in moment space. The \mathcal{I}_{gq} and $\mathcal{I}_{g\bar{q}}$ coefficients in the sum over j in eq. (2.12) describe the case where a quark or antiquark is taken out of the proton, it radiates a gluon which participates in the hard collision, and the quark or antiquark then continues into the final state. These mixing contributions start at one loop. Our one-loop calculation of \mathcal{I}_{gj} for $j = \{g, q, \bar{q}\}$, which are needed for the gluon beam function in the 0-jet Higgs cross section at NNLL, is given in some detail in appendix A and follows the analogous computation of the quark beam function in ref. [68].

We write the matching coefficients for the gluon beam function as

$$\begin{aligned}\mathcal{I}_{gg}(t, z, \mu_B) &= \delta(t) \delta(1 - z) + \frac{\alpha_s(\mu_B)}{4\pi} \mathcal{I}_{gg}^{(1)}(t, z, \mu_B) + \frac{\alpha_s^2(\mu_B)}{(4\pi)^2} \mathcal{I}_{gg}^{(2)}(t, z, \mu_B), \\ \mathcal{I}_{gq}(t, z, \mu_B) &= \frac{\alpha_s(\mu_B)}{4\pi} \mathcal{I}_{gq}^{(1)}(t, z, \mu_B) + \frac{\alpha_s^2(\mu_B)}{(4\pi)^2} \mathcal{I}_{gq}^{(2)}(t, z, \mu_B).\end{aligned}\tag{2.13}$$

Our calculation in appendix A yields the one-loop coefficients

$$\begin{aligned}\mathcal{I}_{gg}^{(1)}(t, z, \mu_B) &= 2C_A \theta(z) \left\{ \frac{2}{\mu_B^2} \mathcal{L}_1\left(\frac{t}{\mu_B^2}\right) \delta(1 - z) + \frac{1}{\mu_B^2} \mathcal{L}_0\left(\frac{t}{\mu_B^2}\right) P_{gg}(z) + \delta(t) \mathcal{I}_{gg}^{(1,\delta)}(z) \right\}, \\ \mathcal{I}_{gq}^{(1)}(t, z, \mu_B) &= 2C_F \theta(z) \left\{ \frac{1}{\mu_B^2} \mathcal{L}_0\left(\frac{t}{\mu_B^2}\right) P_{gq}(z) + \delta(t) \mathcal{I}_{gq}^{(1,\delta)}(z) \right\},\end{aligned}\tag{2.14}$$

where

$$\begin{aligned}\mathcal{I}_{gg}^{(1,\delta)}(z) &= \mathcal{L}_1(1 - z) \frac{2(1 - z + z^2)^2}{z} - P_{gg}(z) \ln z - \frac{\pi^2}{6} \delta(1 - z), \\ \mathcal{I}_{gq}^{(1,\delta)}(z) &= P_{gq}(z) \ln \frac{1 - z}{z} + \theta(1 - z) z.\end{aligned}\tag{2.15}$$

Here $P_{gg}(z)$ and $P_{gq}(z)$ are the $g \rightarrow gg$ and $q \rightarrow gq$ splitting functions given in eq. (A.16), and the $\mathcal{L}_n(x)$ denote the standard plus distributions,

$$\mathcal{L}_n(x) = \left[\frac{\theta(x) \ln^n x}{x} \right]_+, \tag{2.16}$$

defined in eq. (A.44). From eq. (2.14) we see that the proper scale to evaluate eq. (2.12) is $\mu_B^2 \simeq t \simeq \mathcal{T}_{\text{cm}} m_H$. For our final NNLL+NNLO result we also need the μ_B -dependent terms of the two-loop coefficients, contained in $\mathcal{I}_{gg}^{(2)}$ and $\mathcal{I}_{gq}^{(2)}$. They can be computed from the two-loop RGE of the \mathcal{I}_{gj} (see eq. (B.6)), which follows from the two-loop RGEs of the beam function and the PDFs. Our results for these coefficients are given in appendix B.2.

Our result for $\mathcal{I}_{gg}^{(1)}$ is converted to moment space in eq. (A.40), and except for a π^2 term, agrees with the corresponding moment space result given in eq. (68) of ref. [69]. Another comparison can be made by considering the correspondence with the p_T -dependent gluon beam function from ref. [51], which is given in impact parameter space y_T as $B_g(t_n, x, y_T, \mu) = \mathcal{I}_{gg}(t_n, x/\xi, y_T, \mu) \otimes f_g(\xi, \mu)$. Taking the $y_T \rightarrow 0$ limit of their bare result should yield agreement with our bare beam function. In principle the renormalization could change in this limit, but their results indicate that this is not the case. Translating their variable t_n into our variables, $t_n = t/z$, the $\lim_{y_T \rightarrow 0} \mathcal{I}_{gg}(t_n, z, y_T, \mu)$ from ref. [51] agrees with our result in eq. (2.14). In ref. [88] the authors changed their variable definition from t_n to our $t = t_n z$.⁵ Ref. [88] also calculates the other \mathcal{I}_{ij} coefficients at one loop. Our result for the mixing contribution $\mathcal{I}_{gq}^{(1)}$ disagrees with the $y_T \rightarrow 0$ limit of their \mathcal{I}_{gq} . In particular, their constant

⁵The translated result for \mathcal{I}_{gg} quoted in ref. [88] has a typo, it is missing a term $-\delta(t) P_{gg}(z) \ln z$ induced by rescaling $(1/\mu^2) \mathcal{L}_0(t_n/\mu^2) P_{gg}(z)$. We thank S. Mantry and F. Petriello for confirming this.

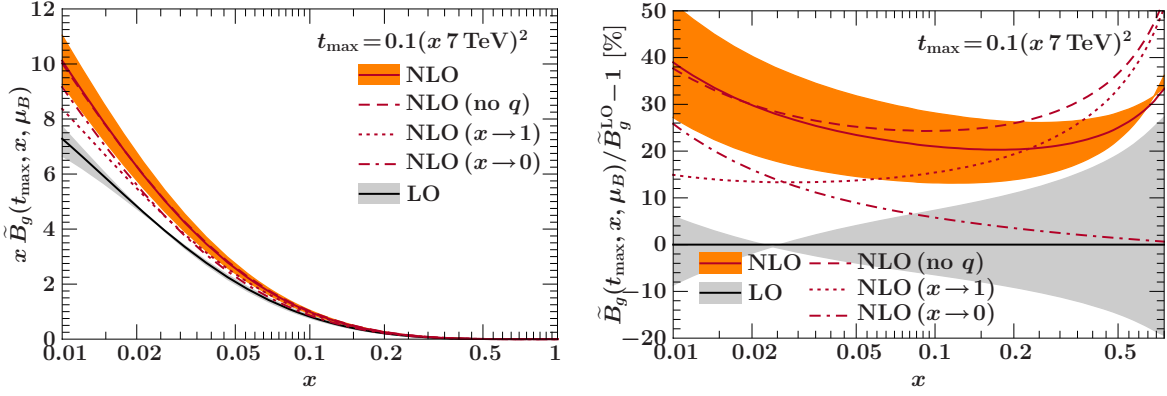


Figure 3. The gluon beam function integrated up to $t_{\max} = 0.1(x 7 \text{ TeV})^2$. The left plot shows $x\tilde{B}_g(t_{\max}, x, \mu_B)$. The right plot shows all results relative to the LO result. The solid lines show the LO and NLO results with the perturbative uncertainties shown by the bands. The dashed, dotted, and dot-dashed lines show the NLO result without quark contribution, in the large x limit, and the small x limit, respectively. See the text for further details.

term is $\mathcal{I}_{qq}^{(1,\delta)}(z) = -P_{qq}(z) \ln[(1-z)/z] + 2(1-z)/z$ which disagrees with ours in eq. (2.15). We have also compared the results of ref. [88] for the quark beam function for $y_T \rightarrow 0$ with our earlier results in refs. [56, 68]. The coefficient $\mathcal{I}_{qq}^{(1)}$ agrees, but the mixing term $\mathcal{I}_{qg}^{(1)}$ also disagrees. The $\lim_{y_T \rightarrow 0} \mathcal{I}_{qg}^{(1)}$ result in ref. [88] is missing a term $-\delta(t)P_{qg}(z)$ that is present in refs. [56, 68].

Given the beam function at the scale μ_B from eq. (2.12), we can evaluate it at any other scale using its renormalization group evolution [68]

$$B_g(t, x, \mu) = \int dt' B_g(t-t', x, \mu_B) U_B(t', \mu_B, \mu), \quad (2.17)$$

with the evolution kernel

$$U_B(t, \mu_B, \mu) = \frac{e^{K_B - \gamma_E \eta_B}}{\Gamma(1 + \eta_B)} \left[\frac{\eta_B}{\mu_B^2} \mathcal{L}^{\eta_B} \left(\frac{t}{\mu_B^2} \right) + \delta(t) \right],$$

$$K_B(\mu_B, \mu) = 4K_\Gamma^g(\mu_B, \mu) + K_{\gamma_B^g}(\mu_B, \mu), \quad \eta_B(\mu_B, \mu) = -2\eta_\Gamma^g(\mu_B, \mu). \quad (2.18)$$

The plus distribution $\mathcal{L}^\eta(x) = [\theta(x)/x^{1-\eta}]_+$ is defined in eq. (A.44), and the functions $K_\Gamma^g(\mu_B, \mu)$, $\eta_\Gamma^g(\mu_B, \mu)$, and $K_\gamma(\mu_B, \mu)$ are given in appendix B.3. Note that for $\mu = \mu_B$ we have $U_B(t, \mu_B, \mu_B) = \delta(t)$, which is consistent with eq. (2.17).

To illustrate our results for the gluon beam function we define its integral over $t \leq t_{\max}$,

$$\tilde{B}_g(t_{\max}, x, \mu_B) = \int dt B_g(t, x, \mu_B) \theta(t_{\max} - t). \quad (2.19)$$

In figure 3 we plot $\tilde{B}_g(t_{\max}, x, \mu_B)$ for a representative fixed value of $t_{\max} = 0.1(x 7 \text{ TeV})^2$. (Similar plots for the quark and antiquark beam functions can be found in refs. [56, 68].)

The left panel shows $x\tilde{B}_g(t_{\max}, x, \mu_B)$. The right panel shows the relative corrections to the LO result $\tilde{B}_g^{\text{LO}}(t_{\max}, x, \mu_B) = f_g(x, \mu_B)$. We use MSTW2008 NLO PDFs [64] with their $\alpha_s(m_Z) = 0.12018$ and two-loop, five-flavor running for α_s . The bands show the perturbative uncertainties from varying the matching scale μ_B . Since at the scale μ_B there are no large logarithms in the beam function, the μ_B variation can be used as an indicator of higher-order perturbative uncertainties. At LO the only scale variation is that of the PDF and the minimum and maximum scale variation are obtained by $\mu_B = \{\sqrt{t_{\max}}/2, 2\sqrt{t_{\max}}\}$ with $\mu_B = \sqrt{t_{\max}}$ the central value. At NLO the maximum variation does not occur at the endpoints of the range $\sqrt{t_{\max}}/2 \leq \mu_B \leq 2\sqrt{t_{\max}}$, but rather for approximately $\mu_B = \{0.8\sqrt{t_{\max}}, 2.0\sqrt{t_{\max}}\}$ with the central value at $\mu_B = 1.5\sqrt{t_{\max}}$. The α_s corrections to the gluon beam function are quite large, between 20% to 40%, which is significantly larger than the $\sim 10\%$ corrections to the quark beam function. The main reason for this is the larger color factor for gluons than quarks.

The size of the various perturbative contributions to the beam function is illustrated in figure 3. The dashed line shows the result obtained from \mathcal{I}_{gg} , without adding the mixing contribution \mathcal{I}_{gq} , using the same central value $\mu_B = 1.5\sqrt{t_{\max}}$. The mixing contributions are only relevant above $x \gtrsim 0.2$, and are suppressed at small x , because of their smaller color factor compared to \mathcal{I}_{gg} and the dominance of the gluon PDF at small x . This means they will be numerically small for a light Higgs.

The dotted line in figure 3 shows the result in the threshold limit (again for $\mu_B = 1.5\sqrt{t_{\max}}$), where we drop \mathcal{I}_{gq} and in addition only keep the terms in \mathcal{I}_{gg} that are singular as $z \rightarrow 1$, and which are expected to become dominant as $x \rightarrow 1$ in eq. (2.12),

$$\begin{aligned} \mathcal{I}_{gg}^{z \rightarrow 1}(t, z, \mu_B) = & \delta(t)\delta(1-z) + \frac{\alpha_s(\mu_B)}{2\pi} C_A \theta(z) \left\{ \frac{2}{\mu_B^2} \mathcal{L}_1\left(\frac{t}{\mu_B^2}\right) \delta(1-z) \right. \\ & \left. + \frac{2}{\mu_B^2} \mathcal{L}_0\left(\frac{t}{\mu_B^2}\right) \mathcal{L}_0(1-z) + \delta(t) \left[2\mathcal{L}_1(1-z) - \frac{\pi^2}{6} \delta(1-z) \right] \right\}. \end{aligned} \quad (2.20)$$

The dotted line indeed approaches the dashed line for $x \gtrsim 0.2$. However, since in this region the mixing contributions become important, the threshold result does not provide a good approximation to the full result (solid line) anywhere.

Finally, the dot-dashed line in figure 3 shows the result only keeping the terms singular as $z \rightarrow 0$ (but including tree level),

$$\begin{aligned} \mathcal{I}_{gg}^{z \rightarrow 0}(t, z, \mu_B) = & \delta(t)\delta(1-z) + \frac{\alpha_s(\mu_B)}{\pi} C_A \theta(z)\theta(1-z) \left[\frac{1}{\mu_B^2} \mathcal{L}_0\left(\frac{t}{\mu_B^2}\right) \frac{1}{z} - \delta(t) \frac{\ln z}{z} \right], \\ \mathcal{I}_{gq}^{z \rightarrow 0}(t, z, \mu_B) = & \frac{\alpha_s(\mu_B)}{\pi} C_F \theta(z)\theta(1-z) \left[\frac{1}{\mu_B^2} \mathcal{L}_0\left(\frac{t}{\mu_B^2}\right) \frac{1}{z} - \delta(t) \frac{\ln z}{z} \right], \end{aligned} \quad (2.21)$$

which one might expect to dominate for $x \rightarrow 0$. Since these only have single-logarithmic μ dependence, their central value is obtained for $\mu_B = \sqrt{t_{\max}}$. This contribution indeed grows towards smaller x , and makes up more than half of the total contribution at $x = 0.01$, but does not yet dominate.

2.3 Soft Function

The soft function $S_B^{gg}(k, \mu_S)$ appearing in eq. (2.2) is defined by the vacuum matrix element of a product of Wilson lines. For $k \simeq \mathcal{T}_{\text{cm}} \gg \Lambda_{\text{QCD}}$, it can be computed in perturbation theory. We write the perturbative soft function as

$$S_{\text{pert}}^{gg}(k, \mu_S) = \delta(k) + \frac{\alpha_s(\mu_S)}{\pi} C_A S_{gg}^{(1)}(k, \mu_S) + \frac{\alpha_s^2(\mu_S)}{\pi^2} C_A S_{gg}^{(2)}(k, \mu_S) + \mathcal{O}\left(\frac{\alpha_s^3}{k}\right), \quad (2.22)$$

where the one- and two-loop coefficients are

$$\begin{aligned} S_{gg}^{(1)}(k, \mu_S) &= -\frac{4}{\mu_S} \mathcal{L}_1\left(\frac{k}{\mu_S}\right) + \frac{\pi^2}{12} \delta(k), \\ S_{gg}^{(2)}(k, \mu_S) &= 8C_A \frac{1}{\mu_S} \mathcal{L}_3\left(\frac{k}{\mu_S}\right) + \beta_0 \frac{1}{\mu_S} \mathcal{L}_2\left(\frac{k}{\mu_S}\right) - \left[\left(\frac{4}{3} + \frac{8\pi^2}{3}\right) C_A + \frac{5}{3} \beta_0\right] \frac{1}{\mu_S} \mathcal{L}_1\left(\frac{k}{\mu_S}\right) \\ &\quad + \left[\left(\frac{8}{9} + \frac{25}{2} \zeta_3\right) C_A + \left(\frac{7}{9} - \frac{\pi^2}{12}\right) \beta_0\right] \frac{1}{\mu_S} \mathcal{L}_0\left(\frac{k}{\mu_S}\right) + S_{gg}^{(2,\delta)} \delta(k), \end{aligned} \quad (2.23)$$

In ref. [56] the quark beam-thrust soft function was obtained from the one-loop hemisphere soft function for outgoing jets [89, 90]. The gluon beam-thrust soft function has Wilson lines in the adjoint rather than fundamental representation and at one loop S_{pert}^{gg} is obtained from the quark result by simply replacing C_F by C_A . The μ_S -dependent terms needed at NNLL+NNLO are shown in eq. (2.23) and were obtained by perturbatively solving the two-loop RGE of the soft function (see eq. (B.13)). The determination of the μ_S -independent constant term, $S_{gg}^{(2,\delta)} \delta(k)$, requires the two-loop calculation of the soft function.

The RG evolution of the soft function has the same structure as that of the beam function,

$$S_B^{gg}(k, \mu) = \int dk' S_B^{gg}(k - k', \mu_S) U_S(k', \mu_S, \mu), \quad (2.24)$$

with the evolution kernel

$$\begin{aligned} U_S(k, \mu_S, \mu) &= \frac{e^{K_S - \gamma_E \eta_S}}{\Gamma(1 + \eta_S)} \left[\frac{\eta_S}{\mu_S} \mathcal{L}^{\eta_S}\left(\frac{k}{\mu_S}\right) + \delta(k) \right], \\ K_S(\mu_S, \mu) &= -4K_\Gamma^g(\mu_S, \mu) + K_{\gamma_S^g}(\mu_S, \mu), \quad \eta_S(\mu_S, \mu) = 4\eta_\Gamma^g(\mu_S, \mu), \end{aligned} \quad (2.25)$$

where $\mathcal{L}^\eta(x) = [\theta(x)/x^{1-\eta}]_+$ is defined in eq. (A.44), and $K_\Gamma^g(\mu_S, \mu)$, $\eta_\Gamma^g(\mu_S, \mu)$, and $K_\gamma(\mu_S, \mu)$ are given in appendix B.3.

The nonperturbative corrections can be modeled and included using the methods of refs. [75, 91]. The perturbative component S_{pert}^{gg} and nonperturbative component F^{gg} of the soft function can be factorized as

$$S_B^{gg}(k, \mu_S) = \int dk' S_{\text{pert}}^{gg}(k - k', \mu_S) F^{gg}(k'). \quad (2.26)$$

At small $\mathcal{T}_{\text{cm}} \sim \Lambda_{\text{QCD}}$ the nonperturbative corrections to the soft function are important. When the spectrum is dominated by perturbative momenta with $\mathcal{T}_{\text{cm}} \gg \Lambda_{\text{QCD}}$ eq. (2.26) can

be expanded in an OPE as

$$S_B^{gg}(k, \mu_S) = S_{\text{pert}}^{gg}(k, \mu_S) - 2\Omega_1^{gg} \frac{dS_{\text{pert}}^{gg}(k, \mu_S)}{dk} + \mathcal{O}\left(\frac{\Lambda_{\text{QCD}}^2}{k^3}\right), \quad (2.27)$$

where the leading power correction is determined by the dimension-one nonperturbative parameter $\Omega_1^{gg} = \int dk' (k'/2) F^{gg}(k')$ which is parametrically $\mathcal{O}(\Lambda_{\text{QCD}})$. The positivity of $F^{gg}(k)$ implies that $\Omega_1^{gg} > 0$, so the factorization in eq. (2.26) predicts the sign of the correction caused by the nonperturbative effects. We will see that this simple OPE result with one nonperturbative parameter Ω_1^{gg} gives an accurate description of the nonperturbative effects in the \mathcal{T}_{cm} spectra for the entire region we are interested in, which includes the peak in the distribution. The OPE in eq. (2.27) implies that the leading nonperturbative effects can be computed as an additive correction to the spectrum

$$\frac{d\sigma^s}{d\mathcal{T}_{\text{cm}}} = \frac{d\sigma_{\text{pert}}^s}{d\mathcal{T}_{\text{cm}}} - 2\Omega_1^{gg} \frac{d^2\sigma_{\text{pert}}^s}{d\mathcal{T}_{\text{cm}}^2}, \quad (2.28)$$

and likewise for the cumulant

$$\sigma^s(\mathcal{T}_{\text{cm}}^{\text{cut}}) = \sigma_{\text{pert}}^s(\mathcal{T}_{\text{cm}}^{\text{cut}}) - 2\Omega_1^{gg} \frac{d}{d\mathcal{T}_{\text{cm}}^{\text{cut}}} \sigma_{\text{pert}}^s(\mathcal{T}_{\text{cm}}^{\text{cut}}). \quad (2.29)$$

To first order in the OPE expansion this is equivalent to a shift in the variable used to evaluate the perturbative spectrum, $\mathcal{T}_{\text{cm}} \rightarrow \mathcal{T}_{\text{cm}} - 2\Omega_1^{gg}$, or cumulant, $\mathcal{T}_{\text{cm}}^{\text{cut}} \rightarrow \mathcal{T}_{\text{cm}}^{\text{cut}} - 2\Omega_1^{gg}$. For the cumulant the nonperturbative corrections always reduce the cross section, whereas the distribution is reduced before the peak and increased in the tail region. Since the nonsingular terms in the cross section are an order of magnitude smaller than the singular terms we can also replace σ^s by σ , that is include the nonsingular $d\sigma^{\text{ns}}/d\mathcal{T}_{\text{cm}}$ in eq. (2.28). For simplicity, we will use the purely perturbative result in most of our numerical analysis. However, in section 2.8 we will use eqs. (2.26) and (2.28) to analyze the effect of nonperturbative corrections on our predictions.

2.4 Nonsingular Contributions

In this section we discuss how we incorporate the nonsingular contributions to the cross section using fixed-order perturbation theory. For the two beam thrust cross sections considered in this paper, the full cross section in fixed-order perturbation theory can be written as

$$\begin{aligned} \frac{d\sigma}{d\tau dY} &= \sigma_0 \alpha_s^2(\mu) \left| F^{(0)}\left(\frac{m_H^2}{4m_t^2}\right) \right|^2 \\ &\times \int \frac{d\xi_a}{\xi_a} \frac{d\xi_b}{\xi_b} \sum_{i,j} C_{ij}\left(\frac{x_a}{\xi_a}, \frac{x_b}{\xi_b}, \tau, Y, \mu, m_H, m_t\right) f_i(\xi_a, \mu) f_j(\xi_b, \mu), \end{aligned} \quad (2.30)$$

where $i, j = g, q, \bar{q}$ sum over parton types, and $\tau = \mathcal{T}_{\text{cm}}/m_H$.⁶ To simplify the notation in the following we will suppress the m_H and m_t dependence of the coefficients C_{ij} . The

⁶For $H \rightarrow \gamma\gamma$ where the boost between the partonic and hadronic center-of-mass frames is accounted for with $\tau_B = \mathcal{T}_B/m_H$, the appropriate replacements in eq. (2.30) are to take $\tau \rightarrow \tau_B$, and in the fourth argument of C_{ij} to set $Y = 0$.

contributions to the C_{ij} can be separated into singular and nonsingular parts,

$$C_{ij}(z_a, z_b, \tau, Y, \mu) = C_{ij}^s(z_a, z_b, \tau, Y, \mu) + C_{ij}^{\text{ns}}(z_a, z_b, \tau, Y, \mu), \quad (2.31)$$

where the singular terms scale as $\sim 1/\tau$ modulo logarithms and can be written as

$$C_{ij}^s(z_a, z_b, \tau, Y, \mu) = C_{ij}^{-1}(z_a, z_b, Y, \mu) \delta(\tau) + \sum_{k \geq 0} C_{ij}^k(z_a, z_b, Y, \mu) \mathcal{L}_k(\tau), \quad (2.32)$$

where $\mathcal{L}_k(\tau) = [\theta(\tau)(\ln^k \tau)/\tau]_+$ is defined in eq. (A.44). The resummed result for the cross section in eq. (2.2) sums the singular contributions at small τ to all orders, counting $(\alpha_s \ln \tau) \sim 1$. The nonsingular contributions, C_{ij}^{ns} , are suppressed relative to the singular ones by $\mathcal{O}(\tau)$ and it suffices to determine them in fixed-order perturbation theory. Hence, we can obtain them by simply subtracting the fixed-order expansion of the singular result from the full fixed-order result,

$$\frac{d\sigma^{\text{ns,FO}}}{d\tau} = \frac{d\sigma^{\text{FO}}}{d\tau} - \frac{d\sigma^{\text{s,FO}}}{d\tau}, \quad (2.33)$$

and analogously for the cumulant

$$\sigma^{\text{ns,FO}}(\tau^{\text{cut}}) = \sigma^{\text{FO}}(\tau^{\text{cut}}) - \sigma^{\text{s,FO}}(\tau^{\text{cut}}). \quad (2.34)$$

We must take care to use the same PDFs and renormalization scale μ for both the σ^{FO} and $\sigma^{\text{s,FO}}$ terms. In our analysis we obtain $\sigma^{\text{NLO}}(\tau^{\text{cut}})$ and $\sigma^{\text{NNLO}}(\tau^{\text{cut}})$ numerically using the publicly available FEHiP program [27, 43], which allows one to obtain the fixed-order NNLO Higgs production cross section for generic phase-space cuts.

At tree level, the only nonzero coefficient is C_{ij}^{-1} , and the nonsingular contribution vanishes, $\sigma^{\text{ns,LO}}(\tau^{\text{cut}}) = 0$. At NLO, the C_{ij}^k are nonzero for $k \leq 1$ and are fully contained in the resummed NNLL result for $d\sigma^{\text{s}}/d\tau$. Hence, we can obtain them by expanding our NNLL singular result to fixed next-to-leading order,

$$\sigma^{\text{s,NLO}}(\tau^{\text{cut}}) = \sigma^{\text{s,NNLL}}(\tau^{\text{cut}})|_{\text{NLO}}. \quad (2.35)$$

The explicit expressions are given in appendix B.4. Subtracting this from the full NLO result we get the nonsingular contribution at NLO,

$$\sigma^{\text{ns,NLO}}(\tau^{\text{cut}}) = \sigma^{\text{NLO}}(\tau^{\text{cut}}) - \sigma^{\text{s,NNLL}}(\tau^{\text{cut}})|_{\text{NLO}}. \quad (2.36)$$

In the left panel of figure 4 we plot the NLO nonsingular cross section determined by this procedure for three different choices of μ , namely $\mu = m_H/2, m_H, 2m_H$. The scaling of the nonsingular distribution implies that it involves only integrable functions, therefore the cumulant $\sigma^{\text{ns,NLO}}(\tau^{\text{cut}})$ vanishes for $\tau^{\text{cut}} \rightarrow 0$. The μ dependence of the NLO nonsingular cross section is sizeable since this is the leading term in this part of the cross section. This μ dependence is canceled by the nonsingular terms at NNLO which we turn to next.

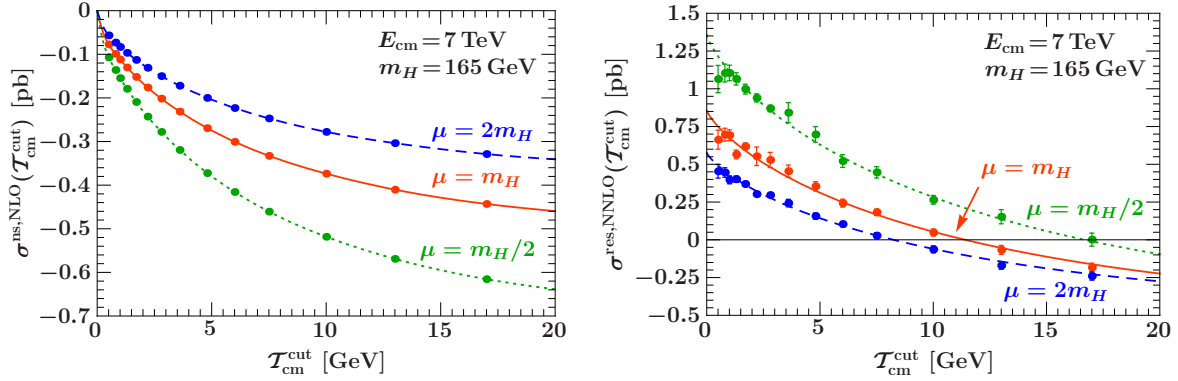


Figure 4. The left panel shows the nonsingular contribution to the NLO cross section as a function of $\mathcal{T}_B^{\text{cm,cut}}$, for the LHC at 7 TeV. The residual NNLO cross section shown in the right panel, is the nonsingular NNLO cross section, $\sigma^{\text{ns,NNLO}}$, plus a constant term c^{res} , as explained in the text.

At NNLO the singular cross section is determined by a result analogous to eq. (2.35)

$$\sigma^{\text{s,NNLO}}(\tau^{\text{cut}}) = \sigma^{\text{s,NNLL}}(\tau^{\text{cut}})|_{\text{NNLO},k \geq 0} + \sigma^{\text{s,NNLO}}|_{k=-1}. \quad (2.37)$$

The NNLO singular coefficients C_{ij}^k are nonzero for $-1 \leq k \leq 3$. Those for $k \geq 0$ can be obtained by expanding the singular NNLL result to fixed NNLO. Their explicit expressions are given in appendix B.4. For $k = -1$ the NNLO contribution to the coefficient C_{ij}^{-1} of the $\delta(\tau)$ is not fully contained in the NNLL result. Therefore, the τ^{cut} -independent $k = -1$ contribution is not included in the first term on the right-hand side of eq. (2.37), but in the second term. For this second term we proceed as follows.

First, we write the NNLO contribution to C_{ij}^{-1} as

$$C_{ij}^{-1}(z_a, z_b, Y, \mu)|_{\text{NNLO}} = \frac{\alpha_s^2(\mu)}{(2\pi)^2} \left[c_{ij}^\pi(z_a, z_b, Y) + c_{ij}^\mu(z_a, z_b, Y, \mu) + c_{ij}^{\text{res}}(z_a, z_b, Y) \right]. \quad (2.38)$$

The first term in brackets denotes the μ -independent terms proportional to π^2 that are part of the π^2 summation. The second term contains all terms proportional to $\ln(\mu/m_H)$, which cancel the μ dependence in the NLO result. We can obtain these two contributions analytically, and they are given in appendix B.4. The remaining μ -independent terms, c_{ij}^{res} , are currently not known analytically. They could be obtained when the complete NNLO results for the hard, beam, and soft functions become available. Using eq. (2.38), the second term on the right-hand side of eq. (2.37) is given by

$$\sigma^{\text{s,NNLO}}|_{k=-1} = c^\pi(\mu) + c^\mu(\mu) + c^{\text{res}}(\mu), \quad (2.39)$$

with $(x = \{\pi, \mu, \text{res}\})$

$$c^x(\mu) = \sigma_0 \frac{\alpha_s^4(\mu)}{(2\pi)^2} \left| F^{(0)}\left(\frac{m_H^2}{4m_t^2}\right) \right|^2 \int dY \int \frac{d\xi_a}{\xi_a} \frac{d\xi_b}{\xi_b} \sum_{i,j} c_{ij}^x\left(\frac{x_a}{\xi_a}, \frac{x_b}{\xi_b}, Y, \mu\right) f_i(\xi_a, \mu) f_j(\xi_b, \mu). \quad (2.40)$$

The μ dependence of $c^\mu(\mu)$ cancels that of $\sigma^{\text{ns,NNLO}}(\tau^{\text{cut}})$ up to terms of $\mathcal{O}(\alpha_s^5)$, whereas that of $c^\pi(\mu)$ and $c^{\text{res}}(\mu)$ only starts at $\mathcal{O}(\alpha_s^5)$. Since $x_{a,b} = (m_H/E_{\text{cm}})e^{\pm Y}$, the $c^x(\mu)$ have a nontrivial dependence on m_H .

To determine the constant c^{res} numerically, we now consider

$$\sigma^{\text{res}}(\tau^{\text{cut}}) \equiv \sigma^{\text{NNLO}}(\tau^{\text{cut}}) - \sigma^{\text{s,NNLL}}(\tau^{\text{cut}}) \Big|_{\text{NNLO}, k \geq 0} - c^\pi - c^\mu = c^{\text{res}} + \sigma^{\text{ns,NNLO}}(\tau^{\text{cut}}). \quad (2.41)$$

Since $\sigma^{\text{ns,NNLO}}(\tau^{\text{cut}})$ vanishes as $\tau^{\text{cut}} \rightarrow 0$, the coefficient c^{res} is determined by $\sigma^{\text{res}}(\tau^{\text{cut}})$ as $\tau^{\text{cut}} \rightarrow 0$, while the nonsingular corrections are given by the remainder $\sigma^{\text{res}}(\tau^{\text{cut}}) - c^{\text{res}}$. Hence, we can obtain both by fitting our numerical results for $\sigma^{\text{res}}(\tau^{\text{cut}})$ at different values of τ^{cut} to the following function:

$$\sigma^{\text{res}}(\tau) = c^{\text{res}} + a_0 \tau \ln \tau + a_1 \tau + a_2 \tau^2 \ln \tau + a_3 \tau^2. \quad (2.42)$$

The a_0 through a_3 terms are sufficient to describe the τ^{cut} dependence of $\sigma^{\text{ns,NNLO}}(\tau^{\text{cut}})$ over the whole range of τ^{cut} . The results of the fit for pp collisions at 7 TeV and $m_H = 165$ GeV for $\mu = m_H$, $\mu = m_H/2$, and $\mu = 2m_H$ are shown in the right panel of figure 4. At $\mu = m_H$ this fit gives

$$c^{\text{res}} = 0.86 \pm 0.02, \quad a_0 = 7.6 \pm 0.6, \quad a_1 = 9.3 \pm 1.5, \quad a_2 = 3.9 \pm 1.1, \quad a_3 = -9.9 \pm 1.6. \quad (2.43)$$

Similarly, for $p\bar{p}$ collisions at 1.96 TeV, $m_H = 165$ GeV, and $\mu = m_H$, we obtain

$$c^{\text{res}} = 0.028 \pm 0.001, \quad a_0 = 0.28 \pm 0.03, \quad a_1 = 0.44 \pm 0.08, \quad a_2 = 0.18 \pm 0.06, \\ a_3 = -0.42 \pm 0.08. \quad (2.44)$$

We have checked that we obtain the same values for c^{res} within the uncertainties when the fit range is restricted to the region of small τ^{cut} . (In this case the fit is not sensitive to a_2 and a_3 , so either one or both of them must be set to zero.) Note that $\sigma^{\text{NNLO}}(\tau^{\text{cut}})$ and $\sigma^{\text{s,NNLL}}|_{\text{NNLO}}$ both diverge as $\tau^{\text{cut}} \rightarrow 0$. The fact that the difference in $\sigma^{\text{res}}(\tau^{\text{cut}})$ does not diverge for $\tau^{\text{cut}} \rightarrow 0$ provides an important cross check between our analytic results for the NNLO singular terms and the full numerical NNLO result. The numerical uncertainty from fitting $c^{\text{res}}(\mu)$ is much smaller than its μ dependence, and so can be ignored for our final error analysis. The μ dependence of $c^{\text{res}}(\mu)$ comes from the PDFs and the overall $\alpha_s^4(\mu)$, where the latter is by far the dominant effect. To see this we can rescale $c^{\text{res}}(m_H/2) = 1.35$ and $c^{\text{res}}(2m_H) = 0.58$ as $c^{\text{res}}(m_H/2)\alpha_s^4(m_H)/\alpha_s^4(m_H/2) = 0.91$ and $c^{\text{res}}(2m_H)\alpha_s^4(m_H)/\alpha_s^4(2m_H) = 0.83$, giving values that are very close to the central value $c^{\text{res}}(m_H) = 0.86$.

Having determined the nonsingular contributions to the cross section we can compare their size to the dominant singular terms. In figure 5 we plot the singular, nonsingular, and full cross sections at NNLO for $\mu = m_H$. The left panel shows the absolute value of these components of the differential cross sections (obtained by taking the derivative of $\sigma(\tau^{\text{cut}})$ with respect to τ^{cut}). For $\mathcal{T}_{\text{cm}} \ll m_H$ the nonsingular terms are an order of magnitude smaller than

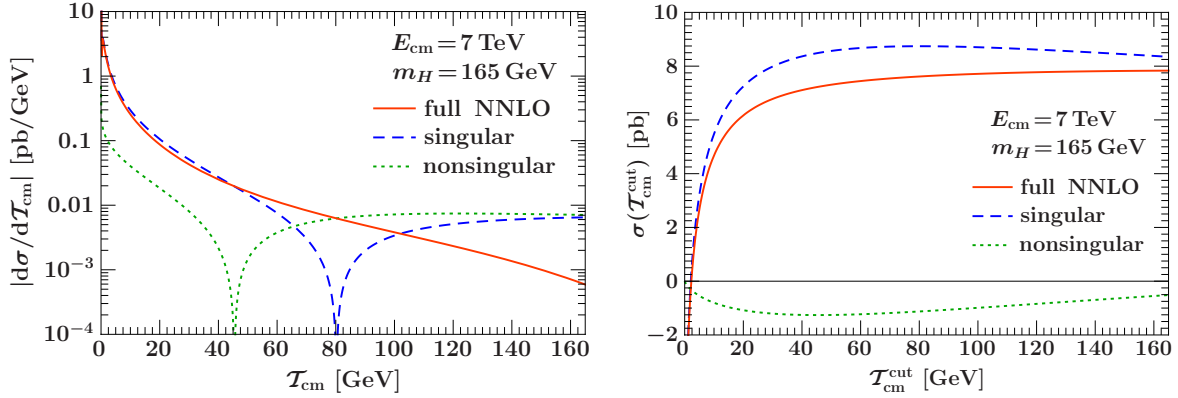


Figure 5. Comparison of the singular, nonsingular, and full cross sections at NNLO for $\mu = m_H$. The left panel shows the magnitude of the differential cross sections on a logarithmic scale. The right panel shows the corresponding cumulant cross sections.

the singular ones. On the other hand for $\mathcal{T}_{\text{cm}} \gtrsim m_H/2$ the singular and nonsingular terms become equally important and there is a large cancellation between the two contributions. These features of the fixed-order cross section will have implications on our choice of running scales discussed in section 2.6.

To determine the singular NNLO contributions in eq. (2.37) for the above analysis we only considered the $k \geq 0$ terms contained in $\sigma^{s,\text{NNLL}}$. Of course $\sigma^{s,\text{NNLL}}$ also contains some $k = -1$ terms at NNLO, in particular the $c^\pi(\mu)$ and $c^\mu(\mu)$ contributions, but also parts of the $c^{\text{res}}(\mu)$ contribution from cross terms between the NLO matching corrections. Since we know $c^{\text{res}}(\mu)$ numerically, we are able to determine the missing $k = -1$ contribution at NNLO numerically, which corresponds to the sum of the unknown μ -independent NNLO matching corrections to the hard, beam, and soft functions. It is given by the difference

$$c^\delta(\mu) = \sigma^{s,\text{NNLO}} - \sigma^{s,\text{NNLL}} \Big|_{\text{NNLO}} = c^\pi(\mu) + c^\mu(\mu) + c^{\text{res}}(\mu) - \sigma^{s,\text{NNLL}} \Big|_{\text{NNLO}, k=-1}. \quad (2.45)$$

Since we include the μ -dependent NNLO matching corrections in $\sigma^{s,\text{NNLL}}$, its NNLO expansion is obtained by setting $\mu_S = \mu_B = \mu_H = \mu$. Thus, we can easily evaluate eq. (2.45) numerically. For $m_H = 165$ GeV, we find for the LHC at 7 TeV,

$$c^\delta(m_H/2) = 0.002, \quad c^\delta(m_H) = -0.035, \quad c^\delta(2m_H) = -0.028, \quad (2.46)$$

and for the Tevatron,

$$c^\delta(m_H/2) = -0.0043, \quad c^\delta(m_H) = -0.0026, \quad c^\delta(2m_H) = -0.0027. \quad (2.47)$$

Comparing this to $c^{\text{res}}(m_H) = 0.86$ (LHC) and $c^{\text{res}}(m_H) = 0.028$ (Tevatron), we see that these coefficients are almost fully accounted for by cross terms between the NLO hard, beam, and soft functions. The remaining NNLO terms in c^δ are in fact very small, and our NNLL+NNLO results are therefore numerically very close to the complete NNLL'+NNLO result.

2.5 Cross Section at NNLL+NNLO

Using the results of sections 2.1 to 2.4 our final result at NNLL+NNLO for the distribution and cumulant is obtained as

$$\begin{aligned} \frac{d\sigma^{\text{NNLL+NNLO}}}{d\mathcal{T}_{\text{cm}}} &= \frac{d\sigma^{\text{s,NNLL}}}{d\mathcal{T}_{\text{cm}}} + \frac{d\sigma^\delta}{d\mathcal{T}_{\text{cm}}} + \frac{d\sigma^{\text{ns,NNLO}+\pi^2}}{d\mathcal{T}_{\text{cm}}}, \\ \sigma^{\text{NNLL+NNLO}}(\mathcal{T}_{\text{cm}}^{\text{cut}}) &= \sigma^{\text{s,NNLL}}(\mathcal{T}_{\text{cm}}^{\text{cut}}) + \sigma^\delta(\mathcal{T}_{\text{cm}}^{\text{cut}}) + \sigma^{\text{ns,NNLO}+\pi^2}(\mathcal{T}_{\text{cm}}^{\text{cut}}). \end{aligned} \quad (2.48)$$

The first term in each equation contains the resummed singular result obtained from eq. (2.2) to NNLL order, including the μ -dependent NNLO matching corrections. The last term contains the NNLO nonsingular corrections determined in the previous subsection, but including π^2 summation by using

$$\begin{aligned} \frac{d\sigma^{\text{ns,NNLO}+\pi^2}}{d\mathcal{T}_{\text{cm}}} &= U_H(m_H^2, -i\mu_{\text{ns}}, \mu_{\text{ns}}) \left[\frac{d\sigma^{\text{ns,NNLO}}}{d\mathcal{T}_{\text{cm}}} - \frac{\alpha_s(\mu_{\text{ns}})C_A}{2\pi} \pi^2 \frac{d\sigma^{\text{ns,NLO}}}{d\mathcal{T}_{\text{cm}}} \right], \\ \sigma^{\text{ns,NNLO}+\pi^2}(\mathcal{T}_{\text{cm}}^{\text{cut}}) &= U_H(m_H^2, -i\mu_{\text{ns}}, \mu_{\text{ns}}) \left[\sigma^{\text{ns,NNLO}}(\mathcal{T}_{\text{cm}}^{\text{cut}}) - \frac{\alpha_s(\mu_{\text{ns}})C_A}{2\pi} \pi^2 \sigma^{\text{ns,NLO}}(\mathcal{T}_{\text{cm}}^{\text{cut}}) \right]. \end{aligned} \quad (2.49)$$

Here $U_H(m_H^2, -i\mu_{\text{ns}}, \mu_{\text{ns}}) = \exp[\alpha_s(\mu_{\text{ns}})C_A\pi/2 + \dots]$ contains the π^2 summation. There are two reasons we include the π^2 summation for the nonsingular terms. First, using SCET one can derive factorization theorems for the nonsingular terms when $\mathcal{T}_{\text{cm}} \ll m_H$, and the results will involve a combination of leading and subleading hard, jet, and soft functions. Many of these terms will have the same LL evolution for their hard functions, and hence they predominantly require the same π^2 summation. As a second reason we observe from figure 5 that there are important cancellations between the singular and nonsingular cross sections for $\mathcal{T}_{\text{cm}} \gtrsim m_H/2$. Since the π^2 summation modifies the cross section for all \mathcal{T}_{cm} and $\mathcal{T}_{\text{cm}}^{\text{cut}}$ values it is important to include it also in the nonsingular terms to not spoil these cancellations.

The middle terms in eq. (2.48) incorporate the singular NNLO terms that are not reproduced by our resummed NNLL result. At fixed order, they are given by

$$\left. \frac{d\sigma^\delta}{d\mathcal{T}_{\text{cm}}} \right|_{\text{NNLO}} = c^\delta(\mu) \delta(\mathcal{T}_{\text{cm}}), \quad \left. \sigma^\delta(\mathcal{T}_{\text{cm}}^{\text{cut}}) \right|_{\text{NNLO}} = c^\delta(\mu). \quad (2.50)$$

As we saw in section 2.4, $c^\delta(\mu)$ turns out to be very small numerically, which means we might as well neglect the σ^δ term entirely. We include it for completeness in eq. (2.48), in order to formally reproduce the complete NNLO cross section. In fact, at this level other contributions that we neglect here, such as the bottom-quark contributions or electroweak corrections, are likely more relevant numerically.

Formally, $c^\delta(\mu)$ is reproduced by the complete two-loop matching required at NNLL' or N³LL. When it is properly incorporated into the predictions at that order it is multiplied by a Sudakov exponent that ensures that the total $\sigma(\mathcal{T}_{\text{cm}}^{\text{cut}}) \rightarrow 0$ as $\mathcal{T}_{\text{cm}}^{\text{cut}} \rightarrow 0$. Hence, we can

include it in the resummed result by multiplying it with the NNLL evolution factors,

$$\frac{d\sigma^\delta}{d\mathcal{T}_{\text{cm}}} = c^\delta(\mu_{\text{ns}}) U_H(m_H^2, \mu_H, \mu) \int dt_a dt_b U_B^g(t_a, \mu_B, \mu) U_B^g(t_b, \mu_B, \mu) U_S\left(\mathcal{T}_{\text{cm}} - \frac{t_a + t_b}{m_H}, \mu_S, \mu\right). \quad (2.51)$$

The scale where we evaluate $c^\delta(\mu)$ here is an N³LL effect, and so beyond the order we are working. We choose $\mu = \mu_{\text{ns}}$, which is the scale at which we evaluate $\sigma^{\text{ns}}(\mathcal{T}_{\text{cm}}^{\text{cut}})$.

2.6 Choice of Running Scales

The factorization theorem in eq. (2.2) resums the singular cross section by evaluating the hard, beam, and soft function at their natural scales $\mu_H \simeq -im_H$, $\mu_B \simeq \sqrt{\tau}m_H$, $\mu_S \simeq \tau m_H$ where they have no large logarithms in fixed-order perturbation theory. Their renormalization group evolution is then used to connect these functions at a common scale. This resums logarithms in the ratios of μ_H , μ_B , and μ_S , which are logarithms of τ . The τ -spectrum has three distinct kinematic regions where this resummation must be handled differently and we will do so using τ -dependent scales given by profile functions $\mu_S(\tau)$ and $\mu_B(\tau)$. Profile functions of this type have been previously used to analyze the $B \rightarrow X_s \gamma$ spectrum [75] and the thrust event shape in $e^+e^- \rightarrow \text{jets}$ [92].

For $\Lambda_{\text{QCD}}/m_H \ll \tau \ll 1$ the scales μ_H , μ_B , μ_S , and Λ_{QCD} are all widely separated and the situation is as described above. We define this region to be $\tau_1 < \tau < \tau_2$. In the $\tau < \tau_1$ region the scale μ_S drops below 1 GeV, we have $\Lambda_{\text{QCD}}/m_H \sim \tau$, and nonperturbative corrections to the soft function become important. In this case the scales are $\mu_H \simeq -im_H$, $\mu_B \simeq \sqrt{\Lambda_{\text{QCD}}m_H}$, and $\mu_S \simeq \Lambda_{\text{QCD}}$.

Finally for $\tau > \tau_2$ we have $\tau \sim 1$, the resummation is not important, and the nonsingular corrections, which are evaluated at a fixed scale μ_{ns} , become just as important as the singular corrections. In this region there is only one scale $i\mu_H = \mu_B = \mu_S = \mu_{\text{ns}} \simeq m_H$. Furthermore it is known from $B \rightarrow X_s \gamma$ and thrust [75, 92] that there can be important cancellations between the singular and nonsingular terms in this limit, and that to ensure these cancellations take place the scales $\mu_B(\tau)$ and $\mu_S(\tau)$ must converge to $|\mu_H| = \mu_{\text{ns}}$ in a region, rather than at a single point. To ensure this we make the approach to μ_H quadratic for $\tau_2 < \tau < \tau_3$ and set $\mu_B(\tau) = \mu_S(\tau) = i\mu_H$ for $\tau \geq \tau_3$ (recall that $i\mu_H > 0$). As we saw in section 2.4, the singular and nonsingular contributions in our case become equally important for $\tau \gtrsim 1/2$. Accordingly, we choose the profile functions such that the scales converge around this value and stay equal for larger τ .

A transition between these three regions is given by the following running scales

$$\begin{aligned} \mu_H &= -i\mu, \\ \mu_B(\tau) &= \left[1 + e_B \theta(\tau_3 - \tau) \left(1 - \frac{\tau}{\tau_3}\right)^2\right] \sqrt{\mu \mu_{\text{run}}(\tau, \mu)}, \\ \mu_S(\tau) &= \left[1 + e_S \theta(\tau_3 - \tau) \left(1 - \frac{\tau}{\tau_3}\right)^2\right] \mu_{\text{run}}(\tau, \mu), \\ \mu_{\text{ns}} &= \mu. \end{aligned} \quad (2.52)$$

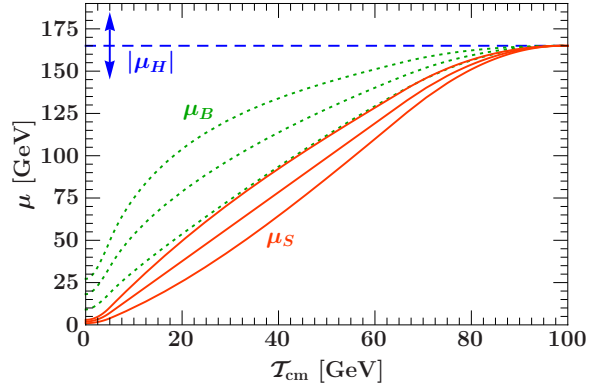


Figure 6. Profiles for the running scales μ_H , μ_B , and μ_S . The central lines for μ_B and μ_S show our central scale choices. The upper and lower curves for μ_B and μ_S correspond to their respective variations b) and c) in eq. (2.55).

For the profile $\mu_{\text{run}}(\tau, \mu)$ we use a combination of two quadratic functions and a linear function as in ref. [92]. For $\tau > \tau_3$ our choice for $\mu_{\text{run}}(\tau, \mu)$ ensures that our cross section formula becomes precisely the fixed-order result.

$$\mu_{\text{run}}(\tau, \mu) = \begin{cases} \mu_0 + a\tau^2/\tau_1 & \tau \leq \tau_1, \\ 2a\tau + b & \tau_1 \leq \tau \leq \tau_2, \\ \mu - a(\tau - \tau_3)^2/(\tau_3 - \tau_2) & \tau_2 \leq \tau \leq \tau_3, \\ \mu & \tau > \tau_3, \end{cases} \quad (2.53)$$

$$a = \frac{\mu_0 - \mu}{\tau_1 - \tau_2 - \tau_3}, \quad b = \frac{\mu\tau_1 - \mu_0(\tau_2 + \tau_3)}{\tau_1 - \tau_2 - \tau_3}.$$

The expressions for a and b follow from demanding that $\mu_{\text{run}}(\tau)$ is continuous and has a continuous derivative. The value of μ_0 determines the scales at $\tau = 0$, while $\tau_{1,2,3}$ determine the transition between the regions discussed above. For our central value we use the following choice of parameters

$$\mu = m_H, \quad e_B = e_S = 0, \quad \mu_0 = 2 \text{ GeV}, \quad \tau_1 = \frac{5 \text{ GeV}}{m_H}, \quad \tau_2 = 0.4, \quad \tau_3 = 0.6. \quad (2.54)$$

The corresponding running scales are shown in figure 6.

Since the factorization theorem is not affected by $\mathcal{O}(1)$ changes of the renormalization scales, we should vary them to determine the perturbative uncertainty. For a reasonable variation of the above parameters, the cross section is most sensitive to μ , e_B and e_S . We therefore estimate our uncertainties from higher order terms in perturbation theory by taking the envelope of the following three separate variations,

$$\begin{aligned} \text{a)} \quad & \mu = 2^{\pm 1} m_H, & e_B = 0, & e_S = 0, \\ \text{b)} \quad & \mu = m_H, & e_B = \pm 0.5, & e_S = 0, \\ \text{c)} \quad & \mu = m_H, & e_B = 0, & e_S = \pm 0.5. \end{aligned} \quad (2.55)$$

The effect of variations b) and c) are shown in figure 6 by the upper and lower curves for μ_B and μ_S , respectively. The effect of variation a) is to change the overall vertical scale of the $|\mu_H|$, μ_B , and μ_S curves in figure 6 by a factor of 1/2 or 2 as indicated by the arrows. In predictions based on fixed-order perturbation theory only a scale variation analogous to a) can be considered.

2.7 PDFs and π^2 Summation

In this subsection we briefly discuss the choice of the order of the PDFs for our resummed results and the effect of the π^2 summation.

As shown in table 1, by default we use the PDFs that correspond to the order of the matching corrections, namely LO PDFs at NLL and NLO PDFs at NNLL. Since the MSTW2008 PDFs [93] are extracted simultaneously with the value of $\alpha_s(m_Z)$, by using PDFs at different orders we are forced to also use different values of $\alpha_s(m_Z)$. Our NNLL+NNLO results contain two-loop corrections and so at this order our default is to use the MSTW2008 PDFs [93] at NNLO with their $\alpha_s(m_Z) = 0.11707$ and with three-loop, five-flavor running for $\alpha_s(\mu)$. For our NLL'+NLO and NNLL results, which include one-loop matching, we use the corresponding NLO PDFs with their $\alpha_s(m_Z) = 0.12018$ and two-loop, five-flavor running for $\alpha_s(\mu)$. At LL and NLL, which only includes tree-level matching, we use the LO PDFs with $\alpha_s(m_Z) = 0.13939$ and one-loop, five-flavor running for $\alpha_s(\mu)$.

Note that at NLL (NNLL) there is a slight mismatch in the required running of $\alpha_s(\mu)$. The resummation at this order requires two-loop (three-loop) $\alpha_s(\mu)$ running, whereas the used LO (NLO) PDFs employ one-loop (two-loop) running of $\alpha_s(\mu)$. In this case, we use the following compromise. We use the appropriate $\alpha_s(m_Z)$ and running consistent with the PDF set to obtain the numerical value of α_s at some required scale. At the same time, in the NLL (NNLL) RGE solutions we use the QCD β function at the appropriate one higher loop order to be consistent with the RGE. There is no such mismatch in the α_s running at LL, NLL'+NLO, and NNLL+NNLO, and hence no mismatch for our highest order predictions.

Various results which test the effect of π^2 resummation and the treatment of PDFs are shown for the cumulant cross section, $\sigma(\mathcal{T}_{\text{cm}}^{\text{cut}})$, for $m_H = 165$ GeV in figure 7. The left panel shows the Tevatron case and right panel shows the LHC with $E_{\text{cm}} = 7$ TeV. The lower four blue curves show the NLL and the upper two orange curves the NNLL results. (The nonsingular corrections do not affect this discussion much, so for simplicity we do not include them in this figure.) The solid lines correspond to our default results, while the dashed, dot-dashed, and dotted are variations with other choices for the PDFs or π^2 summation.

As discussed in section 2.1, the hard function contains large $\alpha_s^n \pi^{2m}$ terms, with $m \leq n$, which in our default results are summed by evaluating the hard function at $\mu_H = -im_H$. The π^2 summation is switched off by taking $\mu_H = m_H$ instead, which is shown by the dotted lines in figure 7. The effect of π^2 summation is very large. It almost doubles the NLL cross section and increases the NNLL cross section by about 30%. From the fact that the NLL results with π^2 summation (blue solid line) is very close to the NNLL result without π^2 summation (orange dotted line) we can conclude that the large corrections from NLL to NNLL are caused

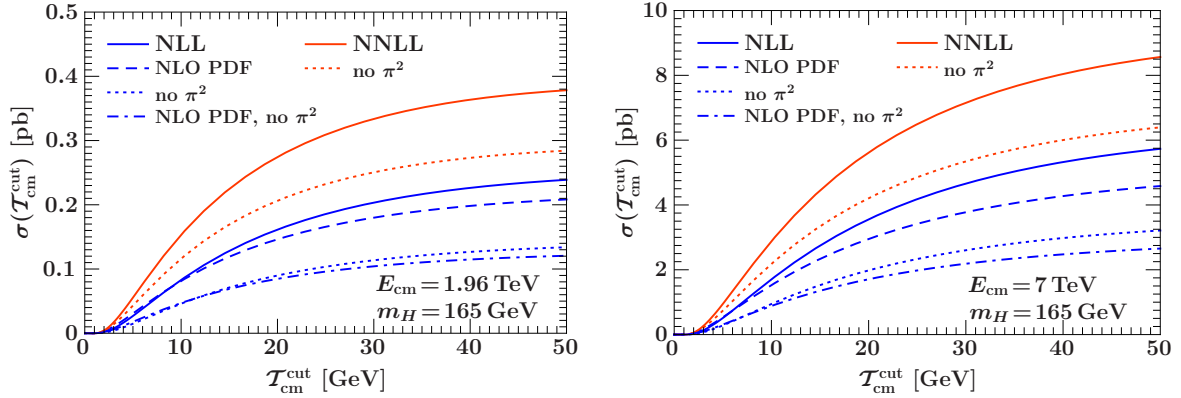


Figure 7. The effect of π^2 summation and using different orders for the PDFs on the cumulant beam thrust cross section for $m_H = 165$ GeV at the Tevatron (left panel) and the LHC with 7 TeV (right panel). Shown are the NLL result with/without π^2 summation and with LO/NLO PDFs, as well as the NNLL cross section with/without π^2 summation and NLO PDFs. See the text for further explanations.

by the large π^2 terms in the virtual hard-matching contributions. This result for the cross section with a cut on \mathcal{T}_{cm} agrees with the observations made in ref. [84] for the total cross section. Similarly, we have checked that the π^2 summation in the NNLL result brings it much closer to the total NNLO result. As a result, the convergence of the perturbative series is significantly improved by including the π^2 summation, and we will make use of this for our main results.

We can also explore the effect of using the NLO PDFs already at NLL, which amounts to including some higher-order terms in the NLL result but allows us to use the same value for $\alpha_s(m_Z)$ at NLL and NNLL. The corresponding results are shown by the blue dashed (with π^2 summation) and dot-dashed (without π^2 summation) in figure 7. For our default (solid blue curve) we use the LO PDFs in the NLL cross section, which increases it by about 10% compared to using NLO PDFs at NLL. Thus it moves the NLL result in the direction of the NNLL result. The main reason for the upward shift is the higher value of α_s associated with the lower-order PDFs, since the Higgs cross section has an overall α_s^2 .

2.8 Nonperturbative Corrections

As discussed in section 2.3, for $\mathcal{T}_{\text{cm}} \ll m_H$ the leading nonperturbative hadronization corrections to the beam thrust spectrum are given by a nonperturbative soft function F^{gg} . For $\mathcal{T}_{\text{cm}} \gg \Lambda_{\text{QCD}}$ the dominant nonperturbative effect can be described by an OPE that yields a single nonperturbative parameter $\Omega_1^{gg} \sim \Lambda_{\text{QCD}}$, leading to a shift in the beam thrust spectrum by $\mathcal{T}_{\text{cm}} \rightarrow \mathcal{T}_{\text{cm}} - 2\Omega_1^{gg}$, and in the cumulant by $\mathcal{T}_{\text{cm}}^{\text{cut}} \rightarrow \mathcal{T}_{\text{cm}}^{\text{cut}} - 2\Omega_1^{gg}$. To illustrate the size of this nonperturbative effect we consider two values for Ω_1^{gg} . First, $\Omega_1^{gg} = 0.35$ GeV is motivated by the fit result for an analogous parameter for dijet quark production in e^+e^- collisions [92]. Second, $\Omega_1^{gg} = 1.0$ GeV is motivated by a potential enhancement by $C_A/C_F = 9/4$

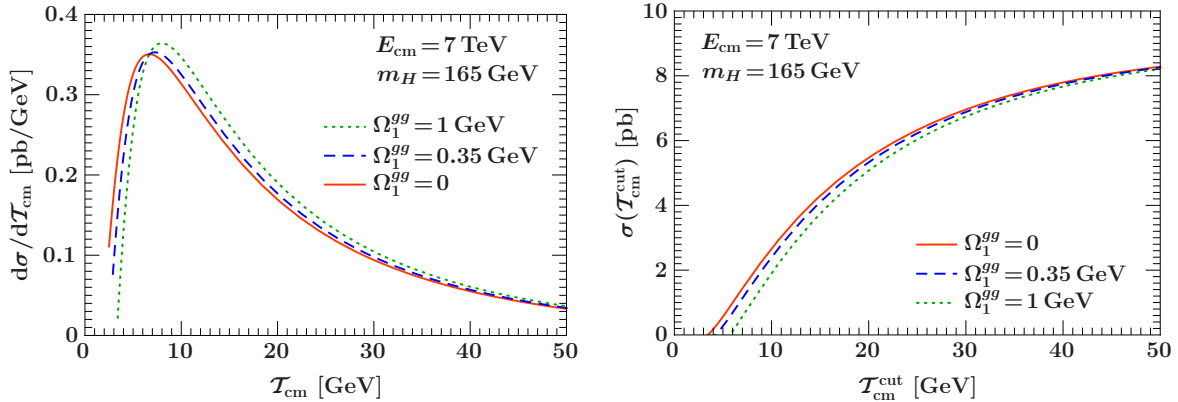


Figure 8. Shift to the NNLL+NNLO perturbative cross section, shown by solid curves with $\Omega_1^{gg} = 0$, caused by the leading nonperturbative hadronization corrections, shown by the dashed and dotted curves for $\Omega_1^{gg} = 0.35$ GeV and $\Omega_1^{gg} = 1.0$ GeV, respectively.

from Casimir scaling for adjoint Wilson lines. This choice also reproduces roughly the size of hadronization effects for Higgs production in PYTHIA. Using eqs. (2.28) and (2.29), results from the OPE for the LHC with $E_{\text{cm}} = 7$ TeV are shown in figure 8. Comparing the OPE results for the distribution, shown in the left panel, to the full convolution with a model soft function using eq. (2.26), we find that the OPE works well for the entire displayed spectrum when $\Omega_1^{gg} = 0.35$ GeV and for $\mathcal{T}_{\text{cm}} > 10$ GeV when $\Omega_1^{gg} = 1.0$ GeV. (Thus, for $\Omega_1^{gg} = 0.35$ GeV the peak is perturbative.) Examining the right panel of figure 8, we see that at $\mathcal{T}_{\text{cm}}^{\text{cut}} = 20$ GeV a power correction of $\Omega_1^{gg} = 0.35$ GeV reduces $\sigma(\mathcal{T}_{\text{cm}}^{\text{cut}})$ by 3%, while for $\Omega_1^{gg} = 1.0$ GeV the reduction is by 7%. (The results for the Tevatron are very similar, giving reductions by 2% and 6%, respectively, for $\mathcal{T}_{\text{cm}}^{\text{cut}} = 20$ GeV.) The sign of this nonperturbative shift is predicted by the factorization theorem, while its magnitude is determined by Ω_1^{gg} . Examining the \mathcal{T}_{cm} spectra from PYTHIA before and after hadronization, we find that the hadronization correction in PYTHIA is consistent with the nonperturbative shift discussed here with a value $\Omega_1^{gg} = 1.0$ GeV for both the Tevatron and LHC.

3 Numerical Results

In this section we present our numerical results for the Higgs production cross section for both the differential beam thrust spectrum, $d\sigma/d\mathcal{T}_{\text{cm}}$, and the cumulant, $\sigma(\mathcal{T}_{\text{cm}}^{\text{cut}})$, which gives the integrated cross section with a cut on beam thrust, $\mathcal{T}_{\text{cm}} \leq \mathcal{T}_{\text{cm}}^{\text{cut}}$. We are mostly interested in the region of small \mathcal{T}_{cm} or $\mathcal{T}_{\text{cm}}^{\text{cut}}$, which corresponds to the 0-jet region. We will show resummed results up to NNLL+NNLO order and also compare with the results obtained in fixed-order perturbation theory at NNLO using FEH1P [27, 43]. An explanation of the various orders is given at the beginning of section 2 and in table 1. Since our focus in this section is on the perturbative results and their uncertainties, we will not include the nonperturbative hadronic correction discussed in section 2.8 (i.e. we take $\Omega_1^{gg} = 0$).

The perturbative uncertainties in the resummed predictions are estimated as explained in detail in section 2.6. For the fixed-order results we use $\mu = m_H/2$ as the default choice for the central value, which tends to give a better convergence for the total cross section, mimicking the effect of the π^2 summation. The perturbative scale uncertainties at fixed order are then evaluated using $\mu = m_H$ and $\mu = m_H/4$. (We follow ref. [8] and do not vary the renormalization and factorization scales independently.) Since our focus here is on the perturbative uncertainties, we do not add PDF and $\alpha_s(m_Z)$ uncertainties in our plots. We have checked that they are essentially independent of the cut on beam thrust and the same as for the total inclusive cross section.

We show results for both the Tevatron and the LHC. For the LHC we always use $E_{\text{cm}} = 7$ TeV. The results for higher E_{cm} are qualitatively similar, except for the overall increased cross section. For most of our plots we use $m_H = 165$ GeV, which is near the WW threshold and where the current Tevatron limits are most sensitive. We also show some plots that illustrate the dependence of our results on m_H .

3.1 Convergence of Resummed Predictions

To study the convergence of the resummed results, we consider results at three different orders: NLL, NLL'+NLO, and NNLL+NNLO, which contain the matching and nonsingular corrections at LO, NLO, and NNLO, respectively. We choose NLL instead of LL as our lowest order to compare to, since NLL is the lowest order where we get a useful approximation with appropriately large scale uncertainties. (The LL results are lower than the NLL ones and also have a smaller scale uncertainty, which means that they do not contain enough information yet to provide a reasonable lowest-order approximation.)

In figures 9 and 10 we show the convergence for the differential spectrum and cumulant, respectively for the Tevatron (left panels) and the LHC (right panels). In figure 11 we show the cumulant for fixed $\mathcal{T}_{\text{cm}}^{\text{cut}}$ as a function of the Higgs mass. We see that the perturbative corrections are rather large, as is typical for Higgs production. The convergence within our perturbative uncertainty bands is reasonable for the differential spectrum and quite good for the cumulant, both for different $\mathcal{T}_{\text{cm}}^{\text{cut}}$ and different m_H . The large step from NLL to NLL'+NLO is mostly due to the NLO matching corrections. As we saw in figure 5, for $\mathcal{T}_{\text{cm}}^{\text{cut}} \ll m_H$ the nonsingular terms are much smaller than the singular corrections that we have computed analytically. One can also see this by comparing the size of the NLO nonsingular terms in the left panel of figure 4 with the full cross section in the right panel of figure 10.

The beam thrust spectrum in figure 9 is peaked in the 0-jet region at small beam thrust $\mathcal{T}_{\text{cm}} \simeq 5$ GeV with a large tail towards higher values. The peak in the spectrum is a perturbative prediction; hadronization effects only have a mild effect on the peak structure as shown above in section 2.8. For the beam thrust spectrum of Drell-Yan, which is Fig. 3 of ref. [94], the peak occurs at smaller values, around $\mathcal{T}_{\text{cm}} \sim 2$ GeV, and the tail of the spectrum falls off much faster. The reason for the shifted peak and higher tail for Higgs production compared to Drell-Yan is that the incoming gluons emit much more initial-state radiation than quarks. This is also the main reason why the perturbative uncertainties are still rather large even

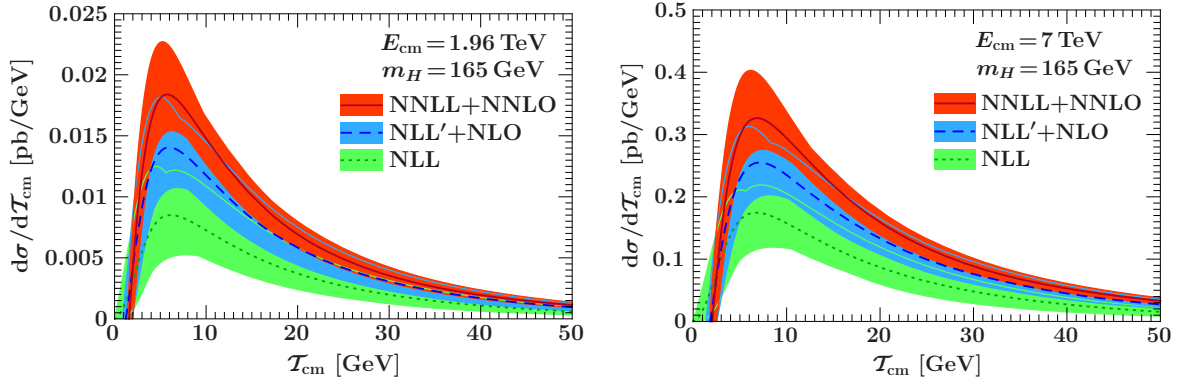


Figure 9. The beam thrust spectrum for Higgs production for $m_H = 165$ GeV at the Tevatron (left) and the LHC for $E_{\text{cm}} = 7$ TeV (right). The bands show the perturbative scale uncertainties as explained in section 2.6.

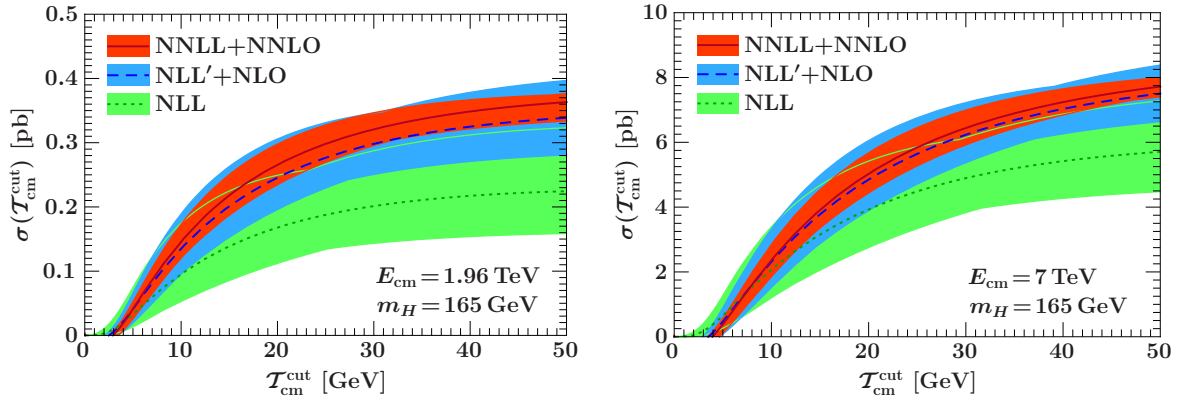


Figure 10. Higgs production cross section as a function of $\mathcal{T}_{\text{cm}}^{\text{cut}}$ for $m_H = 165$ GeV at the Tevatron (left) and the LHC with $E_{\text{cm}} = 7$ TeV (right). The bands show the perturbative scale uncertainties as explained in section 2.6.

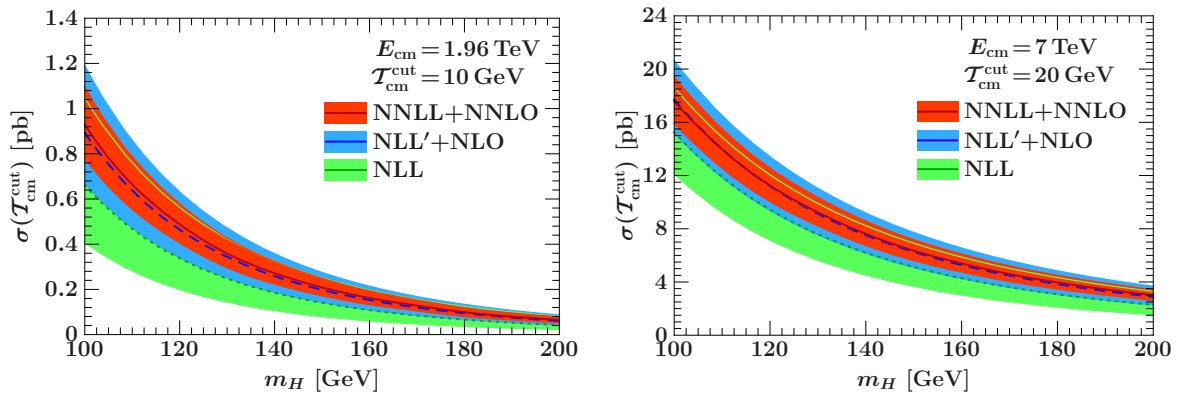


Figure 11. Higgs production cross section with a cut on beam thrust as function of m_H at the Tevatron for $\mathcal{T}_{\text{cm}}^{\text{cut}} = 10$ GeV (left) and the LHC with $E_{\text{cm}} = 7$ TeV and $\mathcal{T}_{\text{cm}}^{\text{cut}} = 20$ GeV (right). The bands show the perturbative scale uncertainties as explained in section 2.6.

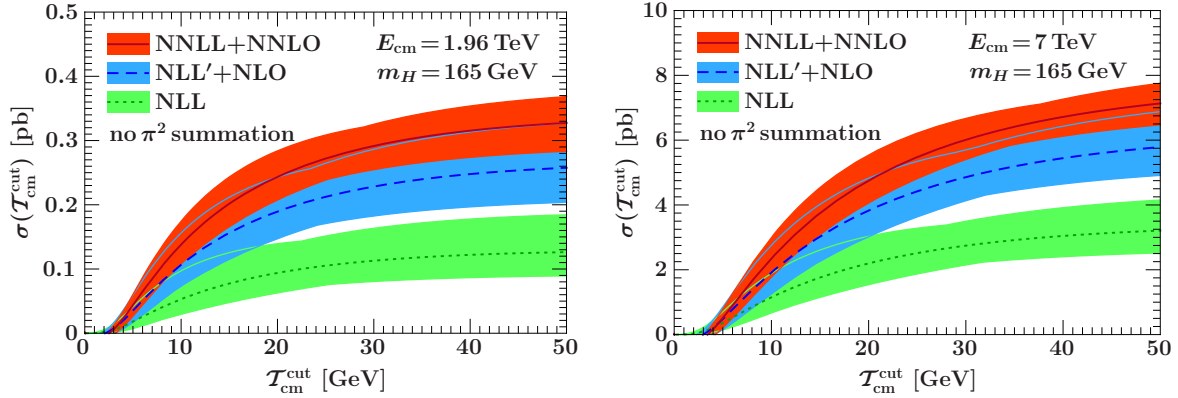


Figure 12. Same as figure 10 but without the π^2 summation.

at the highest order, NNLL+NNLO. One can also see that at the LHC the tail is somewhat higher and the peak less pronounced than at the Tevatron. Correspondingly, the cumulant at the Tevatron starts to level out earlier than at the LHC. The reason is that due to the higher center-of-mass energy at the LHC, more phase space is available for initial-state radiation.

In figure 12 we illustrate what happens if we turn off the π^2 summation. Comparing with figure 10, we see again that the π^2 summation significantly improves the convergence, and by reducing the overall size of the fixed-order corrections it also reduces the size of the perturbative uncertainties.

3.2 Comparison of Resummed and Fixed-Order Predictions

In this subsection, we compare our best resummed result at NNLL+NNLO to the NNLO fixed-order prediction without any resummation. In figure 13 we compare both predictions for the differential beam-thrust spectrum for the Tevatron (left panel) and the LHC (right panel). For small \mathcal{T}_{cm} the large logarithms of $\mathcal{T}_{\text{cm}}/m_H$ dominate the cross section. The NNLO cross section contains terms up to $\alpha_s^2 \ln^3(\mathcal{T}_{\text{cm}}/m_H)/\mathcal{T}_{\text{cm}}$ and diverges as $\mathcal{T}_{\text{cm}} \rightarrow 0$, so we do not expect it to provide a good description of the spectrum at small \mathcal{T}_{cm} . In the NNLL+NNLO calculation, the series of logarithms is summed to all orders, which regulates the divergences and yields a reliable prediction for the cross section. The resummation also enhances the radiative tail in the spectrum, because it essentially sums up the effects of multiple emissions from ISR.

In figure 14 we illustrate that the NNLL+NNLO result correctly reproduces the NNLO result for large $\mathcal{T}_{\text{cm}}^{\text{cut}}$. To see this we need to switch off the π^2 summation, because the NNLL+NNLO result would otherwise contain higher order π^2 terms at large $\mathcal{T}_{\text{cm}}^{\text{cut}}$ that are absent at fixed NNLO. Furthermore, we use $\mu = m_H$ for the NNLO central value, and $\mu = 2m_H$ and $\mu = m_H/2$ for the NNLO scale uncertainties. In this way, the NNLL+NNLO and the NNLO are evaluated at the same scales for large $\mathcal{T}_{\text{cm}} \geq 0.6 m_H$, where the logarithmic resummation is switched off and our running scales satisfy [see section 2.6] $\mu_S(\mathcal{T}_{\text{cm}}^{\text{cut}}) = \mu_B(\mathcal{T}_{\text{cm}}^{\text{cut}}) = \mu_{\text{ns}} = \mu_H = m_H$. In figure 14 we see that with these choices the NNLL+NNLO

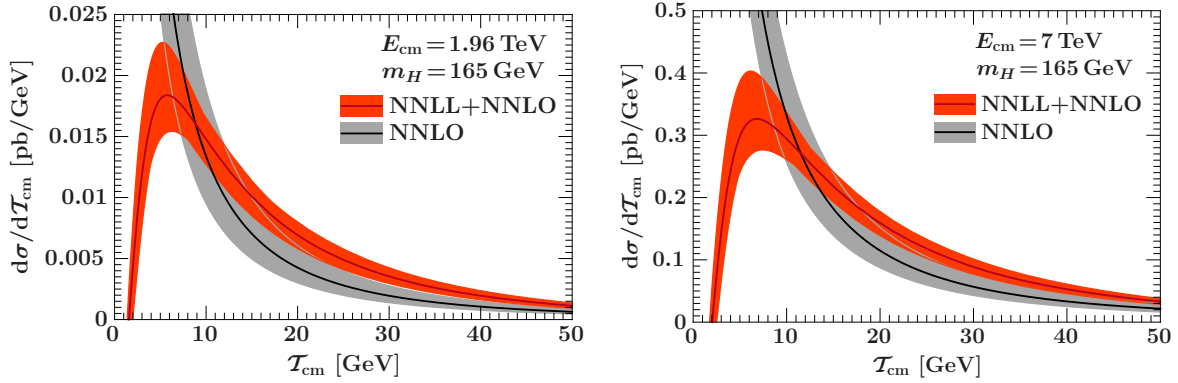


Figure 13. Comparison of the beam thrust spectrum at NNLL+NNLO to the fixed NNLO result at the Tevatron (left) and the LHC with $E_{\text{cm}} = 7 \text{ TeV}$ (right). The bands show the perturbative scale uncertainties.

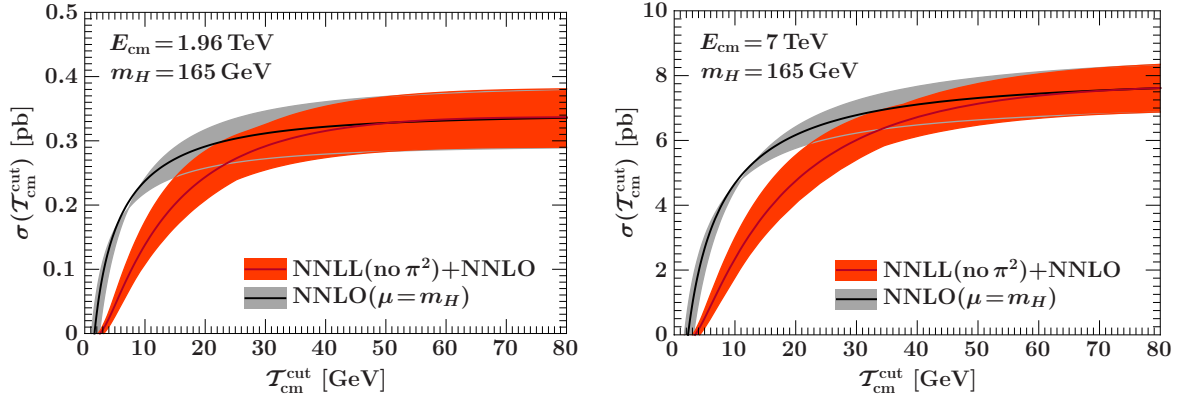


Figure 14. Illustration that the NNLL+NNLO resummed result reproduces the fixed NNLO result at large beam thrust for the Tevatron (left) and the LHC (right). The resummed result has the π^2 summation switched off and $\mu = m_H$ is used for the central value of the fixed-order result. The bands show the perturbative uncertainties. See text for further explanations.

indeed smoothly merges into the NNLO result, including the scale uncertainties, at large $\mathcal{T}_{\text{cm}}^{\text{cut}}$, as it should. Examining figure 14 for smaller $\mathcal{T}_{\text{cm}}^{\text{cut}}$ values we see that the resummed result starts to deviate from the fixed-order one for $\mathcal{T}_{\text{cm}}^{\text{cut}} \lesssim 40 \text{ GeV}$ at the Tevatron and $\mathcal{T}_{\text{cm}}^{\text{cut}} \lesssim 50 \text{ GeV}$ at the LHC.

In figures 15 and 16 we compare the full NNLL+NNLO including π^2 summation to the NNLO (using again the default $\mu = m_H/2$ as the central value) for the Tevatron and LHC, respectively. The left panels show the cumulant cross section, and the right panels show the same results as the relative difference in percent to the central NNLL+NNLO curve, which makes it easy to read off uncertainties. The relative plots are cut off below $\mathcal{T}_{\text{cm}}^{\text{cut}} = 5 \text{ GeV}$ because the resummed cross section goes to zero there. The central value of the NNLL+NNLO leaves the fixed-order uncertainty band at $\mathcal{T}_{\text{cm}}^{\text{cut}} \simeq 25 \text{ GeV}$ at the Tevatron

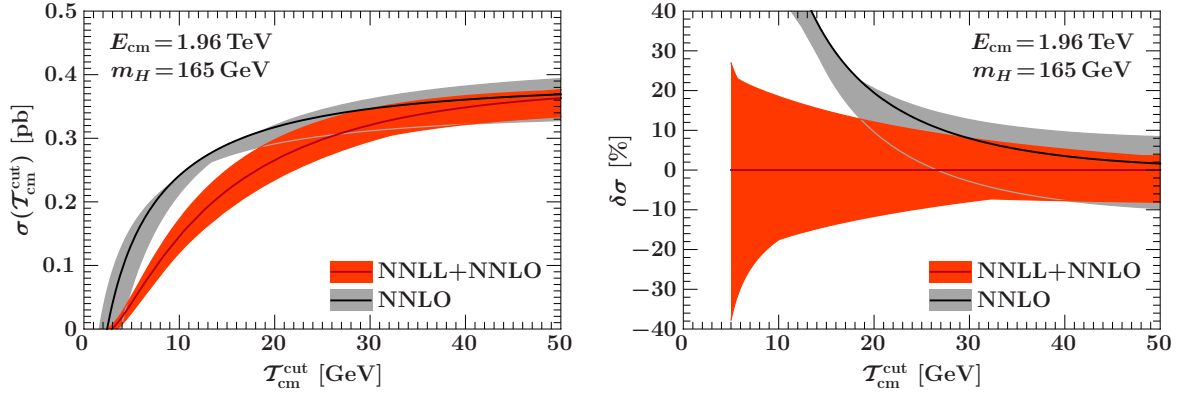


Figure 15. Comparison of the NNLL+NNLO result for the Higgs production cross section as a function of $\mathcal{T}_{\text{cm}}^{\text{cut}}$ to the fixed NNLO result for the Tevatron. The bands show the perturbative scale uncertainties. The left plot shows the cumulant cross section. The right plot shows the same information as percent difference relative to the NNLL+NNLO central value.

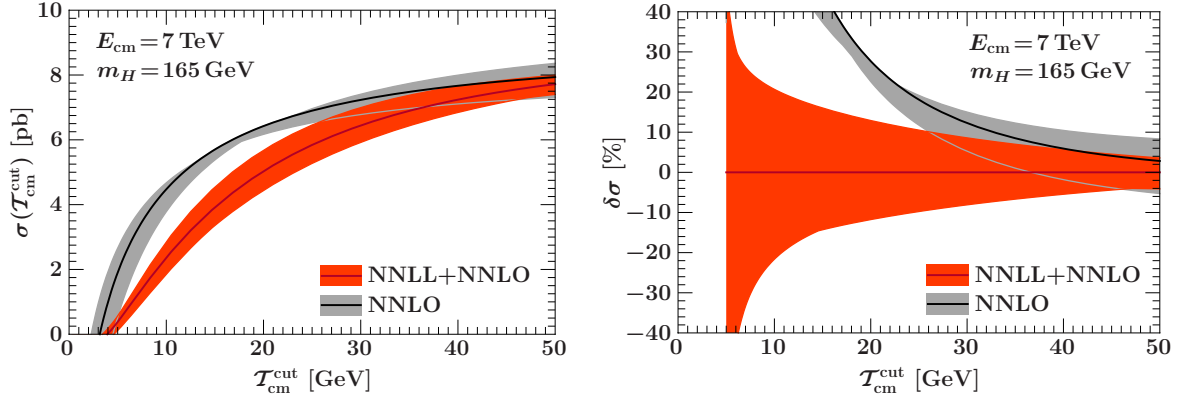


Figure 16. Same as figure 15 but for the LHC with $E_{\text{cm}} = 7 \text{ TeV}$.

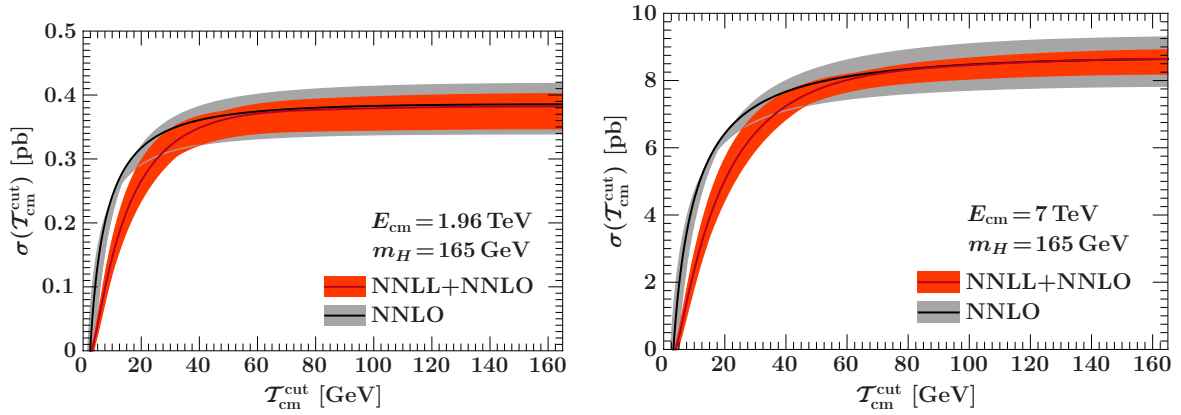


Figure 17. Same as the left panels of figures 15 and 16 but plotted up to $\mathcal{T}_{\text{cm}}^{\text{cut}} = m_H$.

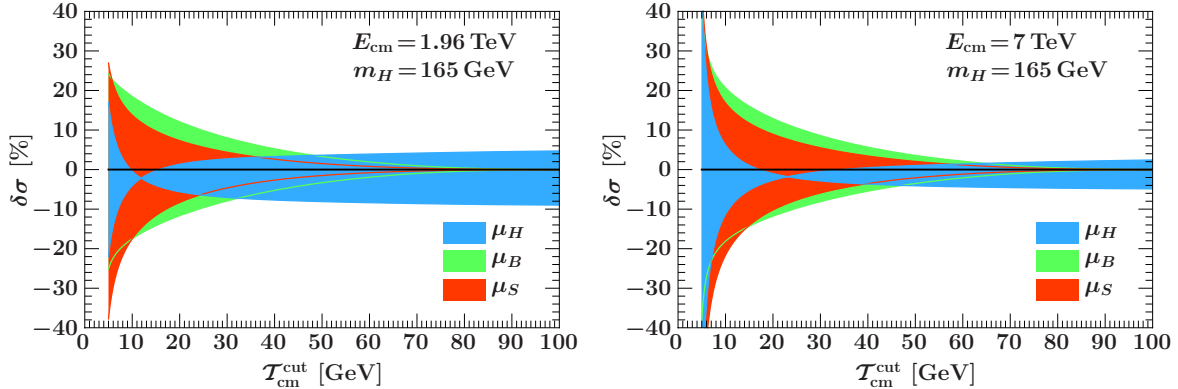


Figure 18. Contribution to the relative uncertainties in the NNLL+NNLO results shown in figures 15 and 16 from the individual scale variations. Here, the μ_H , μ_B , and μ_S variations correspond to cases a), b), and c) in eq. (2.55) and are shown in figure 6.

and at $\mathcal{T}_{\text{cm}}^{\text{cut}} \simeq 35 \text{ GeV}$ at the LHC. Hence, for any lower values the resummation should be taken into account. At $\mathcal{T}_{\text{cm}}^{\text{cut}} = 20 \text{ GeV}$ the central values of the NNLL+NNLO and the NNLO already differ by 20% at the Tevatron and over 25% at the LHC, which both quickly grows beyond 50% towards $\mathcal{T}_{\text{cm}}^{\text{cut}} = 10 \text{ GeV}$.⁷ This clearly shows that it is important to resum the higher-order logarithms that are missing in the fixed-order prediction in order to obtain reliable predictions in the 0-jet region. This also means that one cannot expect the scale variation in the fixed-order result to give a realistic estimate of the size of the missing higher-order terms, and hence it should not be used to estimate the perturbative scale uncertainty either. In contrast, since the resummation takes into account the presence of large logarithms for small $\mathcal{T}_{\text{cm}}^{\text{cut}}$, we are able to obtain reliable estimates of the perturbative uncertainties. The perturbative uncertainties at small $\mathcal{T}_{\text{cm}}^{\text{cut}}$ are larger than those in the fixed-order result, namely 15 – 20% at NNLL+NNLO for $\mathcal{T}_{\text{cm}}^{\text{cut}} = 15 – 20 \text{ GeV}$. Implications of this for the Higgs search are taken up in section 4.

In figure 17 we show the same comparison of NNLL+NNLO and NNLO cumulants, but plotted up to $\mathcal{T}_{\text{cm}}^{\text{cut}} = m_H$. We can see that the central value of the resummed result including the π^2 resummation almost exactly reproduces the NNLO result which uses $\mu = m_H/2$. However, the π^2 summation included in the NNLL+NNLO results leads to a reduction of the scale uncertainties in the inclusive cross section compared to those at NNLO. For the uncertainties at the LHC we find +3% and –5% and for the Tevatron +5% and –9%. In figure 18 we show the relative uncertainties at NNLL+NNLO from the individual scale variations in eq. (2.55). We can see that at small $\mathcal{T}_{\text{cm}}^{\text{cut}}$ the uncertainties are dominated by μ_B and μ_S , i.e. variations b) and c) in eq. (2.55). By construction, those variations go to zero at large $\mathcal{T}_{\text{cm}}^{\text{cut}}$, where the uncertainties are now completely determined by variation a) in

⁷One might expect that a better agreement could be achieved by using a dynamical $\mathcal{T}_{\text{cm}}^{\text{cut}}$ -dependent scale in the fixed-order prediction. We have checked that using the intermediate scale $\mu = \mu_B$ in the fixed-order result however does not improve its behavior relative to the resummed result, but in fact makes it a bit worse.

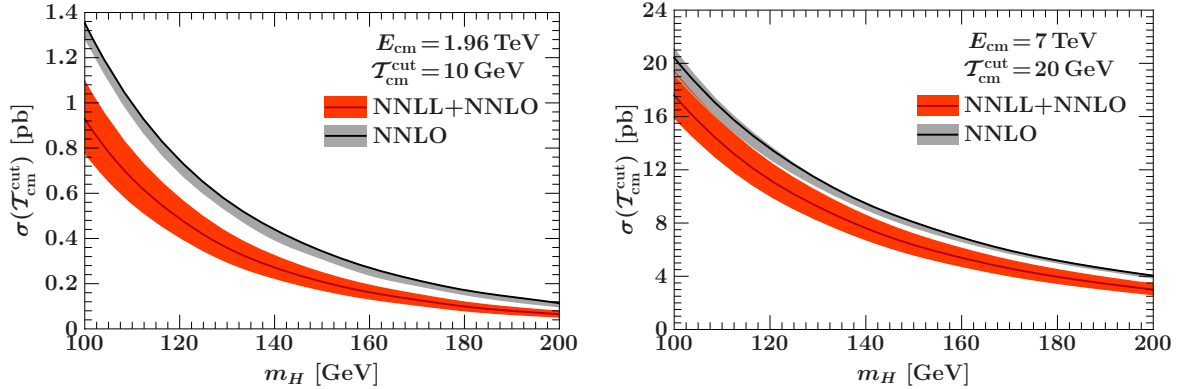


Figure 19. Comparison of the NNLL+NNLO result to the fixed NNLO result for the Higgs production cross section with a cut on beam thrust as function of m_H at the Tevatron for $\mathcal{T}_{\text{cm}}^{\text{cut}} = 10$ GeV (left) and the LHC with $E_{\text{cm}} = 7$ TeV and $\mathcal{T}_{\text{cm}}^{\text{cut}} = 20$ GeV (right). The bands show the perturbative scale uncertainties.

eq. (2.55) and denoted μ_H in the figure, which is equivalent to the fixed-order scale variation.

Finally, figure 19 shows a comparison of NNLL+NNLO to NNLO as a function of the Higgs mass for a fixed value of $\mathcal{T}_{\text{cm}}^{\text{cut}}$. For smaller Higgs masses, the logarithms get smaller and the cross section increases, which reduces the relative differences. This does not change however our overall conclusions for the importance of the resummation for both the central value and determining the perturbative uncertainties.

3.3 Discussion of K -Factors

Using our results we can also address the origin of the large NLO and NNLO K -factors that are typically observed for Higgs production. It is sometimes argued that the origin of these large K -factors for the inclusive cross section are large perturbative corrections due to hard emissions. This is based on the observation that by vetoing hard jets, the fixed-order K -factors are reduced. As a result the fixed-order perturbative series in the presence of a jet veto actually appears to be better behaved than for the inclusive cross section.

Our results show that once the large jet-veto logarithms are properly summed, the K -factor is mostly independent of the jet veto. Hence, it is not caused by hard real emissions, but rather mostly by hard virtual corrections and to a lesser extent by collinear and soft virtual and real radiation. In our analysis this can be examined directly by comparing the convergence of perturbation theory for the hard, jet, and soft functions. As we have seen in section 2.7, and was already observed in ref. [84], by summing the large π^2 terms in the hard virtual corrections, the K -factors are substantially reduced.

There is a simple reason why the large K -factors in fixed-order perturbation theory are reduced: At NLO, the jet veto reduces the cross section just because it cuts out available phase space, and since at LO the cross section is not yet affected by the jet veto, the NLO K -factor is reduced accordingly. Essentially, the large negative phase-space logarithms resulting

from the jet veto happen to cancel the large positive corrections from hard virtual corrections. A similar effect appears at NNLO where the jet veto reduces the available phase space for the second jet. Since the hard virtual corrections are independent of the jet veto one can always choose a particular value for the jet-veto cut such that they are exactly canceled by the large phase-space logarithms at a given order in perturbation theory. However, to conclude that the jet veto in general renders the fixed-order perturbative series better behaved one would have to know that the same level of cancellation will happen at each order in perturbation theory. Since these two types of corrections are a priori not related there is no reason to believe this will be the case. Instead, to obtain reliable predictions both types of large corrections should be rendered as convergent as possible. For the hard virtual corrections the π^2 summation improves the convergence, and for the large phase-space logarithms this is achieved by the resummation carried out here. With the resulting cross section we can then obtain more realistic estimates for higher-order theoretical uncertainties as discussed in section 3.2.

4 Conclusions

A major effort at the LHC and Tevatron is devoted to the search for the Higgs boson. In the current Tevatron exclusion limits and the early LHC searches the $H \rightarrow WW \rightarrow \ell^+ \nu \ell^- \bar{\nu}$ channel plays an important role, since it is the dominant decay channel for Higgs masses above ~ 130 GeV. A large background for this channel are $t\bar{t} \rightarrow WWb\bar{b}$ events, which must be eliminated by a veto on central jets, so the resulting measurement is $pp \rightarrow H + 0$ jets. Such a jet veto causes large double logarithms in the cross section, which need to be summed to all orders in perturbation theory in order to obtain reliable theoretical predictions and uncertainties for the $H + 0$ jet production cross section.

In this paper we have studied Higgs production from gluon fusion, using the inclusive event shape beam thrust, \mathcal{T}_{cm} , to implement a central jet veto. As beam thrust characterizes the event as a whole and does not require a jet algorithm, it is well suited to analytic calculations. This allows us to resum the jet-veto logarithms to NNLL order, based on the factorization theorem for the beam thrust cross section derived in ref. [56]. In our analysis we also include the full set of NNLO corrections, such that our final result at NNLL+NNLO provides the best possible theoretical prediction at any value of beam thrust.

Our main results are presented in figs. 15 and 16. We find that in the 0-jet region at small beam thrust, the resummation of jet-veto logarithms is crucial, and our central value at NNLL+NNLO for the cross section with a cut on beam thrust, $\mathcal{T}_{\text{cm}} \leq \mathcal{T}_{\text{cm}}^{\text{cut}}$, differs significantly from the fixed-order prediction at NNLO. We also find substantially larger perturbative scale uncertainties arising from the jet veto compared to those at NNLO. Since fixed-order perturbation theory is not reliable in the presence of large jet-veto logarithms, one also cannot expect its scale variation to yield a reliable estimate of perturbative uncertainties due to neglecting higher-order corrections.

At present, the jet-veto logarithms are taken into account in the experimental analyses using the leading-logarithmic resummation provided by parton-shower Monte Carlo programs,

usually supplemented with some reweighting procedure to reproduce the total NNLO cross section. While this might yield a reasonable central value that takes into account the dominant effect of the logarithmic resummation, the uncertainties in the so predicted 0-jet cross section cannot be taken as those of the inclusive NNLO cross section. They could at best be equal to those in our NNLL+NNLO results. In fact, they are probably larger than that, since we include the resummation at two orders higher than the LL resummation of parton showers. As we have seen in section 3.1, already one order lower, at NLL'+NLO, the perturbative uncertainties are much larger than those in our NNLL+NNLO results.

The conventional method to veto central jets is to use a jet algorithm and require $p_T^{\text{jet}} < p_T^{\text{cut}}$ for all jets in the event. As we saw in section 1, p_T^{cut} can be related to $\mathcal{T}_{\text{cm}}^{\text{cut}}$ by associating $\mathcal{T}_{\text{cm}}^{\text{cut}}/m_H \simeq (p_T^{\text{cut}}/m_H)^{\sqrt{2}}$ or $\mathcal{T}_{\text{cm}}^{\text{cut}} = p_T^{\text{cut}}$, where the former works well at NNLO while the latter is favored by PYTHIA 8. Hence, we can use the perturbative uncertainties in our results based on $\mathcal{T}_{\text{cm}}^{\text{cut}}$ as a benchmark for the perturbative uncertainties from large logarithms relevant for p_T^{cut} , on which the current experimental analyses are based. For example, the perturbative uncertainties for typical values $p_T^{\text{cut}} \simeq 20 - 30$ GeV at the LHC can be as large as those for $\mathcal{T}_{\text{cm}}^{\text{cut}} \simeq 10 - 15$ GeV, which are 15 - 20% at NNLL+NNLO (for $m_H = 165$ GeV and $E_{\text{cm}} = 7$ TeV). In the current Tevatron analyses, the perturbative scale uncertainty in the 0-jet cross section for $p_T^{\text{cut}} = 15$ GeV is taken as 7% from the fixed-order analysis in ref. [8]. In contrast, the perturbative uncertainties at NNLL+NNLO for values $\mathcal{T}_{\text{cm}}^{\text{cut}} \leq 15$ GeV are significantly larger, e.g. about 20% for $\mathcal{T}_{\text{cm}}^{\text{cut}} = 10$ GeV and $m_H = 165$ GeV. In light of this, the current Tevatron exclusion limits should be reconsidered with an increased theory uncertainty for the 0-jet Higgs cross section. We note that our conclusions about theoretical uncertainties are based on a systematic study of the jet veto, and are therefore independent of the arguments in ref. [9] proposing the use of a larger range for the fixed-order scale variation.

To implement our NNLL+NNLO results in the experimental searches, one could reweight the partonic beam-thrust spectrum obtained from Monte Carlo to our results. This would incorporate both the higher-order resummation of large logarithms in the 0-jet region and at the same time the full NNLO result for the total cross section. This also allows a consistent treatment of the perturbative uncertainties in both regions. To illustrate this, consider dividing the total inclusive cross section, σ_{total} , into a 0-jet bin, $\sigma_0 \equiv \sigma(\mathcal{T}_{\text{cm}}^{\text{cut}})$, and a remaining (≥ 1)-jet bin, $\sigma_{\geq 1} \equiv \sigma_{\text{total}} - \sigma(\mathcal{T}_{\text{cm}}^{\text{cut}})$. This separation into exclusive jet bins causes large logarithms of $\mathcal{T}_{\text{cm}}^{\text{cut}}$ in both σ_0 and $\sigma_{\geq 1}$ which cancel in their sum. This implies that the uncertainties due to $\mathcal{T}_{\text{cm}}^{\text{cut}}$ in both bins are anti-correlated. In particular, if one wants to consider the theory uncertainties in σ_0 and $\sigma_{\geq 1}$ simultaneously in a Gaussian fashion, one has to consider the full theory covariance matrix

$$C = \begin{pmatrix} \Delta_0^2 & \Delta_0 \Delta_{\geq 1} \rho_{0,\geq 1} \\ \Delta_0 \Delta_{\geq 1} \rho_{0,\geq 1} & \Delta_{\geq 1}^2 \end{pmatrix} \approx \begin{pmatrix} \Delta_0^2 & -\Delta_0^2 \\ -\Delta_0^2 & \Delta_0^2 + \Delta_{\text{total}}^2 \end{pmatrix}, \quad (4.1)$$

where Δ_0 and $\Delta_{\geq 1}$ are the theory uncertainties of σ_0 and $\sigma_{\geq 1}$, and $\rho_{0,\geq 1}$ is their correlation coefficient. In the second step above we used the approximation that the uncertainties in σ_0 and σ_{total} are uncorrelated and are added in quadrature in $\sigma_{\geq 1}$. From our results in figure 18

we can see that this is reasonable since the uncertainties in σ_0 are dominated by the lower scales μ_B and μ_S , while those in σ_{total} are determined by μ_H (which in this case is combined in quadrature with the others rather than by taking the envelope). The uncertainty squared for the total cross section, $\sigma_0 + \sigma_{\geq 1}$, is given by the sum of all entries in the matrix C in eq. (4.1). Due to the anti-correlation the uncertainties for the individual jet bins can be larger than that for the total cross section. Our numerical results for the theory uncertainties for the 0-jet bin directly give Δ_0 . The full correlation can be taken into account by reweighting the Monte Carlo to both the central value curve as well as the results obtained from the individual scale variations.

It would also be useful to have a benchmark theoretical uncertainty that is desired for the experimental searches, since with further effort our NNLL+NNLO results can be extended to NNLL'+NNLO or N³LL+NNLO, which has the potential to reduce the uncertainty in the resummed perturbation theory. Given that the theoretical predictions and their uncertainties are very sensitive to the jet veto, it would also be useful to implement the jet veto in the experimental analyses directly in terms of beam thrust, for which resummed theory predictions are available. In addition, a benchmark experimental study of the beam-thrust spectrum can be made with Drell-Yan pairs, as advocated in ref. [94].

In this paper, we have restricted ourselves to studying the case of $gg \rightarrow H + 0$ jets. The same methods can be used to calculate the dominant irreducible background from direct WW production, i.e., the process $pp \rightarrow WW + 0$ jets using beam thrust for the jet veto. The generalization of beam thrust to processes with N signal jets is provided by the event shape N -jettiness introduced in ref. [63]. It can be used in an analogous fashion to study the exclusive $H + 1$ jet and $H + 2$ jet cross sections, the latter being relevant for Higgs production from vector-boson fusion.

Acknowledgments

We thank the ATLAS group at the University of Pennsylvania and Elliot Lipeles for stimulating discussions. We also thank Lance Dixon, Steve Ellis, Zoltan Ligeti, Aneesh Manohar, Kerstin Tackmann, Jesse Thaler, Joey Huston, Fabian Stöckli and especially Kirill Melnikov and Frank Petriello for useful discussions and comments on the manuscript. For hospitality during part of this work we thank the Max-Planck Institute for Physics (Werner-Heisenberg Institute), the CERN theory group, and the Center for the Fundamental Laws of Nature at Harvard. This work was supported in part by the Office of Nuclear Physics of the U.S. Department of Energy under the Contract DE-FG02-94ER40818, by the Department of Energy under the grant DE-SC003916, and by a Friedrich Wilhelm Bessel award from the Alexander von Humboldt foundation.

A NLO Calculation of the Gluon Beam Function

In this section we compute the NLO gluon beam function. We first recall its definition, renormalization, and operator product expansion in terms of standard PDFs and Wilson coefficients \mathcal{I}_{ij} , as discussed in detail in ref. [68]. For a discussion of the basic SCET ingredients relevant to our context we refer to refs. [56, 68]. We then give the details of the one-loop matching calculation, which provides a check on the one-loop anomalous dimension of the gluon beam function and yields the \mathcal{I}_{ij} at NLO.

A.1 Definition and General Results

As usual, we use lightlike vectors $n^\mu = (1, \vec{n})$ and $\bar{n}^\mu = (1, -\vec{n})$, satisfying $n^2 = \bar{n}^2 = 0$, $n \cdot \bar{n} = 2$, to write a vector p^μ in light-cone coordinates

$$p^\mu = p^+ \frac{\bar{n}^\mu}{2} + p^- \frac{n^\mu}{2} + p_\perp^\mu \quad \text{with} \quad p^+ = n \cdot p, \quad p^- = \bar{n} \cdot p. \quad (\text{A.1})$$

The bare gluon beam function operator is defined as

$$\begin{aligned} \mathcal{O}_g^{\text{bare}}(\omega b^+, \omega) &= -\theta(\omega) \int \frac{dy^-}{4\pi} e^{ib^+ y^- / 2} e^{-i\hat{p}^+ y^- / 2} \mathcal{B}_{n_\perp \mu}^c \left(y^- \frac{n}{2} \right) [\delta(\omega - \bar{\mathcal{P}}_n) \mathcal{B}_{n_\perp}^{\mu c}(0)] \\ &= -\omega \theta(\omega) \mathcal{B}_{n_\perp \mu}^c(0) \delta(\omega b^+ - \omega \hat{p}^+) [\delta(\omega - \bar{\mathcal{P}}_n) \mathcal{B}_{n_\perp}^{\mu c}(0)]. \end{aligned} \quad (\text{A.2})$$

The SCET gluon field $\mathcal{B}_{n_\perp}^\mu$ describes n -collinear gluons and includes zero-bin subtractions [95]. It contains collinear Wilson lines W_n to render it invariant under collinear gauge transformations. It is the field after the BPS field redefinition [73] to decouple soft gluons and is thus invariant under soft gauge transformations. Hence, $\mathcal{O}_g^{\text{bare}}$ is fully gauge invariant. The gluon beam function is defined by the proton matrix element of the corresponding renormalized operator $\mathcal{O}_g(t, \omega, \mu)$,

$$B_g(t, x = \omega/P^-, \mu) = \langle p_n(P^-) | \mathcal{O}_g(t, \omega, \mu) | p_n(P^-) \rangle. \quad (\text{A.3})$$

The proton states $|p_n(P^-)\rangle$ have lightlike momentum $P^\mu = P^- n^\mu / 2$, i.e. \vec{n} is chosen in the direction of the proton, and the matrix elements are always implicitly averaged over the proton spin.

In eq. (A.2), \hat{p}^+ is the momentum operator of the residual plus momentum and acts on everything to its right. The additional phase in the position-space operator is included to allow us to write the b^+ dependence in terms of $\delta(\omega b^+ - \omega \hat{p}^+)$, as in the second line of eq. (A.2). Hence, b^+ measures the total plus momentum of real initial-state radiation, i.e. of any intermediate state inserted between the fields. The label operator $\delta(\omega - \bar{\mathcal{P}}_n)$ in eq. (A.2) only acts inside the square brackets and forces the total sum of the minus labels of all fields in \mathcal{B}_{n_\perp} to be equal to ω . In eq. (A.3) it sets the fraction of the proton's light-cone momentum carried into the hard collision to $x = \omega/P^- > 0$. At the time of the collision, the annihilated collinear gluon propagates in a jet of initial-state radiation, and by momentum conservation the small plus momentum of the gluon is $-b^+ < 0$. Hence, it is

spacelike and $-t = \omega(-b^+) < 0$ measures its transverse virtuality. The operator $\mathcal{O}_g(t, \omega)$ is RPI-III invariant, because the transformation of the overall ω compensates that of $\delta(\omega - \overline{\mathcal{P}}_n)$. Therefore, the gluon beam function only depends on the RPI-III invariant variables x and t .

The RGE of the beam function follows from the renormalization of $\mathcal{O}_g(t, \omega, \mu)$. To all orders in perturbation theory, it takes the form

$$\mu \frac{d}{d\mu} B_g(t, x, \mu) = \int dt' \gamma_B^g(t - t', \mu) B_g(t', x, \mu), \quad (\text{A.4})$$

with the anomalous dimension

$$\gamma_B^g(t, \mu) = -2\Gamma_{\text{cusp}}^g[\alpha_s(\mu)] \frac{1}{\mu^2} \mathcal{L}_0\left(\frac{t}{\mu^2}\right) + \gamma_B^g[\alpha_s(\mu)] \delta(t). \quad (\text{A.5})$$

Here, $\mathcal{L}_0(x) = [\theta(x)/x]_+$ is defined in eq. (A.44), $\Gamma_{\text{cusp}}^g(\alpha_s)$ is the gluon cusp anomalous dimension, and $\gamma_B^g(\alpha_s)$ denotes the non-cusp part, whose coefficients up to three loops are given in appendix B. The RGE of the beam function is identical to that of the jet function. It sums double logarithms of t/μ^2 and unlike the PDF evolution does not change the x dependence and does not mix different parton types. The solution of eq. (A.4) was already given in eq. (2.17).

The standard PDFs are defined in SCET by the matrix elements [74]

$$f_i(\xi = \omega'/P^-, \mu) = \langle p_n(P^-) | \mathcal{Q}_i(\omega', \mu) | p_n(P^-) \rangle, \quad (\text{A.6})$$

where $\mathcal{Q}_i(\omega', \mu)$ are the $\overline{\text{MS}}$ renormalized operators corresponding to the bare operators

$$\begin{aligned} \mathcal{Q}_g^{\text{bare}}(\omega') &= -\omega' \theta(\omega') \mathcal{B}_{n\perp\mu}^c(0) [\delta(\omega' - \overline{\mathcal{P}}_n) \mathcal{B}_{n\perp}^{\mu c}(0)], \\ \mathcal{Q}_q^{\text{bare}}(\omega') &= \theta(\omega') \bar{\chi}_n(0) \frac{\overline{\not{n}}}{2} [\delta(\omega' - \overline{\mathcal{P}}_n) \chi_n(0)], \\ \mathcal{Q}_{\bar{q}}^{\text{bare}}(\omega') &= \theta(\omega') \text{tr} \left\{ \frac{\overline{\not{n}}}{2} \chi_n(0) [\delta(\omega' - \overline{\mathcal{P}}_n) \bar{\chi}_n(0)] \right\}. \end{aligned} \quad (\text{A.7})$$

The $\theta(\omega')$ here separates the quark and antiquark PDFs and is included to keep analogous definitions for the PDFs and beam functions.

Compared to eq. (A.7), the fields in the beam-function operator in eq. (A.2) are separated along the n light-cone with large separation y^- corresponding to the small momentum $b^+ \ll \omega$. Hence, by performing an operator product expansion about the limit $y^- \rightarrow 0$ we can expand the beam-function operator $\mathcal{O}_g(t, \omega, \mu)$ in terms of a sum over $\mathcal{Q}_i(\omega', \mu)$,

$$\mathcal{O}_g(t, \omega, \mu) = \sum_j \int \frac{d\omega'}{\omega'} \mathcal{I}_{gj}\left(t, \frac{\omega}{\omega'}, \mu\right) \mathcal{Q}_j(\omega', \mu) + \mathcal{O}\left(\frac{y^-}{\omega}\right), \quad (\text{A.8})$$

where the functional form of the matching coefficients $\mathcal{I}_{ij}(t, z, \mu)$ is again determined by RPI-III invariance. The proton matrix element of eq. (A.8) yields the OPE for the gluon beam function quoted in eq. (1.6),

$$B_g(t, x, \mu) = \sum_j \int \frac{d\xi}{\xi} \mathcal{I}_{gj}\left(t, \frac{x}{\xi}, \mu\right) f_j(\xi, \mu) \left[1 + \mathcal{O}\left(\frac{\Lambda_{\text{QCD}}^2}{t}\right) \right]. \quad (\text{A.9})$$

The power corrections scale like $(\Lambda_{\text{QCD}}^2/\omega)/b^+$, where $t = \omega b^+$ and $\Lambda_{\text{QCD}}^2/\omega$ is the typical plus momentum of the partons in the proton, and involve higher-twist proton structure functions. For $t \sim \Lambda_{\text{QCD}}^2$ the OPE would require an infinite set of higher-twist proton structure functions, which means the beam functions essentially become nonperturbative b^+ -dependent PDFs. On the other hand, for $t \gg \Lambda_{\text{QCD}}^2$, we can compute the matching coefficients \mathcal{I}_{ij} in eq. (A.9) in perturbation theory at the beam scale $\mu_B^2 \simeq t$.

The matching calculation is carried out as usual by taking partonic quark and gluon matrix elements of the operators on both sides of eq. (A.8), which we denote as

$$\begin{aligned} B_{g/j}(t, z = \omega/p^-, \mu) &= \langle j_n(p^-) | \mathcal{O}_g(t, \omega, \mu) | j_n(p^-) \rangle, \\ f_{i/j}(z = \omega/p^-, \mu) &= \langle j_n(p^-) | \mathcal{Q}_i(\omega, \mu) | j_n(p^-) \rangle, \end{aligned} \quad (\text{A.10})$$

and analogously for the bare quantities. Here, $|j_n(p^-)\rangle$ is an n -collinear gluon or quark state, $|g_n(p^-)\rangle$ or $|q_n(p^-)\rangle$, with momentum $p^\mu = p^- n^\mu/2$ and $p^- > 0$, and we average the matrix elements over both color and spin. We denote the partonic momentum fractions by $z = \omega/p^-$ to distinguish them from the hadronic x and ξ . The operators are normalized such that at tree level we simply have

$$B_{g/j}^{(0)}(t, z, \mu) = \delta_{gj} \delta(t) \delta(1-z), \quad f_{i/j}^{(0)}(z, \mu) = \delta_{ij} \delta(1-z), \quad (\text{A.11})$$

which yields

$$\mathcal{I}_{gj}^{(0)}(t, z, \mu) = \delta_{gj} \delta(t) \delta(1-z), \quad B_g^{(0)}(t, x, \mu) = \delta(t) f_g(x, \mu). \quad (\text{A.12})$$

Beyond tree level x and ξ will be different, because the momentum fraction ξ provided by the PDFs is modified by the collinear radiation encoded in the $\mathcal{I}_{gj}(t, z, \mu)$.

Expanding eq. (A.8) to NLO and using the above tree-level results we find

$$\begin{aligned} B_{g/g}^{(1)}(t, z, \mu) &= \mathcal{I}_{gg}^{(1)}(t, z, \mu) + \delta(t) f_{g/g}^{(1)}(z, \mu), \\ B_{g/q}^{(1)}(t, z, \mu) &= \mathcal{I}_{gq}^{(1)}(t, z, \mu) + \delta(t) f_{g/q}^{(1)}(z, \mu). \end{aligned} \quad (\text{A.13})$$

Hence, to compute the one-loop coefficients $\mathcal{I}_{gj}^{(1)}(t, z, \mu)$ we have to compute the one-loop gluon and quark matrix elements of the gluon operators $\mathcal{O}_g(t, \omega, \mu)$ and $\mathcal{Q}_g(\omega, \mu)$. (The quark and antiquark coefficients are identical, $\mathcal{I}_{gq} = \mathcal{I}_{g\bar{q}}$, so we do not need to consider separate matrix elements with external antiquarks.) The corresponding one-loop calculation for the quark operators to determine the matching coefficients \mathcal{I}_{qj} for the quark beam function is given in detail in ref. [68]. There, the calculation is performed in two different ways, first using different regulators for IR and UV, and second using dimensional regularization for both IR and UV. In the first case, the UV and IR divergences can be separated allowing one to obtain the UV renormalization of the operators and at the same time check that the IR divergences in the beam function match those in the PDFs, so the matching coefficients are IR finite. In the second case, the calculation is much quicker, because most diagrams are scaleless and vanish,

but it does not allow one to distinguish the IR and UV divergences. This means one can only check that the IR divergences cancel in the matching if the renormalization of both beam function and PDF are already known. Alternatively, one can assume that the IR divergences cancel and use the known renormalization of the PDFs to obtain the renormalization of the beam function. In our case, the renormalization of the gluon beam function is already known from the general analysis of ref. [68], so we only perform the second, simpler, calculation, regulating both UV and IR in dimensional regularization using the $\overline{\text{MS}}$ scheme.

A.2 The Gluon PDF at One Loop

As explained in ref. [68], the definition in eq. (A.6) is equivalent to the standard definition of the PDFs in QCD. In particular, the collinear fields in eq. (A.7) do not require zero-bin subtractions, because the soft region does not contribute to the PDFs. Therefore, we can use the standard $\overline{\text{MS}}$ renormalization of the PDFs,

$$f_i^{\text{bare}}(\xi) = \sum_j \int \frac{d\xi'}{\xi'} Z_{ij}^f\left(\frac{\xi}{\xi'}, \mu\right) f_j(\xi', \mu), \quad (\text{A.14})$$

where $j = \{q, \bar{q}, g\}$, and the entries in the matrix $Z_{ij}^f(z, \mu)$ are a series of $1/\epsilon$ poles with coefficients in terms of the renormalized $\overline{\text{MS}}$ coupling $\alpha_s(\mu)$. At one loop with $d = 4 - 2\epsilon$, we have for the standard gluon PDF [96],

$$\begin{aligned} Z_{gg}^f(z, \mu) &= \delta(1-z) + \frac{1}{\epsilon} \frac{\alpha_s(\mu)}{2\pi} \theta(z) \left[C_A P_{gg}(z) + \frac{1}{2} \beta_0 \delta(1-z) \right], \\ Z_{gq}^f(z, \mu) &= \frac{1}{\epsilon} \frac{\alpha_s(\mu) C_F}{2\pi} \theta(z) P_{gq}(z), \end{aligned} \quad (\text{A.15})$$

where $\beta_0 = (11C_A - 4n_f T_f)/3$, is the lowest order coefficient of the QCD β function, and the $g \rightarrow gg$ and $q \rightarrow gq$ splitting functions are

$$\begin{aligned} P_{gg}(z) &= 2\mathcal{L}_0(1-z)z + 2\theta(1-z) \left[\frac{1-z}{z} + z(1-z) \right] \\ &= 2\theta(1-z) \left[\frac{z}{(1-z)_+} + \frac{1-z}{z} + z(1-z) \right], \\ P_{gq}(z) &= \theta(1-z) \frac{1+(1-z)^2}{z}, \end{aligned} \quad (\text{A.16})$$

with $\mathcal{L}_0(1-z) = [\theta(1-z)/(1-z)]_+$ defined in eq. (A.44).

Expanding eq. (A.14) to one loop, we get

$$f_{g/j}^{\text{bare}(1)}(z) = Z_{gj}^{f(1)}(z, \mu) + f_{g/j}^{(1)}(z, \mu). \quad (\text{A.17})$$

In pure dimensional regularization, the only Lorentz invariant quantity $f_{g/j}^{\text{bare}}(z)$ can depend on is z . Since z is dimensionless, all loop diagrams contributing to the PDF calculation

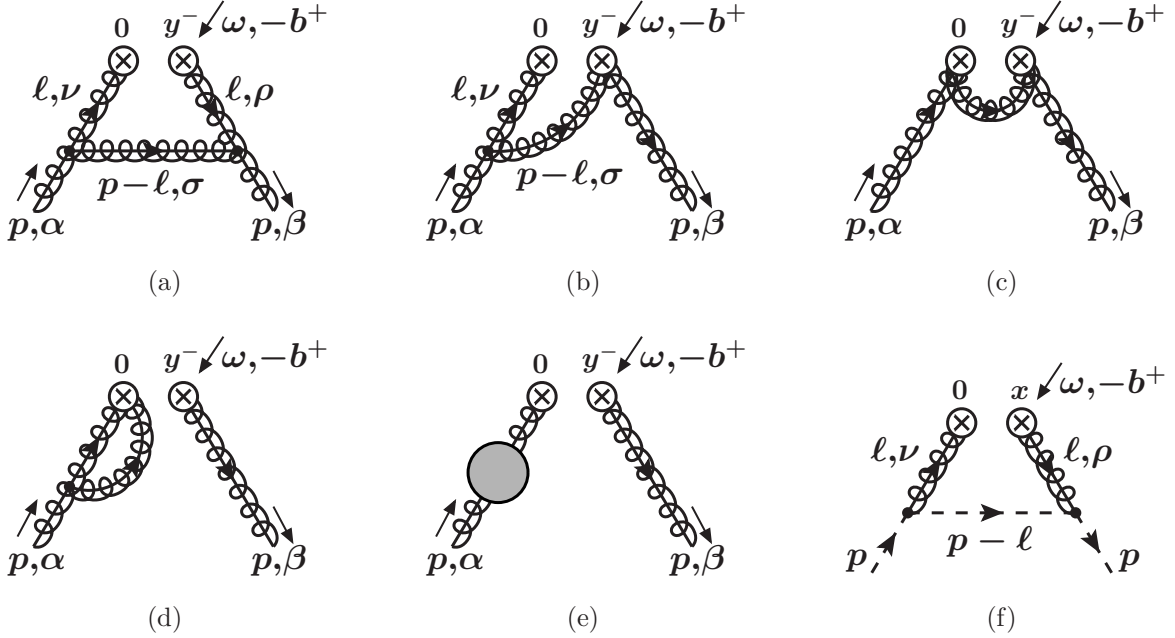


Figure 20. One-loop Feynman diagrams for the gluon beam function. The minus momentum ω is incoming at the vertex and the b^+ momentum is outgoing. Graphs (b), (d), and (e) have symmetric counterparts, which are equal to the ones shown. The corresponding diagrams with the external lines crossed or involving a four-gluon vertex vanish and are not shown.

vanish, $f_{g/j}^{\text{bare}(1)}(z) = 0$, meaning that the IR and UV divergences in $f_{g/j}^{\text{bare}(1)}(z)$ are equal with opposite signs. Thus, from eqs. (A.17) and (A.15) we get

$$\begin{aligned}
 f_{g/g}^{(1)}(z, \mu) &= -\frac{1}{\epsilon} \frac{\alpha_s(\mu)}{2\pi} \theta(z) \left[C_A P_{gg}(z) + \frac{1}{2} \beta_0 \delta(1-z) \right], \\
 f_{g/q}^{(1)}(z, \mu) &= -\frac{1}{\epsilon} \frac{\alpha_s(\mu) C_F}{2\pi} \theta(z) P_{qg}(z),
 \end{aligned}
 \tag{A.18}$$

where the ϵ poles are IR divergences.

A.3 The Gluon Beam Function at One Loop

We now turn to the one-loop calculation of the gluon beam function. The relevant one-loop diagrams are shown in figure 20, with the Feynman rules given below in eq. (A.21). Regulating both the UV and IR in dimensional regularization, the virtual diagram in figure 20(d) and its symmetric counterpart vanish because there is only the p^- momentum of the external gluon flowing into the loop, which is insufficient to give a nonzero Lorentz-invariant result for the loop integral. The diagram in figure 20(e), corresponding to the contribution from wave-function renormalization, vanishes for the same reason. Thus, in the on-shell scheme, both the wave-function renormalization constant Z_ξ as well as the residue R_ξ entering the LSZ formula are equal to one. (A different scheme would give contributions to both Z_ξ and



Figure 21. The SCET Feynman rules for the gluon field strength at $\mathcal{O}(g^0)$ (a) and $\mathcal{O}(g)$ (b).

R_ξ that cancel each other in the final result.) The diagram in figure 20(c) vanishes, because the external gluons have perpendicular polarization, so contracting the two $\mathcal{B}_{n\perp}^{(1)}$ in eq. (A.21) leads to $\bar{n} \cdot \bar{n} = 0$ in the numerator.

Hence, the only diagrams we have to compute are those in figures 20(a) and 20(b) (plus its symmetric counterpart), which determine $B_{g/g}^{\text{bare}(1)}(t, z)$, and figure 20(f), which determines $B_{g/q}^{\text{bare}(1)}(t, z)$. Since the diagrams have real radiation in the intermediate state, we can compute them as the discontinuity of the matrix element of the corresponding time-ordered product of fields [68]

$$B_{g/j}^{\text{bare}}(t, \omega/P^-) = -\theta(\omega) \text{Disc}_{t>0} \int \frac{dy^-}{4\pi} e^{ity^-/(2\omega)} \times \left\langle j_n(p^-) \left| T \left\{ \mathcal{B}_{n\perp\mu}^c \left(y^- \frac{n}{2} \right) [\delta(\omega - \bar{\mathcal{P}}_n) \mathcal{B}_{n\perp}^{\mu c}(0)] \right\} \right| j_n(p^-) \right\rangle. \quad (\text{A.19})$$

For our calculation we need the Feynman rules for the SCET gluon field strength

$$\mathcal{B}_{n\perp}^\mu = \frac{1}{g} \left[W_n^\dagger iD_{n\perp}^\mu W_n \right] \quad (\text{A.20})$$

with one and two external gluons. They are illustrated in figure 21 and are given by

$$\text{figure 21(a)} = \delta^{ca} \left(g_\perp^{\mu\alpha} - \frac{p_\perp^\mu \bar{n}^\alpha}{\bar{n} \cdot p} \right) \equiv \delta^{ca} \mathcal{B}_{n\perp}^{(0)\mu\alpha}(p), \quad (\text{A.21})$$

$$\text{figure 21(b)} = igf^{cab} \left[\frac{g_\perp^{\mu\beta} \bar{n}^\alpha}{\bar{n} \cdot p} - \frac{g_\perp^{\mu\alpha} \bar{n}^\beta}{\bar{n} \cdot q} + \left(\frac{p_\perp^\mu}{\bar{n} \cdot q} - \frac{q_\perp^\mu}{\bar{n} \cdot p} \right) \frac{\bar{n}^\alpha \bar{n}^\beta}{\bar{n} \cdot (p+q)} \right] \equiv igf^{cab} \mathcal{B}_{n\perp}^{(1)\mu\alpha\beta}(p, q),$$

where p and q are both taken as incoming. We abbreviate the triple gluon vertex as

$$gf^{abc} [g^{\mu\nu} (p_1 - p_2)^\rho + g^{\nu\rho} (p_2 - p_3)^\mu + g^{\rho\mu} (p_3 - p_1)^\nu] \equiv gf^{abc} V_3^{\mu\nu\rho}(p_1, p_2, p_3), \quad (\text{A.22})$$

where all momenta are incoming and momentum conservation holds, $p_1 + p_2 + p_3 = 0$. Finally, figure 20(e) requires the collinear quark-gluon vertex, which we write as

$$igT^a \left(n^\mu + \frac{\not{p}_\perp \gamma_\perp^\mu}{\bar{n} \cdot p} + \frac{\gamma_\perp^\mu \not{q}_\perp}{\bar{n} \cdot q} - \frac{\not{p}_\perp \not{q}_\perp}{\bar{n} \cdot p \bar{n} \cdot q} \bar{n}^\mu \right) \frac{\not{\eta}}{2} \equiv igT^a V_n^\mu(p, q) \frac{\not{\eta}}{2}, \quad (\text{A.23})$$

where p and q are the momenta of the outgoing and incoming quark lines, respectively, so the gluon carries incoming momentum $p - q$.

Let us start with the diagram in figure 20(a). The average over the polarizations of the external gluons with momentum $p^\mu = p^- n^\mu / 2$ gives

$$\frac{1}{d-2} \sum_{\text{pol}} \varepsilon^\alpha \varepsilon^{*\beta} = -\frac{g_\perp^{\alpha\beta}}{d-2}, \quad (\text{A.24})$$

where $d = 4 - 2\epsilon$. We also average over the color of the external gluons. This choice for the polarizations and colors of the external states is just a matter of calculational convenience. Using states with fixed polarization and color gives identical results. To make our expressions more palatable, we first perform the color algebra, which yields

$$\frac{\delta^{ab}}{N_c^2 - 1} f^{aec} f^{bde} \delta^{fc} \delta^{fd} = -C_A. \quad (\text{A.25})$$

The diagram is then given by

figure 20(a)

$$\begin{aligned} &= -i \left(\frac{e^{\gamma_E} \mu^2}{4\pi} \right)^\epsilon g^2 C_A \theta(\omega) \text{Disc}_{t>0} \int \frac{d^d \ell}{(2\pi)^d} \frac{\delta(\ell^- - \omega) \delta(\ell^+ + b^+)}{(\ell^2 + i0)^2 [(\ell - p)^2 + i0]} \\ &\quad \times \frac{g_{\perp\alpha}^\beta}{d-2} V_3^{\alpha\sigma\nu}(p, \ell - p, -\ell) V_{3\beta\rho\sigma}(-p, \ell, p - \ell) \mathcal{B}_{n_\perp\mu\nu}^{(0)}(\ell) \mathcal{B}_{n_\perp}^{(0)\mu\rho}(-\ell) \\ &= -i \left(\frac{e^{\gamma_E} \mu^2}{4\pi} \right)^\epsilon \frac{g^2 C_A}{(2\pi)^2} \theta(z) \text{Disc}_{t>0} \int_0^1 d\alpha (1 - \alpha) \int \frac{d^{d-2} \vec{\ell}_\perp}{(2\pi)^{d-2}} \frac{(5 + 4/z^2) \vec{\ell}_\perp^2 + (1 + 1/z)t}{[\vec{\ell}_\perp^2 + t(1 - \alpha/z)]^3} \\ &= \frac{\alpha_s(\mu) C_A}{2\pi} \theta(z) \theta(1 - z) 2 \left[\frac{1 - z}{z} + z(1 - z) + \frac{z}{2} \right] \Gamma(1 + \epsilon) (e^{\gamma_E} \mu^2)^\epsilon \frac{\sin \pi \epsilon}{\pi \epsilon} \frac{\theta(t)}{t^{1+\epsilon}} \left(\frac{z}{1 - z} \right)^\epsilon. \end{aligned} \quad (\text{A.26})$$

In the second line we integrated ℓ^+ and ℓ^- and introduced a Feynman parameter α . The last line follows from the standard integrals and the discontinuities listed in appendix A.4. Expanding in ϵ , using eq. (A.45), we arrive at

$$\text{figure 20(a)} = \frac{\alpha_s(\mu) C_A}{2\pi} \theta(z) \theta(1 - z) 2 \left[\frac{1 - z}{z} + z(1 - z) + \frac{z}{2} \right] \left[\delta(t) \left(-\frac{1}{\epsilon} + \ln \frac{1 - z}{z} \right) + \frac{1}{\mu^2} \mathcal{L}_0 \left(\frac{t}{\mu^2} \right) \right]. \quad (\text{A.27})$$

The color algebra for the diagram in figure 20(b) yields

$$\frac{\delta^{ab}}{N_c^2 - 1} f^{aec} \delta^{fc} f^{feb} = -C_A. \quad (\text{A.28})$$

Including a factor of two for its mirror graph, we get

$$\begin{aligned}
\text{figure 20(b)} &= -2i \left(\frac{e^{\gamma_E} \mu^2}{4\pi} \right)^\epsilon g^2 C_A \theta(\omega) \text{Disc}_{t>0} \int \frac{d^d \ell}{(2\pi)^d} \frac{\delta(\ell^- - \omega) \delta(\ell^+ + b^+)}{(\ell^2 + i0) [(\ell - p)^2 + i0]} \\
&\quad \times \frac{g_{\perp\alpha}^\beta}{d-2} V_3^{\alpha\sigma\nu}(p, \ell - p, -\ell) \mathcal{B}_{n\perp\mu\nu}^{(0)}(\ell) \mathcal{B}_{n\perp\sigma\beta}^{(1)\mu}(p - \ell, -p) \\
&= -i \left(\frac{e^{\gamma_E} \mu^2}{4\pi} \right)^\epsilon \frac{g^2 C_A}{(2\pi)^2} \theta(z) \frac{1+z}{1-z} \text{Disc}_{t>0} \int_0^1 d\alpha \int \frac{d^{d-2} \vec{\ell}_\perp}{(2\pi)^{d-2}} \frac{1}{[\vec{\ell}_\perp^2 + t(1 - \alpha/z)]^2} \\
&= \frac{\alpha_s(\mu) C_A}{2\pi} \theta(z) (1+z) z^{1+\epsilon} \frac{\theta(1-z)}{(1-z)^{1+\epsilon}} \Gamma(1+\epsilon) (\epsilon^{\gamma_E} \mu^2)^\epsilon \frac{\sin \pi \epsilon}{\pi \epsilon} \frac{\theta(t)}{t^{1+\epsilon}}, \quad (\text{A.29})
\end{aligned}$$

using again the relations listed in appendix A.4. Expanding in ϵ yields

$$\begin{aligned}
\text{figure 20(b)} &= \frac{\alpha_s(\mu) C_A}{2\pi} \theta(z) \left\{ \left[-\frac{1}{\epsilon} \delta(t) + \frac{1}{\mu^2} \mathcal{L}_0 \left(\frac{t}{\mu^2} \right) \right] \left[-\frac{2}{\epsilon} \delta(1-z) + \mathcal{L}_0(1-z) z(1+z) \right] \right. \\
&\quad \left. + \frac{2}{\mu^2} \mathcal{L}_1 \left(\frac{t}{\mu^2} \right) \delta(1-z) + \delta(t) z(1+z) \left[\mathcal{L}_1(1-z) - \mathcal{L}_0(1-z) \ln z - \frac{\pi^2}{12} \delta(1-z) \right] \right\}. \quad (\text{A.30})
\end{aligned}$$

Note that crossing the external lines of these diagrams corresponds to $p \rightarrow -p$ (the polarization and color are symmetric and hence unaffected). By changing $\ell \rightarrow -\ell$ this yields the same as the original diagram with the replacement $\delta(\ell^- - \omega) \delta(\ell^+ + b^+) \rightarrow \delta(\ell^- + \omega) \delta(\ell^+ - b^+)$ which leads to

$$\Delta \equiv \left(1 - \frac{\alpha}{z} \right) t \rightarrow \left(1 + \frac{\alpha}{z} \right) t \quad (\text{A.31})$$

in the denominator of the loop integrals. Since $\alpha, z > 0$ these graphs have no discontinuity for $t > 0$ and vanish. Other one-loop diagrams that could in principle connect the two gluon fields, e.g. involving a four gluon vertex, also vanish, because they require to cut one of the external lines entering the gluon operator, which sets $\Delta = t$ in the loop integral and leads to a vanishing discontinuity for $t > 0$.

Adding up the two nonvanishing diagrams in figures 20(a) and 20(b), we find

$$\begin{aligned}
B_{g/g}^{\text{bare}(1)}(t, z) &= \frac{\alpha_s(\mu) C_A}{2\pi} \theta(z) \left\{ \left[\frac{2}{\epsilon^2} \delta(t) - \frac{2}{\epsilon} \frac{1}{\mu^2} \mathcal{L}_0 \left(\frac{t}{\mu^2} \right) \right] \delta(1-z) - \frac{1}{\epsilon} \delta(t) P_{gg}(z) \right. \\
&\quad + \frac{2}{\mu^2} \mathcal{L}_1 \left(\frac{t}{\mu^2} \right) \delta(1-z) + \frac{1}{\mu^2} \mathcal{L}_0 \left(\frac{t}{\mu^2} \right) P_{gg}(z) \\
&\quad \left. + \delta(t) \left[\mathcal{L}_1(1-z) \frac{2(1-z+z^2)^2}{z} - P_{gg}(z) \ln z - \frac{\pi^2}{6} \delta(1-z) \right] \right\}, \quad (\text{A.32})
\end{aligned}$$

where $P_{gg}(z)$ is the $g \rightarrow gg$ splitting function given in eq. (A.16).

The mixing contribution of the quark PDF into the gluon beam function originates from the diagram in figure 20(f). The spin and color averages are

$$\frac{1}{2} \sum_{\text{spins}} u_n(p) \bar{u}_n(p) = \frac{1}{2} \not{p}, \quad \frac{1}{N_c} \text{tr}[T^a T^b] \delta^{ab} = C_F. \quad (\text{A.33})$$

The diagram is thus given by

figure 20(f)

$$\begin{aligned}
&= -i \left(\frac{e^{\gamma_E} \mu^2}{4\pi} \right)^\epsilon g^2 C_F \theta(\omega) \text{Disc}_{t>0} \int \frac{d^d \ell}{(2\pi)^d} \frac{(p^- - \ell^-) \delta(\ell^- - \omega) \delta(\ell^+ + b^+)}{(\ell^2 + i0)^2 [(p - \ell)^2 + i0]} \\
&\quad \times \bar{u}_n(p) V_n^\rho(p, p - \ell) V_{n\nu}(p - \ell, p) \frac{\not{\ell}}{2} u_n(p) \mathcal{B}_{n\perp}^{(0)\mu\nu}(\ell) \mathcal{B}_{n\perp\mu\rho}^{(0)}(-\ell) \\
&= i \left(\frac{e^{\gamma_E} \mu^2}{4\pi} \right)^\epsilon \frac{g^2 C_F}{(2\pi)^2} \theta(z) \left(\frac{d-2}{1-z} + \frac{4}{z^2} \right) \text{Disc}_{t>0} \int_0^1 d\alpha (1-\alpha) \int \frac{d^{d-2} \vec{\ell}_\perp}{(2\pi)^{d-2}} \frac{\ell_\perp^2}{[\ell_\perp^2 + t(1-\alpha/z)]^3} \\
&= \frac{\alpha_s(\mu) C_F}{2\pi} \theta(z) \theta(1-z) \Gamma(1+\epsilon) (e^{\gamma_E} \mu^2)^\epsilon \left[\frac{1+(1-z)^2}{z} - \epsilon z \right] \frac{\sin \pi \epsilon}{\pi \epsilon} \frac{\theta(t)}{t^{1+\epsilon}} \left(\frac{z}{1-z} \right)^\epsilon.
\end{aligned} \tag{A.34}$$

This is the same loop integral and discontinuity as in figure 20(a). For the crossed graph with the external lines interchanged, we can again change $\ell \rightarrow -\ell$ to obtain the same expression up to $\delta(\ell^- - \omega) \delta(\ell^+ + b^+) \rightarrow \delta(\ell^- + \omega) \delta(\ell^+ - b^+)$, which leads to a vanishing discontinuity as before. Expanding in ϵ , we obtain

$$\begin{aligned}
B_{g/q}^{\text{bare}(1)}(t, z) &= \frac{\alpha_s(\mu) C_F}{2\pi} \theta(z) \left\{ \frac{1}{\mu^2} \mathcal{L}_0 \left(\frac{t}{\mu^2} \right) P_{gq}(z) \right. \\
&\quad \left. + \delta(t) \left[P_{gq}(z) \left(-\frac{1}{\epsilon} + \ln \frac{1-z}{z} \right) + \theta(1-z) z \right] \right\},
\end{aligned} \tag{A.35}$$

with $P_{gq}(z)$ as in eq. (A.16). The matrix element with external antiquarks gives the same result, so the mixing contributions from quarks and antiquarks are identical.

The renormalized matrix elements $B_{g/j}(t, z, \mu)$ are given in terms of the bare ones as [68]

$$B_{g/j}^{\text{bare}}(t, z) = \int dt' Z_B^g(t-t', \mu) B_{g/j}(t', z, \mu). \tag{A.36}$$

Since $\gamma_B^g(t, \mu) = -\mu \frac{d}{d\mu} Z_B^g(t, \mu)$, the NLO counterterm follows from the one-loop anomalous dimension in eq. (A.5) with $\Gamma_{\text{cusp}}^g(\alpha_s) = C_A \alpha_s / \pi$ and $\gamma_B^g(\alpha_s) = \beta_0 \alpha_s / (2\pi)$ (see appendix B),

$$Z_B^g(t, \mu) = \delta(t) + \frac{\alpha_s(\mu)}{2\pi} \left\{ 2C_A \left[\frac{1}{\epsilon^2} \delta(t) - \frac{1}{\epsilon} \frac{1}{\mu^2} \mathcal{L}_0 \left(\frac{t}{\mu^2} \right) \right] + \frac{1}{2\epsilon} \beta_0 \delta(t) \right\}. \tag{A.37}$$

Expanding eq. (A.36) to NLO and using the tree-level result for $B_{g/j}(t, z, \mu)$ in eq. (A.11), we find

$$B_{g/j}^{\text{bare}(1)}(t, z) = Z_B^{g(1)}(t, \mu) \delta_{gj} \delta(1-z) + B_{g/j}^{(1)}(t, z, \mu). \tag{A.38}$$

Note that the mixing contribution $B_{g/q}$ is UV finite and not renormalized. From eq. (A.37)

and our results in eqs. (A.32) and (A.35) we have

$$\begin{aligned}
B_{g/g}^{(1)}(t, z, \mu) &= \frac{\alpha_s(\mu)C_A}{2\pi} \theta(z) \left\{ -\frac{1}{\epsilon} \delta(t) \left[P_{gg}(z) + \frac{\beta_0}{2C_A} \delta(1-z) \right] \right. \\
&\quad + \frac{2}{\mu^2} \mathcal{L}_1\left(\frac{t}{\mu^2}\right) \delta(1-z) + \frac{1}{\mu^2} \mathcal{L}_0\left(\frac{t}{\mu^2}\right) P_{gg}(z) \\
&\quad \left. + \delta(t) \left[\mathcal{L}_1(1-z) \frac{2(1-z+z^2)^2}{z} - P_{gg}(z) \ln z - \frac{\pi^2}{6} \delta(1-z) \right] \right\}, \\
B_{g/q}^{(1)}(t, z, \mu) &= \frac{\alpha_s(\mu)C_F}{2\pi} \theta(z) \left\{ -\frac{1}{\epsilon} \delta(t) P_{gq}(z) \right. \\
&\quad \left. + \frac{1}{\mu^2} \mathcal{L}_0\left(\frac{t}{\mu^2}\right) P_{gq}(z) + \delta(t) \left[P_{gq}(z) \ln \frac{1-z}{z} + \theta(1-z)z \right] \right\}, \tag{A.39}
\end{aligned}$$

where all $1/\epsilon$ divergences are now IR divergences. Subtracting the one-loop PDF matrix elements in eq. (A.18) according to eq. (A.13), we see that the IR divergences precisely cancel between $B_{g/j}$ and $f_{g/j}$, and the finite terms in eq. (A.39) determine the one-loop matching coefficients $\mathcal{I}_{gj}(t, z, \mu)$ in eq. (2.14).

To compare our expression for $\mathcal{I}_{gg}^{(1)}(t, z, \mu)$ with the result of ref. [69], we take the moments

$$\begin{aligned}
\hat{C}_{II}^{(1)}(z, N) &= M^2 \int_0^1 dy y^N \mathcal{I}_{gg}^{(1)}[M^2(1-y), z, \mu] = \int_0^{M^2} dt \left(1 - \frac{t}{M^2}\right)^N \mathcal{I}_{gg}^{(1)}(t, z, \mu) \\
&= \frac{\alpha_s(\mu)C_A}{2\pi} \theta(z) \left[\ln^2\left(\frac{Ne^{\gamma_E} \mu^2}{M^2}\right) \delta(1-z) - \ln\left(\frac{Ne^{\gamma_E} \mu^2}{M^2}\right) P_{gg}(z) \right. \\
&\quad \left. + \mathcal{L}_1(1-z) \frac{2(1-z+z^2)^2}{z} - P_{gg}(z) \ln z \right] + \mathcal{O}\left(\frac{1}{N}\right), \tag{A.40}
\end{aligned}$$

where we used the approximation for the harmonic numbers at large N

$$H_N = \sum_{i=1}^N \frac{1}{i} = \ln N + \gamma_E + \mathcal{O}\left(\frac{1}{N}\right). \tag{A.41}$$

Our result in eq. (A.40) agrees with eq. (68) of ref. [69] except for a constant term $-\alpha_s C_A/\pi \delta(1-z)\pi^2/8$.

A.4 Integrals, Discontinuities, and Plus Distributions

Here we list various loop integrals that are needed for the calculation in appendix A.3:

$$\begin{aligned}
\int \frac{d^{d-2}\vec{\ell}_\perp}{(2\pi)^{d-2}} \frac{1}{(\vec{\ell}_\perp^2 + \Delta)^2} &= \frac{1}{(4\pi)^{1-\epsilon}} \Gamma(1+\epsilon) \Delta^{-1-\epsilon}, \\
\int \frac{d^{d-2}\vec{\ell}_\perp}{(2\pi)^{d-2}} \frac{1}{(\vec{\ell}_\perp^2 + \Delta)^3} &= \frac{1}{(4\pi)^{1-\epsilon}} \frac{\Gamma(2+\epsilon)}{2} \Delta^{-2-\epsilon}, \\
\int \frac{d^{d-2}\vec{\ell}_\perp}{(2\pi)^{d-2}} \frac{\vec{\ell}_\perp^2}{(\vec{\ell}_\perp^2 + \Delta)^3} &= \frac{1}{(4\pi)^{1-\epsilon}} (1-\epsilon) \frac{\Gamma(1+\epsilon)}{2} \Delta^{-1-\epsilon}. \tag{A.42}
\end{aligned}$$

To calculate the discontinuities of the various graphs we need the relations,

$$\begin{aligned}
-\theta(z)\frac{i}{2\pi}\text{Disc}_{t>0}\int_0^1 d\alpha\Delta^{-1-\epsilon} &= \theta(z)\frac{\sin\pi\epsilon}{\pi\epsilon}\frac{\theta(t)}{t^{1+\epsilon}}\theta(1-z)z^{1+\epsilon}(1-z)^{-\epsilon}, \\
-\theta(z)\frac{i}{2\pi}\text{Disc}_{t>0}\int_0^1 d\alpha(1-\alpha)\Delta^{-1-\epsilon} &= \theta(z)\frac{\sin\pi\epsilon}{\pi\epsilon(1-\epsilon)}\frac{\theta(t)}{t^{1+\epsilon}}\theta(1-z)z^{1+\epsilon}(1-z)^{1-\epsilon}, \\
-\theta(z)\frac{i}{2\pi}\text{Disc}_{t>0}\int_0^1 d\alpha(1-\alpha)t\Delta^{-2-\epsilon} &= \theta(z)\frac{\sin\pi\epsilon}{\pi\epsilon(1+\epsilon)}\frac{\theta(t)}{t^{1+\epsilon}}\theta(1-z)z^{2+\epsilon}(1-z)^{-\epsilon}. \quad (\text{A.43})
\end{aligned}$$

The plus distributions are defined as

$$\begin{aligned}
\mathcal{L}_n(x) &= \left[\frac{\theta(x)\ln^n x}{x}\right]_+ = \lim_{\beta\rightarrow 0}\left[\frac{\theta(x-\beta)\ln^n x}{x} + \delta(x-\beta)\frac{\ln^{n+1}\beta}{n+1}\right], \\
\mathcal{L}^\eta(x) &= \left[\frac{\theta(x)}{x^{1-\eta}}\right]_+ = \lim_{\beta\rightarrow 0}\left[\frac{\theta(x-\beta)}{x^{1-\eta}} + \delta(x-\beta)\frac{x^\eta-1}{\eta}\right], \quad (\text{A.44})
\end{aligned}$$

satisfying the boundary condition $\int_0^1 dz \mathcal{L}_n(z) = 0$. We also need the distribution identity,

$$\frac{1}{(1-z)^{1+\epsilon}} = -\frac{1}{\epsilon}\delta(1-z) + \mathcal{L}_0(1-z) - \epsilon\mathcal{L}_1(1-z) + \mathcal{O}(\epsilon^2). \quad (\text{A.45})$$

B Perturbative Results

B.1 Hard Function

The functions $F^{(0)}(z)$ and $F^{(1)}(z)$ which encode the m_t dependence of the hard Wilson coefficient in eq. (2.7) are given by

$$\begin{aligned}
F^{(0)}(z) &= \frac{3}{2z} - \frac{3}{2z}\left|1 - \frac{1}{z}\right| \begin{cases} \arcsin^2(\sqrt{z}), & 0 < z \leq 1, \\ \ln^2[-i(\sqrt{z} + \sqrt{z-1})], & z > 1, \end{cases} \\
F^{(1)}(z) &= \left(5 - \frac{38}{45}z - \frac{1289}{4725}z^2 - \frac{155}{1134}z^3 - \frac{5385047}{65488500}z^4\right)C_A \\
&\quad + \left(-3 + \frac{307}{90}z + \frac{25813}{18900}z^2 + \frac{3055907}{3969000}z^3 + \frac{659504801}{1309770000}z^4\right)C_F + \mathcal{O}(z^5). \quad (\text{B.1})
\end{aligned}$$

Here, $F^{(0)}(z)$ gives the well-known m_t dependence of the leading-order $gg \rightarrow H$ cross section given by the virtual top-quark loop. The full analytic m_t dependence of the virtual two-loop corrections to $gg \rightarrow H$ in terms of harmonic polylogarithms were obtained in refs. [76, 77]. Since the corresponding exact expression for $F^{(1)}(z)$ is very long, we use the results expanded in m_H^2/m_t^2 from ref. [79]. The additional m_t dependence coming from $F^{(1)}(z)$ is small and the expansion is converging very quickly, so the expanded result is completely sufficient for

practical purposes. For completeness we also give the leading terms in $F^{(2)}(z)$,

$$\begin{aligned}
F^{(2)}(z) &= (7C_A^2 + 11C_A C_F - 6C_F \beta_0) \ln(-4z - i0) + \left(-\frac{419}{27} + \frac{7\pi^2}{6} + \frac{\pi^4}{72} - 44\zeta_3\right) C_A^2 \\
&+ \left(-\frac{217}{2} - \frac{\pi^2}{2} + 44\zeta_3\right) C_A C_F + \left(\frac{2255}{108} + \frac{5\pi^2}{12} + \frac{23\zeta_3}{3}\right) C_A \beta_0 - \frac{5}{6} C_A T_F \\
&+ \frac{27}{2} C_F^2 + \left(\frac{41}{2} - 12\zeta_3\right) C_F \beta_0 - \frac{4}{3} C_F T_F + \mathcal{O}(z). \tag{B.2}
\end{aligned}$$

The first few higher-order terms in z can be extracted from the results in refs. [78, 79].

Alternatively to the one-step matching we use, one can perform a two-step matching by treating $m_H \ll m_t$ as done in refs. [49, 51, 59, 85]. In this case, one first integrates out the top quark at the scale $\mu_t \simeq m_t$ and then matches from QCD onto SCET at $\mu_H \simeq m_H$. In this way one neglects power corrections of $\mathcal{O}(m_H/m_t)$ but in turn the running between μ_t and μ_H allows one to sum logarithms of m_H/m_t . We first integrate out the top loop to get the effective Hamiltonian [12, 13]

$$\mathcal{H}_{\text{eff}} = -C_1(m_t, \mu_t) \frac{H}{12\pi v} G^{\mu\nu a} G_{\mu\nu}^a, \quad C_1(m_t, \mu_t) = \alpha_s(\mu_t) \left[1 + \frac{\alpha_s(\mu_t)}{4\pi} (5C_A - 3C_F)\right], \tag{B.3}$$

where as before $\alpha_s(\mu_t)$ is evaluated for $n_f = 5$ flavors and at higher order $C_1(m_t, \mu_t)$ contains logarithms of m_t/μ_t . In the second step, we integrate out hard off-shell modes by matching onto the SCET operator in eq. (2.5),

$$\begin{aligned}
-G_{\mu\nu}^a G^{\mu\nu a} &= C_2(q^2, \mu_H) q^2 g_{\mu\nu} \mathcal{B}_\perp^{\mu c} \mathcal{B}_\perp^{\nu c}, \\
C_2(q^2, \mu_H) &= 1 + \frac{\alpha_s(\mu_H)}{4\pi} C_A \left(-\ln^2 \frac{-q^2 - i0}{\mu_H^2} + \frac{\pi^2}{6}\right). \tag{B.4}
\end{aligned}$$

The SCET matching coefficient $C_2(q^2, \mu_H)$ corresponds to the IR finite parts of the gluon form factor. Combining the two matching steps we obtain

$$\begin{aligned}
C_{ggH}(m_t, q^2, \mu) &= C_1(m_t, \mu) C_2(q^2, \mu) \\
&= \alpha_s(\mu) \left\{ 1 + \frac{\alpha_s(\mu)}{4\pi} \left[\left(-\ln^2 \frac{-q^2 - i0}{\mu^2} + 5 + \frac{\pi^2}{6}\right) C_A - 3C_F \right] \right\}. \tag{B.5}
\end{aligned}$$

In the second line we expanded both coefficients at the same scale μ , which reproduces the $m_t \rightarrow \infty$ limit of eq. (2.7). At NNLO, this gives the leading terms of $F^{(2)}(z)$ in eq. (B.2). The strict $m_t \rightarrow \infty$ limit is formally necessary for a consistent two step matching. Note that in the $m_t \rightarrow \infty$ limit that is often used in the literature, the full m_t dependence of the leading-order cross section in the overall factor $F^{(0)}(z)$ in eq. (2.7) is included, which then turns out to be a very good approximation for the total cross section [14, 18, 19, 97]. Considering the virtual corrections only, this way of defining the $m_t \rightarrow \infty$ limit is equivalent to the one-step matching in eq. (2.7) where one neglects the weak m_t dependence of $F^{(1)}(z)$ and using $F^{(1)}(0)$.

B.2 Beam Function

We obtain the μ_B -dependent terms in the two-loop contribution $\mathcal{I}_{ij}^{(2)}$ in eq. (2.13) by perturbatively solving the two-loop RGE of the matching coefficients \mathcal{I}_{gj} , given by [68]

$$\mu \frac{d}{d\mu} \mathcal{I}_{gj}(t, z, \mu) = \sum_k \int dt' \frac{dz'}{z'} \mathcal{I}_{gk}(t - t', \frac{z}{z'}, \mu) \left[\gamma_B^g(t', \mu) \delta_{kj} \delta(1 - z') - \delta(t') \gamma_{kj}^f(z', \mu) \right], \quad (\text{B.6})$$

where the $\gamma_B^g(t, \mu)$ is the anomalous dimensions of the beam function in eq. (A.5) and $\gamma_{kj}^f(z, \mu)$ that of the PDFs. We obtain

$$\begin{aligned} \mathcal{I}_{gg}^{(2)}(t, z, \mu_B) &= \frac{1}{\mu_B^2} \mathcal{L}_3\left(\frac{t}{\mu_B^2}\right) 8C_A^2 \delta(1 - z) + \frac{1}{\mu_B^2} \mathcal{L}_2\left(\frac{t}{\mu_B^2}\right) [12C_A^2 P_{gg}(z) - 2C_A \beta_0 \delta(1 - z)] \\ &\quad + \frac{1}{\mu_B^2} \mathcal{L}_1\left(\frac{t}{\mu_B^2}\right) \left\{ 4C_A^2 \left[\left(\frac{4}{3} - \pi^2\right) \delta(1 - z) + 2\mathcal{I}_{gg}^{(1,\delta)}(z) + (P_{gg} \otimes P_{gg})(z) \right] \right. \\ &\quad \left. + 2C_A \beta_0 \left[\frac{10}{3} \delta(1 - z) - P_{gg}(z) \right] + 8C_F T_F n_f (P_{gq} \otimes P_{qg})(z) \right\} \\ &\quad + \frac{1}{\mu_B^2} \mathcal{L}_0\left(\frac{t}{\mu_B^2}\right) \left\{ 4C_A^2 \left[\left(-\frac{7}{9} + 8\zeta_3\right) \delta(1 - z) - \frac{\pi^2}{3} P_{gg}(z) + (\mathcal{I}_{gg}^{(1,\delta)} \otimes P_{gg})(z) \right] \right. \\ &\quad \left. + C_A \beta_0 \left[\left(-\frac{92}{9} + \frac{\pi^2}{3}\right) \delta(1 - z) - 2\mathcal{I}_{gg}^{(1,\delta)}(z) \right] \right. \\ &\quad \left. + C_F T_F n_f [4\delta(1 - z) + 8(\mathcal{I}_{gq}^{(1,\delta)} \otimes P_{qg})(z)] + 4P_{gg}^{(1)}(z) \right\} + 4\delta(t) \mathcal{I}_{gg}^{(2,\delta)}(z), \\ \mathcal{I}_{gq}^{(2)}(t, z, \mu_B) &= \frac{1}{\mu_B^2} \mathcal{L}_2\left(\frac{t}{\mu_B^2}\right) 12C_A C_F P_{gq}(z) + \frac{1}{\mu_B^2} \mathcal{L}_1\left(\frac{t}{\mu_B^2}\right) \left\{ 4C_F^2 (P_{gq} \otimes P_{qg})(z) \right. \\ &\quad \left. + 4C_A C_F [(P_{gg} \otimes P_{gq})(z) + 2\mathcal{I}_{gq}^{(1,\delta)}(z)] - 4C_F \beta_0 P_{gq}(z) \right\} \\ &\quad + \frac{1}{\mu_B^2} \mathcal{L}_0\left(\frac{t}{\mu_B^2}\right) \left\{ 4C_A C_F \left[-\frac{\pi^2}{3} P_{gq}(z) + (\mathcal{I}_{gq}^{(1,\delta)} \otimes P_{gq})(z) \right] \right. \\ &\quad \left. + 4C_F^2 (\mathcal{I}_{gq}^{(1,\delta)} \otimes P_{qq})(z) - 4C_F \beta_0 \mathcal{I}_{gq}^{(1,\delta)}(z) + 4P_{gq}^{(2)}(z) \right\} + 4\delta(t) \mathcal{I}_{gq}^{(2,\delta)}(z). \end{aligned} \quad (\text{B.7})$$

The μ_B -independent terms $\mathcal{I}_{gj}^{(2,\delta)}(z)$ require the two-loop calculation of gluon beam function which is not yet available. The one-loop functions $\mathcal{I}_{gj}^{(1,\delta)}(z)$ entering in the above expressions were already given in eq. (2.15). The quark and gluon splitting functions are

$$\begin{aligned} P_{gg}(z) &= 2\mathcal{L}_0(1 - z)z + 2\theta(1 - z) \left[\frac{1 - z}{z} + z(1 - z) \right], \\ P_{gq}(z) &= \theta(1 - z) \frac{1 + (1 - z)^2}{z}, \\ P_{qq}(z) &= \mathcal{L}_0(1 - z)(1 + z^2) + \frac{3}{2} \delta(1 - z), \\ P_{qg}(z) &= \theta(1 - z) [(1 - z)^2 + z^2]. \end{aligned} \quad (\text{B.8})$$

The two-loop splitting functions were calculated in refs. [98, 99] and are given by [99]

$$\begin{aligned}
P_{gg}^{(1)}(z) &= C_A^2 \left\{ \frac{1}{3} (4 - \pi^2) \mathcal{L}_0(1-z) + (-1 + 3\zeta_3) \delta(1-z) + \frac{-253 + 294z - 318z^2 + 253z^3}{18z} \right. \\
&\quad + \frac{-1 + 2z - z^2 + z^3}{3z} \pi^2 - \frac{4}{3} (9 + 11z^2) \ln z + \frac{2(1+z-z^2)^2}{1-z^2} \ln^2 z \\
&\quad \left. - 2P_{gg}(z) \ln z \ln(1-z) - 2P_{gg}(-z) \left[\ln z \ln(1+z) + \text{Li}_2(-z) + \frac{\pi^2}{12} \right] \right\} \\
&\quad + C_A \beta_0 \left[\frac{5}{3} \mathcal{L}_0(1-z) + \delta(1-z) + \frac{23 - 29z + 19z^2 - 23z^3}{6z} + (1+z) \ln z \right] \\
&\quad + C_F T_F n_f \left[-\delta(1-z) + \frac{4(1-12z+6z^2+5z^3)}{3z} - 2(1+z) \ln^2 z - 2(3+5z) \ln z \right], \\
P_{gq}^{(1)}(z) &= C_A C_F \left\{ \frac{-101 + 129z - 51z^2 + 44z^3}{9z} - \frac{1}{3} (36 + 15z + 8z^2) \ln z + 2z \ln(1-z) \right. \\
&\quad + (2+z) \ln^2 z - P_{gq}(z) \left[2 \ln z \ln(1-z) - \ln^2(1-z) + \frac{\pi^2}{6} \right] \\
&\quad \left. - 2P_{gq}(-z) \left[\ln z \ln(1+z) + \text{Li}_2(-z) + \frac{\pi^2}{12} \right] \right\} \\
&\quad + C_F^2 \left[-\frac{1}{2} (5+7z) + \frac{1}{2} (4+7z) \ln z + \frac{-6+6z-5z^2}{z} \ln(1-z) - \frac{1}{2} (2-z) \ln^2 z \right. \\
&\quad \left. - P_{gq}(z) \ln^2(1-z) \right] + C_F \beta_0 \left[\frac{2(5-5z+4z^2)}{3z} + P_{gq}(z) \ln(1-z) \right]. \tag{B.9}
\end{aligned}$$

The convolution of two splitting functions is defined as (the index j is not summed over)

$$(P_{ij} \otimes P_{jk})(z) = \int_z^1 \frac{dw}{w} P_{ij}(w) P_{jk}\left(\frac{z}{w}\right), \tag{B.10}$$

and analogously for the convolution $(\mathcal{I}_{ij}^{(1,\delta)} \otimes P_{jk})$. The necessary convolutions are

$$\begin{aligned}
(P_{gq} \otimes P_{gq})(z) &= \frac{4 + 3z - 3z^2 - 4z^3}{3z} + 2(1+z) \ln z, \\
(P_{gq} \otimes P_{qq})(z) &= 2 - \frac{z}{2} + (2-z) \ln z + \frac{2(2-2z+z^2)}{z} \ln(1-z), \\
(P_{gg} \otimes P_{gq})(z) &= \frac{-31 + 24z + 3z^2 + 4z^3}{3z} - \frac{4(1+z+z^2)}{z} \ln z + \frac{2(2-2z+z^2)}{z} \ln(1-z), \\
(P_{gg} \otimes P_{gg})(z) &= 8\mathcal{L}_1(1-z) - \frac{2\pi^2}{3} \delta(1-z) + \frac{4(-11+9z-9z^2+11z^3)}{3z} \\
&\quad + \frac{4(-1-3z^2+4z^3-z^4)}{z(1-z)} \ln z + \frac{8(1-2z+z^2-z^3)}{z} \ln(1-z), \\
(\mathcal{I}_{gq}^{(1,\delta)} \otimes P_{gq})(z) &= \frac{-13 + 12z + 6z^2 - 5z^3}{9z} + \pi^2 \frac{1+z}{3} + \frac{-4 + 9z^2 + 4z^3}{3z} \ln z \\
&\quad + \frac{4 + 3z - 3z^2 - 4z^3}{3z} \ln(1-z) - (1+z) \ln^2 z - 2(1+z) \text{Li}_2(z), \\
(\mathcal{I}_{gq}^{(1,\delta)} \otimes P_{qq})(z) &= \frac{5 - 4z + 2z^2}{2z} + \pi^2 \frac{-4 + 6z - 3z^2}{6z} + \frac{-2-z}{2} \ln z + \frac{4+3z}{2} \ln(1-z)
\end{aligned}$$

$$\begin{aligned}
& + \frac{z-2}{2} \ln^2 z + \frac{2(2-2z+z^2)}{z} \ln(1-z)[\ln(1-z) - \ln z] + (z-2)\text{Li}_2(z), \\
(\mathcal{I}_{gg}^{(1,\delta)} \otimes P_{gq})(z) &= \frac{21-26z+5z^2}{6z} + \pi^2 \frac{-2-6z-3z^2}{6z} + \frac{9-30z-9z^2-4z^3}{3z} \ln z \\
& + \frac{-31+24z+3z^2+4z^3}{3z} \ln(1-z) + \frac{2(1+z+z^2)}{z} \ln^2 z \\
& + \frac{2-2z+z^2}{z} \ln(1-z)[\ln(1-z) - 2 \ln z] + (8+2z)\text{Li}_2(z), \\
(\mathcal{I}_{gg}^{(1,\delta)} \otimes P_{gg})(z) &= 6\mathcal{L}_2(1-z) - \pi^2 \mathcal{L}_0(1-z) + 4\zeta_3 \delta(1-z) + \frac{(1-z)(67-2z+67z^2)}{9z} \\
& + \pi^2 \frac{-3+2z-7z^2+3z^3}{3z} + \frac{2(11-21z+6z^2-22z^3)}{3z} \ln z \\
& + \frac{4(-11+9z-9z^2+11z^3)}{3z} \ln(1-z) + \frac{2(1+3z^2-4z^3+z^4)}{z(1-z)} \ln^2 z \\
& + \frac{8(-1+2z-3z^2+2z^3-z^4)}{z(1-z)} \ln z \ln(1-z) \\
& + \frac{6(1-2z+z^2-z^3)}{z} \ln^2(1-z) + 8(1+z)\text{Li}_2(z). \tag{B.11}
\end{aligned}$$

B.3 Renormalization Group Evolution

The hard Wilson coefficient satisfies the RGE

$$\begin{aligned}
\mu \frac{d}{d\mu} C_{ggH}(m_t, q^2, \mu) &= \gamma_H^g(q^2, \mu) C_{ggH}(m_t, q^2, \mu), \\
\gamma_H^g(q^2, \mu) &= \Gamma_{\text{cusp}}^g[\alpha_s(\mu)] \ln \frac{-q^2 - i0}{\mu^2} + \gamma_H^g[\alpha_s(\mu)], \tag{B.12}
\end{aligned}$$

whose solution gives eq. (2.10). The beam function RGE is given in eq. (A.4). The soft function satisfies an analogous RGE,

$$\begin{aligned}
\mu \frac{d}{d\mu} S_B^{gg}(k, \mu) &= \int dk' \gamma_S^g(k-k', \mu) S_B^{gg}(k', \mu), \\
\gamma_S^g(k, \mu) &= 4\Gamma_{\text{cusp}}^g[\alpha_s(\mu)] \frac{1}{\mu} \mathcal{L}_0\left(\frac{k}{\mu}\right) + \gamma_S^g[\alpha_s(\mu)] \delta(k), \tag{B.13}
\end{aligned}$$

whose solution yields eq. (2.24). The functions $K_\Gamma^i(\mu_0, \mu)$, $\eta_\Gamma^i(\mu_0, \mu)$, $K_\gamma(\mu_0, \mu)$ required for the RGE solutions of the hard, beam, and soft functions in section 2 are defined as

$$\begin{aligned}
K_\Gamma^i(\mu_0, \mu) &= \int_{\alpha_s(\mu_0)}^{\alpha_s(\mu)} \frac{d\alpha_s}{\beta(\alpha_s)} \Gamma_{\text{cusp}}^i(\alpha_s) \int_{\alpha_s(\mu_0)}^{\alpha_s} \frac{d\alpha'_s}{\beta(\alpha'_s)}, & \eta_\Gamma^i(\mu_0, \mu) &= \int_{\alpha_s(\mu_0)}^{\alpha_s(\mu)} \frac{d\alpha_s}{\beta(\alpha_s)} \Gamma_{\text{cusp}}^i(\alpha_s), \\
K_\gamma(\mu_0, \mu) &= \int_{\alpha_s(\mu_0)}^{\alpha_s(\mu)} \frac{d\alpha_s}{\beta(\alpha_s)} \gamma(\alpha_s). \tag{B.14}
\end{aligned}$$

Expanding the beta function and anomalous dimensions in powers of α_s ,

$$\beta(\alpha_s) = -2\alpha_s \sum_{n=0}^{\infty} \beta_n \left(\frac{\alpha_s}{4\pi}\right)^{n+1}, \quad \Gamma_{\text{cusp}}^i(\alpha_s) = \sum_{n=0}^{\infty} \Gamma_n^i \left(\frac{\alpha_s}{4\pi}\right)^{n+1}, \quad \gamma(\alpha_s) = \sum_{n=0}^{\infty} \gamma_n \left(\frac{\alpha_s}{4\pi}\right)^{n+1}, \quad (\text{B.15})$$

their explicit expressions at NNLL are (suppressing the superscript i on K_{Γ}^i , η_{Γ}^i and Γ_n^i),

$$\begin{aligned} K_{\Gamma}(\mu_0, \mu) &= -\frac{\Gamma_0}{4\beta_0^2} \left\{ \frac{4\pi}{\alpha_s(\mu_0)} \left(1 - \frac{1}{r} - \ln r\right) + \left(\frac{\Gamma_1}{\Gamma_0} - \frac{\beta_1}{\beta_0}\right)(1 - r + \ln r) + \frac{\beta_1}{2\beta_0} \ln^2 r \right. \\ &\quad \left. + \frac{\alpha_s(\mu_0)}{4\pi} \left[\left(\frac{\beta_1^2}{\beta_0^2} - \frac{\beta_2}{\beta_0}\right) \left(\frac{1-r^2}{2} + \ln r\right) + \left(\frac{\beta_1\Gamma_1}{\beta_0\Gamma_0} - \frac{\beta_1^2}{\beta_0^2}\right) (1-r + r \ln r) \right. \right. \\ &\quad \left. \left. - \left(\frac{\Gamma_2}{\Gamma_0} - \frac{\beta_1\Gamma_1}{\beta_0\Gamma_0}\right) \frac{(1-r)^2}{2} \right] \right\}, \\ \eta_{\Gamma}(\mu_0, \mu) &= -\frac{\Gamma_0}{2\beta_0} \left[\ln r + \frac{\alpha_s(\mu_0)}{4\pi} \left(\frac{\Gamma_1}{\Gamma_0} - \frac{\beta_1}{\beta_0}\right) (r-1) \right. \\ &\quad \left. + \frac{\alpha_s^2(\mu_0)}{16\pi^2} \left(\frac{\Gamma_2}{\Gamma_0} - \frac{\beta_1\Gamma_1}{\beta_0\Gamma_0} + \frac{\beta_1^2}{\beta_0^2} - \frac{\beta_2}{\beta_0}\right) \frac{r^2-1}{2} \right], \\ K_{\gamma}(\mu_0, \mu) &= -\frac{\gamma_0}{2\beta_0} \left[\ln r + \frac{\alpha_s(\mu_0)}{4\pi} \left(\frac{\gamma_1}{\gamma_0} - \frac{\beta_1}{\beta_0}\right) (r-1) \right]. \end{aligned} \quad (\text{B.16})$$

Here, $r = \alpha_s(\mu)/\alpha_s(\mu_0)$ and the running coupling at the scale μ is given in terms of that at the reference scale μ_0 by the three-loop expression

$$\frac{1}{\alpha_s(\mu)} = \frac{X}{\alpha_s(\mu_0)} + \frac{\beta_1}{4\pi\beta_0} \ln X + \frac{\alpha_s(\mu_0)}{16\pi^2} \left[\frac{\beta_2}{\beta_0} \left(1 - \frac{1}{X}\right) + \frac{\beta_1^2}{\beta_0^2} \left(\frac{\ln X}{X} + \frac{1}{X} - 1\right) \right], \quad (\text{B.17})$$

where $X \equiv 1 + \alpha_s(\mu_0)\beta_0 \ln(\mu/\mu_0)/(2\pi)$. At NNLL, we require the three-loop β function and gluon cusp anomalous dimension and the two-loop non-cusp anomalous dimensions. The coefficients of the $\overline{\text{MS}}$ β function to three loops are [100, 101]

$$\begin{aligned} \beta_0 &= \frac{11}{3} C_A - \frac{4}{3} T_F n_f, \\ \beta_1 &= \frac{34}{3} C_A^2 - \left(\frac{20}{3} C_A + 4C_F\right) T_F n_f, \\ \beta_2 &= \frac{2857}{54} C_A^3 + \left(C_F^2 - \frac{205}{18} C_F C_A - \frac{1415}{54} C_A^2\right) 2T_F n_f + \left(\frac{11}{9} C_F + \frac{79}{54} C_A\right) 4T_F^2 n_f^2. \end{aligned} \quad (\text{B.18})$$

The coefficients of the gluon cusp anomalous dimension in $\overline{\text{MS}}$ are [102]

$$\begin{aligned} \Gamma_0^g &= 4C_A, \\ \Gamma_1^g &= 4C_A \left[\left(\frac{67}{9} - \frac{\pi^2}{3}\right) C_A - \frac{20}{9} T_F n_f \right], \\ \Gamma_2^g &= 4C_A \left[\left(\frac{245}{6} - \frac{134\pi^2}{27} + \frac{11\pi^4}{45} + \frac{22\zeta_3}{3}\right) C_A^2 + \left(-\frac{418}{27} + \frac{40\pi^2}{27} - \frac{56\zeta_3}{3}\right) C_A T_F n_f \right. \\ &\quad \left. + \left(-\frac{55}{3} + 16\zeta_3\right) C_F T_F n_f - \frac{16}{27} T_F^2 n_f^2 \right], \end{aligned} \quad (\text{B.19})$$

and are equal to $C_A/C_F\Gamma_{0,1,2}^g$. The anomalous dimension coefficients for the hard Wilson coefficient to three loops are [59, 103, 104]

$$\begin{aligned}
\gamma_{H0}^g &= -2\beta_0, \\
\gamma_{H1}^g &= \left(-\frac{118}{9} + 4\zeta_3\right)C_A^2 + \left(-\frac{38}{9} + \frac{\pi^2}{3}\right)C_A\beta_0 - 2\beta_1, \\
\gamma_{H2}^g &= \left(-\frac{60875}{162} + \frac{634\pi^2}{81} + \frac{8\pi^4}{5} + \frac{1972\zeta_3}{9} - \frac{40\pi^2\zeta_3}{9} - 32\zeta_5\right)C_A^3 \\
&\quad + \left(\frac{7649}{54} + \frac{134\pi^2}{81} - \frac{61\pi^4}{45} - \frac{500\zeta_3}{9}\right)C_A^2\beta_0 + \left(\frac{466}{81} + \frac{5\pi^2}{9} - \frac{28\zeta_3}{3}\right)C_A\beta_0^2 \\
&\quad + \left(-\frac{1819}{54} + \frac{\pi^2}{3} + \frac{4\pi^4}{45} + \frac{152\zeta_3}{9}\right)C_A\beta_1 - 2\beta_2. \tag{B.20}
\end{aligned}$$

The non-cusp anomalous dimension for the gluon beam function is equal to that of the gluon jet function which is given by $\gamma_J^g(\alpha_s) = -2\gamma_H^g(\alpha_s) - \gamma_f^g(\alpha_s)$. Here, $\gamma_f^g(\alpha_s)$ is the coefficient of the $\delta(1-z)$ in the gluon PDF anomalous dimension which is known to three loops [102]. The resulting coefficients to three loops are

$$\begin{aligned}
\gamma_{B0}^g &= 2\beta_0, \\
\gamma_{B1}^g &= \left(\frac{182}{9} - 32\zeta_3\right)C_A^2 + \left(\frac{94}{9} - \frac{2\pi^2}{3}\right)C_A\beta_0 + 2\beta_1, \\
\gamma_{B2}^g &= \left(\frac{49373}{81} - \frac{944\pi^2}{81} - \frac{16\pi^4}{5} - \frac{4520\zeta_3}{9} + \frac{128\pi^2\zeta_3}{9} + 224\zeta_5\right)C_A^3 \\
&\quad + \left(-\frac{6173}{27} - \frac{376\pi^2}{81} + \frac{13\pi^4}{5} + \frac{280\zeta_3}{9}\right)C_A^2\beta_0 + \left(-\frac{986}{81} - \frac{10\pi^2}{9} + \frac{56\zeta_3}{3}\right)C_A\beta_0^2 \\
&\quad + \left(\frac{1765}{27} - \frac{2\pi^2}{3} - \frac{8\pi^4}{45} - \frac{304\zeta_3}{9}\right)C_A\beta_1 + 2\beta_2. \tag{B.21}
\end{aligned}$$

At NNLL we only need γ_H^g and γ_B^g at two loops. The three-loop coefficients are given for completeness. The result in eq. (B.21) agrees with that given in ref. [105] for the gluon jet function.⁸ The non-cusp anomalous dimension of the gluon beam-thrust soft function is given by $\gamma_S^g(\alpha_s) = -2\gamma_H^g(\alpha_s) - 2\gamma_B^g(\alpha_s)$.

B.4 Singular Fixed-Order NLO and NNLO Coefficients

In this Appendix we give our results for the perturbative coefficients C_{ij} entering in the fixed-order cross section in eq. (2.30). The coefficients for quarks and antiquarks are related as follows:

$$\begin{aligned}
C_{q\bar{q}}(z_a, z_b, \tau, Y, \mu) &= C_{qq}(z_a, z_b, \tau, Y, \mu), \quad C_{qg}(z_a, z_b, \tau, Y, \mu) = C_{\bar{q}g}(z_a, z_b, \tau, Y, \mu), \\
C_{qg}(z_a, z_b, \tau, Y, \mu) &= C_{gq}(z_b, z_a, \tau, -Y, \mu), \\
C_{q\bar{q}'}^s(z_a, z_b, \tau, Y, \mu) &= C_{\bar{q}q'}^s(z_a, z_b, \tau, Y, \mu) = C_{q\bar{q}'}^s(z_a, z_b, \tau, Y, \mu) = C_{q\bar{q}'}^s(z_a, z_b, \tau, Y, \mu). \tag{B.22}
\end{aligned}$$

⁸Apart from a typo in ref. [105] where one of the terms in the $C_A^2 n_f$ contribution is missing a π^2 .

The first line follows from charge-conjugation invariance and the second line from parity invariance of QCD. The last line is only true because we limit ourselves to contributions from gluon beam functions. Consequently, we only need to consider C_{gg} , C_{gq} , and $C_{q\bar{q}}$. The small contributions involving quark beam functions that we neglect correspond to $q\bar{q} \rightarrow H$ production, where the $q\bar{q}$ pair couples to the Higgs either directly or indirectly through a two-loop $q\bar{q} \rightarrow gg \rightarrow H$ diagram.

As in eq. (2.31) we split the coefficients into singular and nonsingular parts, where the singular coefficients are further decomposed as in eq. (2.32),

$$C_{ij}^s(z_a, z_b, \tau, Y, \mu) = C_{ij}^{-1}(z_a, z_b, Y, \mu) \delta(\tau) + \sum_{k \geq 0} C_{ij}^k(z_a, z_b, Y, \mu) \mathcal{L}_k(\tau). \quad (\text{B.23})$$

Each of the coefficients has an expansion in α_s , which we write as ($x = s$ or $x = k \geq -1$)

$$C_{ij}^x = C_{ij}^{x(0)} + \frac{\alpha_s(\mu)}{2\pi} C_{ij}^{x(1)} + \frac{\alpha_s^2(\mu)}{(2\pi)^2} C_{ij}^{x(2)} + \dots, \quad (\text{B.24})$$

corresponding to the LO, NLO, and NNLO contributions. (The overall α_s^2 of the Higgs cross section is factored out in eq. (2.30).) At leading order, the only nonzero coefficient is

$$C_{gg}^{s(0)}(z_a, z_b, \tau, Y, \mu) = \delta(\tau) \delta(1 - z_a) \delta(1 - z_b). \quad (\text{B.25})$$

The singular NLO terms are fully contained in the resummed result at NNLL. Hence, the simplest way to obtain them is to set $\mu_H = \mu_B = \mu_S = \mu$ in eq. (2.2), which eliminates the evolution factors, and expand it in $\alpha_s(\mu)$. Using the NLO results for the hard, beam, and soft functions, we find

$$\begin{aligned} C_{gg}^{s(1)}(z_a, z_b, \tau, Y, \mu) &= C_A \delta(1 - z_a) \theta(z_b) \left\{ -2\mathcal{L}_1(\tau) \delta(1 - z_b) + \mathcal{L}_0(\tau) P_{gg}(z_b) \right. \\ &\quad \left. + \delta(\tau) \left[\left(\frac{2\pi^2}{3} + Y^2 + \frac{F^{(1)}}{2C_A} \right) \delta(1 - z_b) - (Y + 2L_\mu) P_{gg}(z_b) + \mathcal{I}_{gg}^{(1,\delta)}(z_b) \right] \right\} \\ &\quad + (z_a \leftrightarrow z_b, Y \rightarrow -Y), \\ C_{gq}^{s(1)}(z_a, z_b, \tau, Y, \mu) &= C_F \delta(1 - z_a) \theta(z_b) \left\{ \mathcal{L}_0(\tau) P_{gq}(z_b) \right. \\ &\quad \left. + \delta(\tau) [\mathcal{I}_{gq}^{(1,\delta)}(z_b) - (Y + 2L_\mu) P_{gq}(z_b)] \right\}. \end{aligned} \quad (\text{B.26})$$

Here $L_\mu \equiv \ln(\mu/m_H)$ and $F^{(1)} \equiv F^{(1)}[m_H^2/(4m_t^2)]$. The L_μ terms in the NLO coefficients precisely cancel the μ dependence in the leading-order cross section coming from eq. (B.25).

The NNLO coefficients $C_{ij}^{k(2)}$ for $k \geq 0$ are reproduced by the resummed result at NNLL. Once we include the μ -dependent NNLO terms in the hard, beam, and soft functions (which are determined from the NNLL resummation), we can obtain the $C_{ij}^{k(2)}$ as before by setting $\mu_H = \mu_B = \mu_S = \mu$ in eq. (2.2) and expanding to $\mathcal{O}(\alpha_s^2)$. For $C_{ij}^{-1(2)}$ we are only able to obtain some parts analytically. We write it as [see eq. (2.38)]

$$C_{ij}^{-1(2)}(z_a, z_b, Y, \mu) = c_{ij}^\pi(z_a, z_b, Y) + c_{ij}^\mu(z_a, z_b, Y, \mu) + c_{ij}^{\text{res}}(z_a, z_b, Y). \quad (\text{B.27})$$

The first contribution denotes the π^2 terms, which we get by taking $\mu_H = \mu = m_H$ in the resummed result (as opposed to taking $\mu_H = -im_H$, which resums them into the hard evolution factor). The second contribution contains the μ -dependent terms proportional to $L_\mu = \ln(\mu/m_H)$, which we are able to obtain by requiring that they cancel the μ dependence of the singular NLO result. Obtaining an analytic expression for the remaining piece, $c_{ij}^{\text{res}}(z_a, z_b, Y)$, requires the complete two-loop hard, beam, and soft functions. Its contribution to the cross section after convolution with the PDFs and integrated over Y is extracted numerically from the fixed-order NNLO cross section as discussed in section 2.4.

For the nonzero coefficients of $C_{gg}^{\text{s}(2)}$ we find

$$\begin{aligned}
C_{gg}^{3(2)}(z_a, z_b, Y, \mu) &= 8C_A^2 \delta(1 - z_a)\delta(1 - z_b), \\
C_{gg}^{2(2)}(z_a, z_b, Y, \mu) &= \delta(1 - z_a) \left\{ -6C_A^2 P_{gg}(z_b) + \frac{3}{2}C_A\beta_0 \delta(1 - z_b) \right\} + (z_a \leftrightarrow z_b), \\
C_{gg}^{1(2)}(z_a, z_b, Y, \mu) &= \delta(1 - z_a) \left\{ C_A^2 \left[\left(-\frac{4}{3} - \frac{11}{3}\pi^2 - 4Y^2 \right) \delta(1 - z_b) + 4(Y + 2L_\mu)P_{gg}(z_b) \right. \right. \\
&\quad \left. \left. + (P_{gg} \otimes P_{gg})(z_b) - 4\mathcal{I}_{gg}^{(1,\delta)}(z_b) \right] - 2C_A F^{(1)} \delta(1 - z_b) \right. \\
&\quad \left. - C_A\beta_0 \left[\left(\frac{5}{3} + 2L_\mu \right) \delta(1 - z_b) + \frac{1}{2}P_{gg}(z_b) \right] + 2C_F T_F n_f (P_{gq} \otimes P_{qg})(z_b) \right\} \\
&\quad + C_A^2 P_{gg}(z_a)P_{gg}(z_b) + (z_a \leftrightarrow z_b, Y \rightarrow -Y), \\
C_{gg}^{0(2)}(z_a, z_b, Y, \mu) &= \delta(1 - z_a) \left\{ C_A^2 \left[(1 + 5\zeta_3)\delta(1 - z_b) + 2(\pi^2 + Y^2)P_{gg}(z_b) \right. \right. \\
&\quad \left. \left. - (Y + 2L_\mu)(P_{gg} \otimes P_{gg})(z_b) + (\mathcal{I}_{gg}^{(1,\delta)} \otimes P_{gg})(z_b) \right] \right. \\
&\quad \left. - \frac{1}{2}C_A\beta_0 \left[\left(2 + \frac{\pi^2}{6} + Y^2 \right) \delta(1 - z_b) - (Y + 2L_\mu)P_{gg}(z_b) + \mathcal{I}_{gg}^{(1,\delta)}(z_b) \right] \right. \\
&\quad \left. + 2C_F T_F n_f \left[\frac{1}{2}\delta(1 - z_b) - (Y + 2L_\mu)(P_{gq} \otimes P_{qg})(z_b) + (\mathcal{I}_{gq}^{(1,\delta)} \otimes P_{qg})(z_b) \right] \right. \\
&\quad \left. + C_A F^{(1)} P_{gg}(z_b) + P_{gg}^{(1)}(z_b) \right\} \\
&\quad + C_A^2 \left[\mathcal{I}_{gg}^{(1,\delta)}(z_a) - 2L_\mu P_{gg}(z_a) \right] P_{gg}(z_b) + (z_a \leftrightarrow z_b, Y \rightarrow -Y). \tag{B.28}
\end{aligned}$$

The two-loop splitting function, $P_{gg}^{(1)}(z)$ is given in eq. (B.9). The convolutions $(P_{ij} \otimes P_{jk})(z)$ and $(\mathcal{I}_{ij}^{(1,\delta)} \otimes P_{jk})(z)$ are defined in eq. (B.10) and their analytical expressions are given in eq. (B.11). For the μ -dependent and π^2 terms of $C_{gg}^{-1(2)}$ we get

$$\begin{aligned}
c_{gg}^\mu(z_a, z_b, Y, \mu) &= -2L_\mu \delta(1 - z_a) \left\{ C_A^2 \left[\left(\frac{4\pi^2}{3} + 2Y^2 \right) P_{gg}(z_b) \right. \right. \\
&\quad \left. \left. - (Y + L_\mu)(P_{gg} \otimes P_{gg})(z_b) + \mathcal{I}_{gg}^{(1,\delta)} \otimes P_{gg}(z_b) \right] \right. \\
&\quad \left. - \frac{1}{2}C_A\beta_0 \left[\left(\frac{2\pi^2}{3} + Y^2 \right) \delta(1 - z_b) - (Y + L_\mu)P_{gg}(z_b) + \mathcal{I}_{gg}^{(1,\delta)}(z_b) \right] \right. \\
&\quad \left. + 2C_F T_F n_f \left[-(Y + L_\mu)(P_{gq} \otimes P_{qg})(z_b) + \mathcal{I}_{gq}^{(1,\delta)} \otimes P_{qg}(z_b) \right] \right. \\
&\quad \left. - \frac{1}{4}(\beta_1 + F^{(1)}\beta_0)\delta(1 - z_b) + C_A F^{(1)} P_{gg}(z_b) + P_{gg}^{(1)}(z_b) \right\} \tag{B.29}
\end{aligned}$$

$$\begin{aligned}
& -2C_A^2 L_\mu \left[\mathcal{I}_{gg}^{(1,\delta)}(z_a) - L_\mu P_{gg}(z_a) \right] P_{gg}(z_b) + (z_a \leftrightarrow z_b, Y \rightarrow -Y), \\
c_{gg}^\pi(z_a, z_b, Y) &= \pi^2 \delta(1 - z_a) \left\{ C_A^2 \left[\left(\frac{1}{3} + \frac{\pi^2}{3} + Y^2 \right) \delta(1 - z_b) - Y P_{gg}(z_b) + \mathcal{I}_{gg}^{(1,\delta)}(z_b) \right] \right. \\
& \left. + \frac{5}{12} C_A \beta_0 \delta(1 - z_b) + \frac{1}{2} C_A F^{(1)} \delta(1 - z_b) \right\} + (z_a \leftrightarrow z_b, Y \rightarrow -Y).
\end{aligned}$$

For $C_{gg}^{s(2)}$ we find

$$\begin{aligned}
C_{gg}^{3(2)}(z_a, z_b, Y, \mu) &= 0, \tag{B.30} \\
C_{gg}^{2(2)}(z_a, z_b, Y, \mu) &= -6C_A C_F \delta(1 - z_a) P_{gq}(z_b), \\
C_{gg}^{1(2)}(z_a, z_b, Y, \mu) &= \delta(1 - z_a) \left\{ C_A C_F \left[4(Y + 2L_\mu) P_{gq}(z_b) + (P_{gg} \otimes P_{gq})(z_b) - 4\mathcal{I}_{gg}^{(1,\delta)}(z_b) \right] \right. \\
& \left. + C_F^2 (P_{gq} \otimes P_{qq})(z_b) - C_F \beta_0 P_{gq}(z_b) \right\} + 2C_A C_F P_{gg}(z_a) P_{gq}(z_b), \\
C_{gg}^{0(2)}(z_a, z_b, Y, \mu) &= \delta(1 - z_a) \left\{ C_A C_F \left[2(\pi^2 + Y^2) P_{gq}(z_b) - (Y + 2L_\mu) (P_{gg} \otimes P_{gq})(z_b) \right. \right. \\
& \left. \left. + (\mathcal{I}_{gg}^{(1,\delta)} \otimes P_{gq})(z_b) \right] \right. \\
& \left. + C_F^2 \left[-(Y + 2L_\mu) (P_{gq} \otimes P_{qq})(z_b) + (\mathcal{I}_{gq}^{(1,\delta)} \otimes P_{qq})(z_b) \right] \right. \\
& \left. + C_F \beta_0 \left[(Y + 2L_\mu) P_{gq}(z_b) - \mathcal{I}_{gq}^{(1,\delta)}(z_b) \right] + C_F F^{(1)} P_{gq}(z_b) + P_{gq}^{(1)}(z_b) \right\} \\
& \left. + C_A C_F \left[P_{gg}(z_a) \mathcal{I}_{gq}^{(1,\delta)}(z_b) + \mathcal{I}_{gg}^{(1,\delta)}(z_a) P_{gq}(z_b) - 4L_\mu P_{gg}(z_a) P_{gq}(z_b) \right]. \right.
\end{aligned}$$

The two-loop splitting function $P_{gq}^{(1)}(z)$ is given in eq. (B.9). For $C_{gq}^{-1(2)}$, the μ -dependent and π^2 terms are

$$\begin{aligned}
c_{gq}^\mu(z_a, z_b, Y, \mu) &= -2L_\mu \delta(1 - z_a) \left\{ C_A C_F \left[\left(\frac{4\pi^2}{3} + 2Y^2 \right) P_{gq}(z_b) - (Y + L_\mu) (P_{gg} \otimes P_{gq})(z_b) \right. \right. \\
& \left. \left. + (\mathcal{I}_{gg}^{(1,\delta)} \otimes P_{gq})(z_b) \right] + C_F^2 \left[-(Y + L_\mu) (P_{gq} \otimes P_{qq})(z_b) + (\mathcal{I}_{gq}^{(1,\delta)} \otimes P_{qq})(z_b) \right] \right. \\
& \left. + C_F \beta_0 \left[(Y + L_\mu) P_{gq}(z_b) - \mathcal{I}_{gq}^{(1,\delta)}(z_b) \right] + C_F F^{(1)} P_{gq}(z_b) + P_{gq}^{(1)}(z_b) \right\} \\
& - 2C_A C_F L_\mu \left[P_{gg}(z_a) \mathcal{I}_{gq}^{(1,\delta)}(z_b) + \mathcal{I}_{gg}^{(1,\delta)}(z_a) P_{gq}(z_b) - 2L_\mu P_{gg}(z_a) P_{gq}(z_b) \right], \\
c_{gq}^\pi(z_a, z_b, Y) &= \pi^2 C_A C_F \delta(1 - z_a) \left[-Y P_{gq}(z_b) + \mathcal{I}_{gq}^{(1,\delta)}(z_b) \right]. \tag{B.31}
\end{aligned}$$

Finally, for $C_{qq'}^{s(2)}$ we find

$$\begin{aligned}
C_{qq'}^{3(2)}(z_a, z_b, Y, \mu) &= C_{qq'}^{2(2)}(z_a, z_b, Y, \mu) = 0, \\
C_{qq'}^{1(2)}(z_a, z_b, Y, \mu) &= 2C_F^2 P_{gq}(z_a) P_{gq'}(z_b), \\
C_{qq'}^{0(2)}(z_a, z_b, Y, \mu) &= C_F^2 \left[P_{gq}(z_a) \mathcal{I}_{gq'}^{(1,\delta)}(z_b) + \mathcal{I}_{gq}^{(1,\delta)}(z_a) P_{gq'}(z_b) - 4L_\mu P_{gq}(z_a) P_{gq'}(z_b) \right]. \tag{B.32}
\end{aligned}$$

There is no contribution to $C_{qq'}^{-1(2)}$ from π^2 summation, $c_{qq'}^\pi = 0$. The μ -dependent terms are

$$c_{qq'}^\mu(z_a, z_b, Y, \mu) = -2C_F^2 L_\mu \left[P_{gq}(z_a) \mathcal{I}_{gq'}^{(1,\delta)}(z_b) + \mathcal{I}_{gq}^{(1,\delta)}(z_a) P_{gq'}(z_b) - 2L_\mu P_{gq}(z_a) P_{gq'}(z_b) \right]. \quad (\text{B.33})$$

References

- [1] **CDF and D0** Collaboration, T. Aaltonen *et. al.*, *Combination of Tevatron searches for the standard model Higgs boson in the W^+W^- decay mode*, *Phys. Rev. Lett.* **104** (2010) 061802, [[arXiv:1001.4162](#)].
- [2] **The ATLAS** Collaboration, G. Aad *et. al.*, *Expected Performance of the ATLAS Experiment - Detector, Trigger and Physics*, [arXiv:0901.0512](#).
- [3] **CMS** Collaboration, *Search Strategy for a Standard Model Higgs Boson Decaying to Two W Bosons in the Fully Leptonic Final State*, . CMS-PAS-HIG-08-006.
- [4] M. Dittmar and H. K. Dreiner, *How to find a Higgs boson with a mass between 155 GeV – 180 GeV at the LHC*, *Phys. Rev. D* **55** (1997) 167–172, [[hep-ph/9608317](#)].
- [5] **The CDF** Collaboration, T. Aaltonen *et. al.*, *Inclusive Search for Standard Model Higgs Boson Production in the WW Decay Channel using the CDF II Detector*, *Phys. Rev. Lett.* **104** (2010) 061803, [[arXiv:1001.4468](#)].
- [6] **The D0** Collaboration, V. M. Abazov *et. al.*, *Search for Higgs boson production in dilepton and missing energy final states with $\sim 5.4\text{fb}^{-1}$ of $p\bar{p}$ collisions at $\sqrt{s} = 1.96$ TeV*, *Phys. Rev. Lett.* **104** (2010) 061804, [[arXiv:1001.4481](#)].
- [7] **CDF and D0** Collaboration, *Combined CDF and D0 Upper Limits on Standard Model Higgs-Boson Production with up to 6.7fb^{-1} of Data*, [arXiv:1007.4587](#).
- [8] C. Anastasiou, G. Dissertori, M. Grazzini, F. Stöckli, and B. R. Webber, *Perturbative QCD effects and the search for a $H \rightarrow WW \rightarrow \ell\nu\ell\nu$ signal at the Tevatron*, *JHEP* **08** (2009) 099, [[arXiv:0905.3529](#)].
- [9] J. Baglio and A. Djouadi, *Predictions for Higgs production at the Tevatron and the associated uncertainties*, *JHEP* **10** (2010) 064, [[arXiv:1003.4266](#)].
- [10] F. Demartin, S. Forte, E. Mariani, J. Rojo, and A. Vicini, *The impact of PDF and alphas uncertainties on Higgs Production in gluon fusion at hadron colliders*, *Phys. Rev. D* **82** (2010) 014002, [[arXiv:1004.0962](#)].
- [11] J. Baglio and A. Djouadi, *Addendum to: Predictions for Higgs production at the Tevatron and the associated uncertainties*, [arXiv:1009.1363](#).
- [12] S. Dawson, *Radiative corrections to Higgs boson production*, *Nucl. Phys. B* **359** (1991) 283–300.
- [13] A. Djouadi, M. Spira, and P. M. Zerwas, *Production of Higgs bosons in proton colliders: QCD corrections*, *Phys. Lett. B* **264** (1991) 440–446.
- [14] M. Spira, A. Djouadi, D. Graudenz, and P. M. Zerwas, *Higgs boson production at the LHC*, *Nucl. Phys. B* **453** (1995) 17–82, [[hep-ph/9504378](#)].

- [15] R. V. Harlander and W. B. Kilgore, *Next-to-next-to-leading order Higgs production at hadron colliders*, *Phys. Rev. Lett.* **88** (2002) 201801, [[hep-ph/0201206](#)].
- [16] C. Anastasiou and K. Melnikov, *Higgs boson production at hadron colliders in NNLO QCD*, *Nucl. Phys. B* **646** (2002) 220–256, [[hep-ph/0207004](#)].
- [17] V. Ravindran, J. Smith, and W. L. van Neerven, *NNLO corrections to the total cross section for Higgs boson production in hadron hadron collisions*, *Nucl. Phys. B* **665** (2003) 325–366, [[hep-ph/0302135](#)].
- [18] A. Pak, M. Rogal, and M. Steinhauser, *Finite top quark mass effects in NNLO Higgs boson production at LHC*, *JHEP* **02** (2010) 025, [[arXiv:0911.4662](#)].
- [19] R. V. Harlander, H. Mantler, S. Marzani, and K. J. Ozeren, *Higgs production in gluon fusion at next-to-next-to-leading order QCD for finite top mass*, *Eur. Phys. J. C* **66** (2010) 359–372, [[arXiv:0912.2104](#)].
- [20] U. Aglietti, R. Bonciani, G. Degrossi, and A. Vicini, *Two-loop light fermion contribution to Higgs production and decays*, *Phys. Lett. B* **595** (2004) 432–441, [[hep-ph/0404071](#)].
- [21] S. Actis, G. Passarino, C. Sturm, and S. Uccirati, *NLO Electroweak Corrections to Higgs Boson Production at Hadron Colliders*, *Phys. Lett. B* **670** (2008) 12–17, [[arXiv:0809.1301](#)].
- [22] C. Anastasiou, R. Boughezal, and F. Petriello, *Mixed QCD-electroweak corrections to Higgs boson production in gluon fusion*, *JHEP* **04** (2009) 003, [[arXiv:0811.3458](#)].
- [23] A. Djouadi, *The Anatomy of electro-weak symmetry breaking. I: The Higgs boson in the standard model*, *Phys. Rept.* **457** (2008) 1–216, [[hep-ph/0503172](#)].
- [24] R. Boughezal, *Theoretical Status of Higgs Production at Hadron Colliders in the SM*, [[arXiv:0908.3641](#)].
- [25] C. Anastasiou, G. Dissertori, F. Stöckli, and B. R. Webber, *QCD radiation effects on the $H \rightarrow WW \rightarrow \ell\nu\ell\nu$ signal at the LHC*, *JHEP* **03** (2008) 017, [[arXiv:0801.2682](#)].
- [26] S. Catani, D. de Florian, and M. Grazzini, *Direct Higgs production and jet veto at the Tevatron and the LHC in NNLO QCD*, *JHEP* **01** (2002) 015, [[hep-ph/0111164](#)].
- [27] C. Anastasiou, K. Melnikov, and F. Petriello, *Higgs boson production at hadron colliders: Differential cross sections through next-to-next-to-leading order*, *Phys. Rev. Lett.* **93** (2004) 262002, [[hep-ph/0409088](#)].
- [28] G. Davatz *et. al.*, *Combining Monte Carlo generators with next-to-next-to-leading order calculations: Event reweighting for Higgs boson production at the LHC*, *JHEP* **07** (2006) 037, [[hep-ph/0604077](#)].
- [29] C. Anastasiou, G. Dissertori, and F. Stöckli, *NNLO QCD predictions for the $H \rightarrow WW \rightarrow \ell\nu\ell\nu$ signal at the LHC*, *JHEP* **09** (2007) 018, [[arXiv:0707.2373](#)].
- [30] M. Grazzini, *NNLO predictions for the Higgs boson signal in the $H \rightarrow WW \rightarrow \ell\nu\ell\nu$ and $H \rightarrow ZZ \rightarrow 4\ell$ decay channels*, *JHEP* **02** (2008) 043, [[arXiv:0801.3232](#)].
- [31] E. L. Berger, Q.-H. Cao, C. B. Jackson, T. Liu, and G. Shaughnessy, *Higgs Boson Search Sensitivity in the $H \rightarrow WW$ Dilepton Decay Mode at $\sqrt{s} = 7$ and 10 TeV*, *Phys. Rev. D* **82** (2010) 053003, [[arXiv:1003.3875](#)].

- [32] S. Frixione and B. R. Webber, *Matching NLO QCD computations and parton shower simulations*, *JHEP* **06** (2002) 029, [[hep-ph/0204244](#)].
- [33] S. Frixione, P. Nason, and B. R. Webber, *Matching NLO QCD and parton showers in heavy flavour production*, *JHEP* **08** (2003) 007, [[hep-ph/0305252](#)].
- [34] S. Alioli, P. Nason, C. Oleari, and E. Re, *NLO Higgs boson production via gluon fusion matched with shower in POWHEG*, *JHEP* **04** (2009) 002, [[arXiv:0812.0578](#)].
- [35] K. Hamilton, P. Richardson, and J. Tully, *A Positive-Weight Next-to-Leading Order Monte Carlo Simulation for Higgs Boson Production*, *JHEP* **04** (2009) 116, [[arXiv:0903.4345](#)].
- [36] T. Sjöstrand, S. Mrenna, and P. Skands, *Pythia 6.4 physics and manual*, *JHEP* **05** (2006) 026, [[hep-ph/0603175](#)].
- [37] T. Sjöstrand, S. Mrenna, and P. Skands, *A Brief Introduction to PYTHIA 8.1*, *Comput. Phys. Commun.* **178** (2008) 852–867, [[arXiv:0710.3820](#)].
- [38] G. Corcella *et. al.*, *Herwig 6: An event generator for hadron emission reactions with interfering gluons (including supersymmetric processes)*, *JHEP* **01** (2001) 010, [[hep-ph/0011363](#)].
- [39] G. Corcella *et. al.*, *HERWIG 6.5 release note*, [[hep-ph/0210213](#)].
- [40] D. de Florian, M. Grazzini, and Z. Kunszt, *Higgs production with large transverse momentum in hadronic collisions at next-to-leading order*, *Phys. Rev. Lett.* **82** (1999) 5209–5212, [[hep-ph/9902483](#)].
- [41] V. Ravindran, J. Smith, and W. L. Van Neerven, *Next-to-leading order QCD corrections to differential distributions of Higgs boson production in hadron hadron collisions*, *Nucl. Phys. B* **634** (2002) 247–290, [[hep-ph/0201114](#)].
- [42] C. J. Glosser and C. R. Schmidt, *Next-to-leading corrections to the Higgs boson transverse momentum spectrum in gluon fusion*, *JHEP* **12** (2002) 016, [[hep-ph/0209248](#)].
- [43] C. Anastasiou, K. Melnikov, and F. Petriello, *Fully differential Higgs boson production and the di-photon signal through next-to-next-to-leading order*, *Nucl. Phys. B* **724** (2005) 197–246, [[hep-ph/0501130](#)].
- [44] J. C. Collins, D. E. Soper, and G. Sterman, *Transverse Momentum Distribution in Drell-Yan Pair and W and Z Boson Production*, *Nucl. Phys. B* **250** (1985) 199.
- [45] C. Balazs and C. P. Yuan, *Higgs boson production at the LHC with soft gluon effects*, *Phys. Lett. B* **478** (2000) 192–198, [[hep-ph/0001103](#)].
- [46] E. L. Berger and J.-w. Qiu, *Differential cross section for Higgs boson production including all-orders soft gluon resummation*, *Phys. Rev. D* **67** (2003) 034026, [[hep-ph/0210135](#)].
- [47] G. Bozzi, S. Catani, D. de Florian, and M. Grazzini, *The q_T spectrum of the Higgs boson at the LHC in QCD perturbation theory*, *Phys. Lett. B* **564** (2003) 65–72, [[hep-ph/0302104](#)].
- [48] A. Kulesza, G. Sterman, and W. Vogelsang, *Joint resummation for Higgs production*, *Phys. Rev. D* **69** (2004) 014012, [[hep-ph/0309264](#)].
- [49] A. Idilbi, X.-d. Ji, and F. Yuan, *Transverse momentum distribution through soft-gluon resummation in effective field theory*, *Phys. Lett. B* **625** (2005) 253–263, [[hep-ph/0507196](#)].
- [50] G. Bozzi, S. Catani, D. de Florian, and M. Grazzini, *Transverse-momentum resummation and*

- the spectrum of the Higgs boson at the LHC*, *Nucl. Phys. B* **737** (2006) 73–120, [[hep-ph/0508068](#)].
- [51] S. Mantry and F. Petriello, *Factorization and Resummation of Higgs Boson Differential Distributions in Soft-Collinear Effective Theory*, *Phys. Rev. D* **81** (2010) 093007, [[arXiv:0911.4135](#)].
- [52] E. Laenen, G. Sterman, and W. Vogelsang, *Recoil and threshold corrections in short distance cross-sections*, *Phys. Rev. D* **63** (2001) 114018, [[hep-ph/0010080](#)].
- [53] D. de Florian and M. Grazzini, *Higgs production through gluon fusion: updated cross sections at the Tevatron and the LHC*, *Phys. Lett. B* **674** (2009) 291–294, [[arXiv:0901.2427](#)].
- [54] G. Davatz, G. Dissertori, M. Dittmar, M. Grazzini, and F. Pauss, *Effective K-factors for $gg \rightarrow H \rightarrow WW \rightarrow \ell\nu\ell\nu$ at the LHC*, *JHEP* **05** (2004) 009, [[hep-ph/0402218](#)].
- [55] A. Papaefstathiou, J. M. Smillie, and B. R. Webber, *Resummation of transverse energy in vector boson and Higgs boson production at hadron colliders*, *JHEP* **04** (2010) 084, [[arXiv:1002.4375](#)].
- [56] I. W. Stewart, F. J. Tackmann, and W. J. Waalewijn, *Factorization at the LHC: From PDFs to Initial State Jets*, *Phys. Rev. D* **81** (2010) 094035, [[arXiv:0910.0467](#)].
- [57] S. Catani, D. de Florian, M. Grazzini, and P. Nason, *Soft-gluon resummation for Higgs boson production at hadron colliders*, *JHEP* **07** (2003) 028, [[hep-ph/0306211](#)].
- [58] S. Moch and A. Vogt, *Higher-order soft corrections to lepton pair and Higgs boson production*, *Phys. Lett. B* **631** (2005) 48–57, [[hep-ph/0508265](#)].
- [59] A. Idilbi, X.-d. Ji, J.-P. Ma, and F. Yuan, *Threshold resummation for Higgs production in effective field theory*, *Phys. Rev. D* **73** (2006) 077501, [[hep-ph/0509294](#)].
- [60] E. Laenen and L. Magnea, *Threshold resummation for electroweak annihilation from DIS data*, *Phys. Lett. B* **632** (2006) 270–276, [[hep-ph/0508284](#)].
- [61] V. Ravindran, *Higher-order threshold effects to inclusive processes in QCD*, *Nucl. Phys. B* **752** (2006) 173–196, [[hep-ph/0603041](#)].
- [62] V. Ahrens, T. Becher, M. Neubert, and L. L. Yang, *Updated Predictions for Higgs Production at the Tevatron and the LHC*, *Phys. Lett. B* **698** (2011) 271–274, [[arXiv:1008.3162](#)].
- [63] I. W. Stewart, F. J. Tackmann, and W. J. Waalewijn, *N-Jettiness: An Inclusive Event Shape to Veto Jets*, *Phys. Rev. Lett.* **105** (2010) 092002, [[arXiv:1004.2489](#)].
- [64] A. D. Martin, W. J. Stirling, R. S. Thorne, and G. Watt, *Parton distributions for the LHC*, *Eur. Phys. J. C* **63** (2009) 189–285, [[arXiv:0901.0002](#)].
- [65] M. Cacciari, G. P. Salam, and G. Soyez, *The anti- k_t jet clustering algorithm*, *JHEP* **04** (2008) 063, [[arXiv:0802.1189](#)].
- [66] M. Cacciari, G. P. Salam, and G. Soyez. <http://fastjet.fr/>.
- [67] N. Kidonakis, *Next-to-next-to-leading soft-gluon corrections for the top quark cross section and transverse momentum distribution*, *Phys. Rev. D* **82** (2010) 114030, [[arXiv:1009.4935](#)].
- [68] I. W. Stewart, F. J. Tackmann, and W. J. Waalewijn, *The Quark Beam Function at NNLL*, *JHEP* **09** (2010) 005, [[arXiv:1002.2213](#)].

- [69] S. Fleming, A. K. Leibovich, and T. Mehen, *Resummation of Large Endpoint Corrections to Color-Octet J/ψ Photoproduction*, *Phys. Rev. D* **74** (2006) 114004, [[hep-ph/0607121](#)].
- [70] C. W. Bauer, S. Fleming, and M. E. Luke, *Summing Sudakov logarithms in $B \rightarrow X_s \gamma$ in effective field theory*, *Phys. Rev. D* **63** (2000) 014006, [[hep-ph/0005275](#)].
- [71] C. W. Bauer, S. Fleming, D. Pirjol, and I. W. Stewart, *An effective field theory for collinear and soft gluons: Heavy to light decays*, *Phys. Rev. D* **63** (2001) 114020, [[hep-ph/0011336](#)].
- [72] C. W. Bauer and I. W. Stewart, *Invariant operators in collinear effective theory*, *Phys. Lett. B* **516** (2001) 134–142, [[hep-ph/0107001](#)].
- [73] C. W. Bauer, D. Pirjol, and I. W. Stewart, *Soft-collinear factorization in effective field theory*, *Phys. Rev. D* **65** (2002) 054022, [[hep-ph/0109045](#)].
- [74] C. W. Bauer, S. Fleming, D. Pirjol, I. Z. Rothstein, and I. W. Stewart, *Hard scattering factorization from effective field theory*, *Phys. Rev. D* **66** (2002) 014017, [[hep-ph/0202088](#)].
- [75] Z. Ligeti, I. W. Stewart, and F. J. Tackmann, *Treating the b quark distribution function with reliable uncertainties*, *Phys. Rev. D* **78** (2008) 114014, [[arXiv:0807.1926](#)].
- [76] R. Harlander and P. Kant, *Higgs production and decay: Analytic results at next-to-leading order QCD*, *JHEP* **12** (2005) 015, [[hep-ph/0509189](#)].
- [77] C. Anastasiou, S. Beerli, S. Bucherer, A. Daleo, and Z. Kunszt, *Two-loop amplitudes and master integrals for the production of a Higgs boson via a massive quark and a scalar-quark loop*, *JHEP* **01** (2007) 082, [[hep-ph/0611236](#)].
- [78] R. V. Harlander and K. J. Ozeren, *Top mass effects in Higgs production at next-to-next-to-leading order QCD: virtual corrections*, *Phys. Lett. B* **679** (2009) 467–472, [[arXiv:0907.2997](#)].
- [79] A. Pak, M. Rogal, and M. Steinhauser, *Virtual three-loop corrections to Higgs boson production in gluon fusion for finite top quark mass*, *Phys. Lett. B* **679** (2009) 473–477, [[arXiv:0907.2998](#)].
- [80] G. Parisi, *Summing Large Perturbative Corrections in QCD*, *Phys. Lett. B* **90** (1980) 295.
- [81] G. Sterman, *Summation of Large Corrections to Short Distance Hadronic Cross-Sections*, *Nucl. Phys. B* **281** (1987) 310.
- [82] L. Magnea and G. Sterman, *Analytic continuation of the Sudakov form-factor in QCD*, *Phys. Rev. D* **42** (1990) 4222–4227.
- [83] T. O. Eynck, E. Laenen, and L. Magnea, *Exponentiation of the Drell-Yan cross section near partonic threshold in the DIS and MS-bar schemes*, *JHEP* **06** (2003) 057, [[hep-ph/0305179](#)].
- [84] V. Ahrens, T. Becher, M. Neubert, and L. L. Yang, *Origin of the Large Perturbative Corrections to Higgs Production at Hadron Colliders*, *Phys. Rev. D* **79** (2009) 033013, [[arXiv:0808.3008](#)].
- [85] V. Ahrens, T. Becher, M. Neubert, and L. L. Yang, *Renormalization-Group Improved Prediction for Higgs Production at Hadron Colliders*, *Eur. Phys. J. C* **62** (2009) 333–353, [[arXiv:0809.4283](#)].
- [86] J.-y. Chiu, R. Kelley, and A. V. Manohar, *Electroweak Corrections using Effective Field*

- Theory: Applications to the LHC*, *Phys. Rev. D* **78** (2008) 073006, [[arXiv:0806.1240](#)].
- [87] J.-y. Chiu, A. Fuhrer, R. Kelley, and A. V. Manohar, *Factorization Structure of Gauge Theory Amplitudes and Application to Hard Scattering Processes at the LHC*, *Phys. Rev. D* **80** (2009) 094013, [[arXiv:0909.0012](#)].
- [88] S. Mantry and F. Petriello, *Transverse Momentum Distributions from Effective Field Theory with Numerical Results*, *Phys. Rev. D* **83** (2011) 053007, [[arXiv:1007.3773](#)].
- [89] M. D. Schwartz, *Resummation and NLO Matching of Event Shapes with Effective Field Theory*, *Phys. Rev. D* **77** (2008) 014026, [[arXiv:0709.2709](#)].
- [90] S. Fleming, A. H. Hoang, S. Mantry, and I. W. Stewart, *Top Jets in the Peak Region: Factorization Analysis with NLL Resummation*, *Phys. Rev. D* **77** (2008) 114003, [[arXiv:0711.2079](#)].
- [91] A. H. Hoang and I. W. Stewart, *Designing Gapped Soft Functions for Jet Production*, *Phys. Lett. B* **660** (2008) 483–493, [[arXiv:0709.3519](#)].
- [92] R. Abbate, M. Fickinger, A. H. Hoang, V. Mateu, and I. W. Stewart, *Thrust at N³LL with Power Corrections and a Precision Global Fit for $\alpha_s(m_Z)$* , [arXiv:1006.3080](#).
- [93] A. D. Martin, W. J. Stirling, R. S. Thorne, and G. Watt, *Uncertainties on α_s in global PDF analyses and implications for predicted hadronic cross sections*, *Eur. Phys. J. C* **64** (2009) 653–680, [[arXiv:0905.3531](#)].
- [94] I. W. Stewart, F. J. Tackmann, and W. J. Waalewijn, *The Beam Thrust Cross Section for Drell-Yan at NNLL Order*, *Phys. Rev. Lett.* **106** (2011) 032001, [[arXiv:1005.4060](#)].
- [95] A. V. Manohar and I. W. Stewart, *The zero-bin and mode factorization in quantum field theory*, *Phys. Rev. D* **76** (2007) 074002, [[hep-ph/0605001](#)].
- [96] G. Altarelli and G. Parisi, *Asymptotic Freedom in Parton Language*, *Nucl. Phys. B* **126** (1977) 298.
- [97] S. Dawson and R. Kauffman, *QCD corrections to Higgs boson production: nonleading terms in the heavy quark limit*, *Phys. Rev. D* **49** (1994) 2298–2309, [[hep-ph/9310281](#)].
- [98] W. Furmanski and R. Petronzio, *Singlet Parton Densities Beyond Leading Order*, *Phys. Lett. B* **97** (1980) 437.
- [99] R. K. Ellis and W. Vogelsang, *The evolution of parton distributions beyond leading order: the singlet case*, [hep-ph/9602356](#).
- [100] O. V. Tarasov, A. A. Vladimirov, and A. Y. Zharkov, *The Gell-Mann-Low Function of QCD in the Three Loop Approximation*, *Phys. Lett. B* **93** (1980) 429–432.
- [101] S. A. Larin and J. A. M. Vermaseren, *The three-loop QCD β function and anomalous dimensions*, *Phys. Lett. B* **303** (1993) 334–336, [[hep-ph/9302208](#)].
- [102] A. Vogt, S. Moch, and J. A. M. Vermaseren, *The three-loop splitting functions in QCD: The singlet case*, *Nucl. Phys. B* **691** (2004) 129–181, [[hep-ph/0404111](#)].
- [103] S. Moch, J. A. M. Vermaseren, and A. Vogt, *Three-loop results for quark and gluon form factors*, *Phys. Lett. B* **625** (2005) 245–252, [[hep-ph/0508055](#)].
- [104] A. Idilbi, X. dong Ji, and F. Yuan, *Resummation of Threshold Logarithms in Effective Field*

Theory For DIS, Drell-Yan and Higgs Production, *Nucl. Phys. B* **753** (2006) 42–68,
[[hep-ph/0605068](#)].

- [105] T. Becher and M. D. Schwartz, *Direct photon production with effective field theory*, *JHEP* **02** (2010) 040, [[arXiv:0911.0681](#)].